UNIVERSITÉ LAVAL

Comparative study of infrared thermography, ultrasonic C-scan, X-ray computed tomography and terahertz imaging on composite materials

Thèse

Hai Zhang

Doctorat en génie électrique
Philosophiæ doctor (Ph. D.)

Québec, Canada

Comparative study of infrared thermography, ultrasonic C-scan, X-ray computed tomography and terahertz imaging on composite materials

Thèse

Hai Zhang

Sous la direction de:

Xavier Maldague, directeur de recherche

Résumé

L'évaluation non destructive (NDT) des matériaux composites est compliquée en raison de la vaste gamme de défauts rencontrés (y compris délaminage, microfissuration, fracture de la fibre, retrait des fibres, fissuration matricielle, inclusions, vides et dommages aux chocs). La capacité de caractériser quantitativement le type, la géométrie et l'orientation des défauts est essentielle. La thermographie infrarouge (IRT), en tant que technique de diagnostic d'image, peut satisfaire le besoin industriel croissant de NDT&E.

Dans la thèse, la thermographie par excitation optique et mécanique a été utilisée pour étudier différents matériaux composites, dont 1) des préformes sèches en fibres de carbone, 2) des composites de fibres naturelles, 3) des composites hybrides de basalte-fibres de carbone soumis à une charge d'impact (séquence de type sandwich et séquence d'empilement intercalé), 4) des défauts micro-dimensionnés dans un composite polymère renforcé de fibre de carbone (CFRP) en 3D avec une couture de type « joint en T », et 5) des peintures sur toile qui peuvent être considérées comme des matériaux composites. Une nouvelle technique IRT de thermographie de ligne par micro-laser (micro-LLT) a été proposée pour l'évaluation des porosités submillimétriques dans le CFRP. La microscopie de points par micro-laser (micro-LST) et la micro-vibrothermographie (micro-VT) ont également été présentées avec l'utilisation de microlentilles. La thermographie pulsée (PT) et la thermographie modulée « à verrouillage » (LT) ont été comparées à la tomographie par rayons X (TC) pour validation. Le C-scan ultrasonore (UT) et l'imagerie par ondes tera-hertziennes en onde continue (CW THz) ont également été réalisés à des fins comparatives. L'inspection par techniques thermographiques est une question ouverte à discuter pour le public scientifique. En fait, la thermographie par impulsions (PPT) basée sur la transformation de phase a été utilisée pour estimer la profondeur des dommages. Pour traiter les données thermographiques, on a également utilisé la reconstruction de signal thermographique de base (B-TSR), la thermographie des composants principaux (PCT) et la thermographie des moindres carrés partiels (PLST). Enfin, une analyse complète et comparative basée sur le diagnostic d'images thermographiques a été menée en vue d'applications industrielles potentielles.

Abstract

Non-destructive testing (NDT) of composite materials is complicated due to the wide range of flaws encountered (including delamination, micro-cracking, fiber fracture, fiber pullout, matrix cracking, inclusions, voids, and impact damage). The ability to quantitatively characterize the type, geometry, and orientation of flaws is essential. Infrared thermography (IRT), as an image diagnostic technique, can satisfy the increasing industrial need for NDT&E.

In the thesis, optical and mechanical excitation thermography were used to investigate different composite materials, including 1) carbon fiber dry preforms, 2) natural fiber composites, 3) basalt-carbon fiber hybrid composites subjected to impact loading (sandwich-like and intercalated stacking sequence), 4) micro-sized flaws in a stitched T-joint 3D carbon fiber reinforced polymer composite (CFRP), and 5) paintings on canvas which can be considered as composite materials. Of particular interest, a new IRT technique micro-laser line thermography (micro-LLT) was proposed for the evaluation of submillimeter porosities in CFRP. Micro-laser spot thermography (micro-LST) and micro-vibrothermography (micro-VT) were also presented with the usage of a micro-lens. Pulsed thermography (PT) and lock-in thermography (LT) were compared with x-ray computed tomography (CT) for validation. Ultrasonic C-scan (UT) and continuous wave terahertz imaging (CW THz) were also conducted for the comparative purpose. The inspection by thermographic techniques is an open matter to be discussed for the scientific audience. In fact, pulse phase thermography (PPT) based on phase transform was used to estimate the damage depth. Basic thermographic signal reconstruction (B-TSR), principal component thermography (PCT) and partial least squares thermography (PLST) (another more recent advanced image processing technique) were also used to process the thermographic data. Finally, a comprehensive and comparative analysis based on thermographic image diagnostics was conducted in view of potential industrial applications.

Contents

Résumé iii

Abstract iv

Contents v

List of Tables vii

List of Figures viii

Acknowledgements xvii

Introduction 1

1 A Review of NDT&E techniques 4
- 1.1 Optical Excitation Thermography in this research . . . 4
- 1.2 Mechanical Excitation Thermography . . . 5
- 1.3 Ultrasonic C-scan (UT) . . . 6
- 1.4 X-ray Computed Tomography (CT) . . . 6
- 1.5 Continuous Wave Terahertz Imaging (CW THz) . . . 7

2 Infrared Image Processing 9
- 2.1 Pulsed Phase Thermography (PPT) . . . 9
- 2.2 Partial Least Square Thermography (PLST) . . . 10
- 2.3 Principal Component Thermography (PCT) . . . 12
- 2.4 Basic Thermographic Signal Reconstruction (B-TSR) . . . 14
- 2.5 Cold Image Subtraction (CIS) . . . 15

3 Image Diagnosis for Industrial Carbon Fiber Dry Preform 16
- 3.1 Introduction . . . 16
- 3.2 Carbon Fiber Dry Preforms . . . 17
- 3.3 Experimental Configurations . . . 19
- 3.4 Experimental Measurement for Thermal Diffusivity . . . 20
- 3.5 Experimental Results and Analysis . . . 22
- 3.6 Summary . . . 26

4 Image Diagnosis and Characterization for Natural Fiber Composites 30
- 4.1 Introduction . . . 30
- 4.2 Natural Fiber Composites . . . 31

4.3 Experimental Configurations . . . 33
4.4 Experimental Results and Analysis . . . 36
4.5 Summary . . . 42

5 Image Diagnostics of Impact Damage in Basalt and Carbon Fiber Composites 45
5.1 Introduction . . . 45
5.2 Basalt-Carbon Hybrid Composites . . . 46
5.3 Experimental Configurations . . . 47
5.4 Experimental Results and Analysis . . . 48
5.5 Summary . . . 55

6 Image Diagnosis for Micro-sized Flaws in CFRP 57
6.1 Introduction . . . 57
6.2 T-joint CFRP . . . 59
6.3 Inspection Results Using the Established Techniques . . . 61
6.4 Micro Laser Line Thermography (Micro-LLT) . . . 67
6.5 Lock-in Micro-LLT and Micro-LST . . . 76
6.6 Micro-vibrothermoraphy (Micro-VT) . . . 79
6.7 Summary . . . 82

7 Non-destructive Investigation of Paintings on Canvas 84
7.1 Introduction . . . 84
7.2 Description of The Samples . . . 87
7.3 Experimental Configurations . . . 88
7.4 Result Analysis . . . 91
7.5 Summary . . . 94

Conclusion 96

A List of contributions 98

Bibliography 101

List of Tables

3.1 Orientation/width of layers and defects. 18
3.2 Thermal diffusivity by theoretical calculation and experimental measurement. . 21
3.3 Relationship between modulated frequency f_b and detection depth z. 22
3.4 Performance of thermographic methods. 28

4.1 Dent depth as a function of impact energy. 33
4.2 Flir Phoenix (MWIR) technical specifications [1]. 34
4.3 Physical properties of materials. 36
4.4 Relationship between modulated frequency f_b and depth z. 42
4.5 Capabilities of different techniques. 44

5.1 Thickness and fiber volume fraction of specimens. 46
5.2 Damaged areas obtained from PCT in PT and VT. 49
5.3 Damaged areas obtained from PLST. 50
5.4 Calculated thermal diffusivity α. 51
5.5 Relationship between modulated frequency f_b and depth z. 52
5.6 Damaged areas obtained from PPT and LT. 53

6.1 The model geometrical parameters 61
6.2 The material properties 70
6.3 Detection capacity of pulsed micro-LLT. 76
6.4 Micro-VT generator technical specifications. 79
6.5 Experimental thermographic results. 81

List of Figures

2.1 Schematic representation of the transformation of the 3D thermal data into a 2D raster-like matrix. 12
2.2 (a) Thermographic data rearrangement from a 3D sequence to a 2D A matrix in order to apply SVD, (b) rearrangement of 2D U matrix into a 3D matrix containing the EOFs [2]. 13
2.3 Typical use of TSR (model: 8 plies CFRP (0.0125" / ply)) [3] 14
2.4 An example with an academic aluminum plate to explain cold image subtraction. 15

3.1 Photographs of TW and PW specimens: (a) TW-01: front side, (b) TW-02: front side, (c) PW-01: front side, (d) TW-01: rear side, (e) TW-02: rear side, (f) PW-01: rear side. 17
3.2 Photographs of US specimens: (a) US-01: front side, (b) US-02: front side, (c) US-03: front side, (d) US-01: rear side, (e) US-02: rear side, (f) US-03: rear side. 18
3.3 Optical excitation thermography set-ups: (a) schematic set-up for PT using flashes, (b) schematic set-up for PT and LT using lamps, (c) experimental set-up for PT using flashes, (d) experimental set-up for PT and LT using lamps. . 19
3.4 (a) Experimental measurement set-up, (b) an example for the α calculation. . . 21
3.5 Phase transform results of TW/PW specimens using the flashes set-up and 88 fps: (a) TW-01: 0.25 mm, (b) TW-01: 0.4 mm, (c) TW-01: 0.5 mm, (d) TW-02: 0.25 mm, (e) TW-02: 0.4 mm, (f) TW-02: 0.5 mm, (g) PW-01: 0.25 mm, (h) PW-01: 0.4 mm, (i) PW-01: 0.5 mm. 23
3.6 B-TSR and PCT results of TW/PW specimens using the flashes set-up and 88 fps: (a) TW-01: B-TSR (1st), (b) TW-01: B-TSR (2nd), (c) TW-01: PCT (EOF03), (d) TW-02: B-TSR (1st), (e) TW-02: B-TSR (2nd), (f) TW-02: PCT (EOF03), (g) PW-01: B-TSR (1st), (h) PW-01: B-TSR (2nd), (i) PW-01: PCT (EOF01). 24
3.7 PLST results of TW/PW specimens using the flashes set-up and 88 fps: (a) TW-01: 1st loading, (b) TW-01: 2nd loading, (c) TW-01: 3rd loading, (d) TW-02: 1st loading, (e) TW-02: 2nd loading, (f) TW-02: 3rd loading, (g) PW-01: 1st loading, (h) PW-01: 2nd loading, (i) PW-01: 3rd loading. 25
3.8 Phase transform results of US specimens using the flashes set-up and 88 fps: (a) US-01: 0.15 mm, (b) US-01: 0.3 mm, (c) US-01: 0.4 mm, (d) US-02: 0.15 mm, (e) US-02: 0.3 mm, (f) US-02: 0.4 mm, (g) US-03: 0.15 mm, (h) US-03: 0.3 mm, (i) US-03: 0.4 mm. 26

3.9 B-TSR and PCT results of US specimens using the flashes set-up and 88 fps: (a) US-01: B-TSR (1st), (b) US-01: B-TSR (2nd), (c) US-01: PCT (EOF01), (d) US-02: B-TSR (1st), (e) US-02: B-TSR (2nd), (f) US-02: PCT (EOF01), (g) US-03: B-TSR (1st), (h) US-03: B-TSR (2nd), (i) US-03: PCT (EOF01). . 27
3.10 PLST results of US specimens using the flashes set-up and 88 fps: (a) US-01: 1st loading, (b) US-01: 3rd loading, (c) US-01: 5th loading, (d) US-02: 1st loading, (e) US-02: 3rd loading, (f) US-02: 5th loading, (g) US-03: 1st loading, (h) US-03: 3rd loading, (i) US-03: 5thUS loading. 28
3.11 Thermographic results of PW-01 and US-03 using the flash/halogen lamps set-ups and 55 fps: (a) PW-03: 0.9 mm, (b) PW-01: 1.65 mm, (c) PW-01: B-TSR (1st), (d) PW-01: PCT (EOF03), (e) US-03: 0.5 mm, (f) US-03: 0.9 mm, (g) US-03: B-TSR (1st), (h) US-03: PCT (EOF03). 29
3.12 (a) US-03: Phase-based LT (0.8 mm), (b) US-03: PCT (EOF04), (c) US-03: twisted front photo, (d) US-03: twisted rear photo. 29

4.1 BFRP specimens (rear side): (a) 7.5 J, (b) 15 J, (c) 22.5 J. 31
4.2 Jute/hemp fiber hybrid laminates (rear side): (a) plate No. 1, (b) plate No. 2, (c) plate No. 3. 32
4.3 SCB specimens (front side): (a) 5 J, (b) 10 J, (c) 20 J, (d) 30 J. 32
4.4 Optical excitation thermography set-ups: (a) schematic set-up for LT [4], (b) schematic set-up for PT (flashes) [4], (c) experimental set-up for LT/PT (halogen lamps), (d) experimental set-up for PT (flashes). 33
4.5 VT set-up, (a) schematic set-up using lock-in signals [4], schematic set-up using pulse signals [4], (c) experimental set-up. 34
4.6 UT experimental set-up. 35
4.7 CW sub-THz imaging system in reflection mode: (a) experimental set-up, (b) schematic set-up. 35
4.8 PT results of BFRP: (a) 7.5 J: 0.28 mm, (b) 15 J: 0.28 mm, (c) 22.5 J: 0.28 mm, (d) 7.5 J: 0.85 mm, (e) 15 J: 0.85 mm, (f) 22.5 J: 0.85 mm, (g) 7.5 J: 1 mm, (h) 15 J: 1 mm, (i) 22.5 J 1 mm, (j) 7.5 J: PCT (EOF03), (k) 15 J: PCT (EOF04), (l) 22.5 J: PCT (EOF03). 37
4.9 UT results of BFRP: (a) 7.5 J, (b) 15 J, (c) 22.5 J. 38
4.10 VT results BFRP: (a) 7.5 J: PCT (EOF06), (b) 15 J: PCT (EOF03), (c) 22.5 J: PCT (EOF02). 38
4.11 Front-side results of 15 J BFRP: (a) photo, (b) UT result, (c) CW sub-THz result, (d) intensity curve for sub-THz result, (e) phase: 0.28 mm, (f) phase: 0.85 mm, (g) phase: 1 mm, (h) PCT: EOF03. 39
4.12 IRT results of JHFP: (a) plate No.1: 0.44 mm, (b) plate No.2: 0.44 mm, (c) plate No.3: 0.44 mm, (d) plate No.1: 1.72 mm, (e) plate No.2: 1.72 mm, (f) plate No.3: 1.72 mm, (g) plate No.1: PT (PCT: EOF02), (h) plate No.2: PT (PCT: EOF03), (i) plate No.3: PT (PCT: EOF03), (j) plate No.1: VT (PCT: EOF04), (k) plate No.2: VT (PCT: EOF04), (l) plate No.3: VT (PCT: EOF06). 40
4.13 IRT results of SCB: (a) 5 J: 1.65 mm, (b) 10 J: 1.65 mm, (c) 20 J: 1.65 mm, (d) 30 J: 1.65 mm, (e) 5 J: 1.94 mm, (f) 10 J: 1.94 mm, (g) 20 J: 1.94 mm, (h) 30 J: 1.94 mm, (i) 5 J: PT (PCT: EOF), (j) 10 J: PT (PCT: EOF), (k) 20 J: PT (PCT: EOF), (l) 30 J: PT (PCT: EOF), (m) 5 J: VT (PCT: EOF), (n) 10 J: VT (PCT: EOF), (o) 20 J: VT (PCT: EOF), (p) 30 J: VT (PCT: EOF). . . 41

4.14 Phase-based LT results of SCB: (a) 5 J: 0.95 mm, (b) 10 J: 0.95 mm, (c) 20 J: 0.95 mm, (d) 30 J: 0.95 mm, (e) 5 J: 1.9 mm, (f) 10 J: 1.9 mm, (g) 20 J: 1.9 mm, (h) 30 J: 1.9 mm, (i) 5 J: 4.25 mm, (j) 10 J: 4.25 mm, (k) 20 J: 4.25 mm, (l) 30 J: 4.25 mm. 43

5.1 Photographs of the impact regions (rear side): (a) B, (b) C, (c) BCs, (d) BCa. 47
5.2 Optical excitation thermography configurations: (a) schematic set-up for PT using flashes, (b) schematic set-up for LT and PT using lamps, (c) experimental set-up for PT using flashes, (d) experimental set-up for LT and PT using lamps. 47
5.3 VT configuration, (a) schematic set-up, (b) experimental set-up. 48
5.4 PCT results of PT: (a) B: EOF 04, (b) C: EOF 04, (c) BCs: EOF 04, (d) BCa: EOF 04. 49
5.5 PCT results of VT: (a) B: EOF 03, (b) C: EOF 03, (c) BCs: EOF 04, (d) BCa: EOF 03. 49
5.6 PLST results: (a) B: Loading 01), (b) C: Loading 01, (c) BCs: Loading 01, (d) BCa: Loading 01, (e) B: Loading 02, (f) C: Loading 02, (g) BCs: Loading 02, (h) BCa: Loading 02, (i) B: Loading 03, (j) C: Loading 03, (k) BCs:Loading 03, (l) BCa: Loading 03. 50
5.7 PPT results: (a) B: 0.68 mm, (b) C: 1.05 mm, (c) BCs: 0.87 mm, (d) BCa: 0.87 mm, (e) B: 0.96 mm, (f) C: 1.48 mm, (g) BCs: 1.23 mm, (h) BCa: 1.23 mm, (i) B: 1.19 mm, (j) C: 1.84 mm, (k) BCs: 1.52 mm, (l) BCa: 1.52 mm. . . 52
5.8 LT results: (a) B: 2.15 mm, (b) C: 2.09 mm, (c) BCs: 2.75 mm, (d) BCa: 2.75 mm, (e) B: 3.05 mm, (f) C: 3.31 mm, (g) BCs: 3.88 mm, (h) BCa: 3.88 mm. . 53
5.9 CT slices: (a) B: 0.1 mm, (b) C: 0.1 mm, (c) BCs: 0.1 mm, (d) BCa: 0.1 mm, (e) B: 0.6 mm, (f) C: 0.5 mm, (g) BCs: 0.8 mm, (h) BCa: 0.8 mm, (i) B: 0.8 mm, (j) C: 1.7 mm, (k) BCs: 1.7 mm, (l) BCa: 1.7 mm, (m) B: 1 mm, (n) C: 3 mm, (o) BCs: 2.7 mm, (p) BCa: 2.7 mm, (q) B: 3.3 mm, (r) C: 3.3 mm, (s) BCs: 3.3 mm, (t), BCs: 3.3 mm. 54

6.1 Typical dry-core in a non-stitched CFRP T-Joint (microscopic inspection). . . 58
6.2 (a) The complete 3D fabrication model, (b) a high-resolution photography of the preform, (c) the procedure of a triangular-shaped noodle processing for T-joint insertion. 59
6.3 (a) The textile unit cell model (mm), (b) the single layer preform model. 60
6.4 The model geometrical relation. 60
6.5 (a) Complete stitched 3D T-joint sample, (b) front side of the sample. 61
6.6 Microscopic inspection results of T-joint CFRP (a) top-section, (b) cross-section. 62
6.7 UT results of T-joint CFRP (2.25 MHz) (a) pulsed-echo, (b) through-transmission, (c) color scale for signal amplitude percent. 63
6.8 (a) Classical PT set-up[4], (b) experimental set-up. 64
6.9 PT results of T-joint CFRP (a) first derivative, (b) second derivative. 64
6.10 (a) Classical VT set-up[4], (b) experimental set-up. 64
6.11 VT results of T-joint CFRP. 65
6.12 (a) Classical LST set-up[5], (b) experimental set-up[6]. 65
6.13 (a) image prior to heating, (b) heating spot. 66
6.14 ST results of T-joint CFRP (locked-in method) (a) surface, (b) depth: 0.21 mm, (c) depth: 0.65 mm 66

6.15 (a) Micro-laser line thermography experimental set-up, (b) laser spot to laser line. . . . 67
6.16 The x-ray tomography results (a) surface, (b) depth: 90 μm, (c) depth: 0.18 mm. 68
6.17 The micro-laser line thermography results (a) cold image, (b) raw image with contrast adjustment, (c) PCT. . . . 69
6.18 The geometrical model. . . . 71
6.19 (a) The micro-CT measurements (surface), (b) the corresponding model geometrical parameters, (c) the geometrical parameters of the porosities A and B. . . . 72
6.20 (a) surface temperature distribution (heating time: 0.5 s), (b) slice temperature distribution (heating time: 0.5 s), (c) surface temperature distribution from top view. . . . 73
6.21 Slice temperature distribution from top view when the heating time is 0.5 s: (a) surface, (b) depth: 50 μm, (c) depth: 0.1 mm, (d) depth: 0.2 mm, (e) depth: 0.5 mm. . . . 74
6.22 Slice temperature distribution from side view: (a) heating time: 0.5 s, (b) heating time: 1 s. . . . 75
6.23 The simulation results after the corresponding image processing: (a) CIS, (b) PCT. . . . 75
6.24 Lock-in micro-LLT set-up: (a) experimental set-up, (b) schematic set-up. . . . 77
6.25 Micro-LST experimental set-up. . . . 78
6.26 Micro-CT slices (a) surface, (b) depth: 90 μm, (c) depth: 0.18 mm, (d) depth: 0.414 mm. . . . 79
6.27 Micro-LLT results (a) pulse: 0.5 s, cold image, (b) lock-in: 5 Hz, PCT (EOF 8), (c) lock-in: 5 Hz, FT amplitude, (d) lock-in: 5 Hz, FT amplitude (defects marked) (e) lock-in: 1 Hz, FT amplitude, (f) lock-in: 1 Hz, FT amplitude (defects marked) (g) lock-in: 5 Hz, FT phase, (h) lock-in: 1 Hz, FT phase. . . . 80
6.28 Micro-LST results (a) pulse: 0.5 s, cold image, (b) lock-in: 1 Hz, PCT (EOF 5), (c) lock-in: 1 Hz, FT amplitude, (d) lock-in: 1 Hz, FT phase. . . . 81
6.29 Micro-VT experimental set-up. . . . 82
6.30 Micro-VT results (a) pulse: 10 s, (b) pulse: 10 s (defects marked). . . . 82

7.1 “James Abbott McNeill Whistler, Arrangement in Grey and Black, No. 1: *Portrait of the Painter's Mother*, 1871, oil on canvas, 144.3 cm × 162.4 cm, Musée d'Orsay, Paris". . . . 88
7.2 The photographs of the paintings on canvas: (a) the canvas A, (b) the canvas B, (c) the textile support made from hemp and nettle, (d) the textile support made from flax and juniper. . . . 89
7.3 CW sub-THz imaging system: (a) schematic set-up in reflection mode, (b) schematic set-up in transmission mode, (c) experimental set-up in reflection mode, (d) experimental set-up in transmission mode. . . . 90
7.4 PT set-up using flash: (a) schematic set-up, (b) experimental set-up. . . . 90
7.5 CW THz results: (a) painting on canvas A in reflection mode, (b) canvas A in transmission mode, (c) painting on canvas B in reflection mode, (d) canvas B in transmission mode. . . . 91
7.6 PCT results: (a) painting A: EOF 02, (b) painting A: EOF 03, (c) painting A: EOF 04, (d) painting B: EOF 02, (e) painting B: EOF 03, (f) paint B: EOF 04. 92

7.7 PLST results: (a) painting A: Loading 01, (b) painting A: Loading 02, (c) painting A: Loading 03, (d) painting B: Loading 01, (e) painting B: Loading 02, (f) paint B: Loading 03. 93

Abbreviations

B-TSR Basic thermographic signal reconstruction

BCa Basalt-carbon fiber hybrid composite with alternately stacked structure

BCs Basalt-carbon fiber hybrid composite with sandwich-like structure

BFRP Basalt fiber reinforced polymer

CFRP Carbon fiber reinforced polymer

CH Culture heritage

CIS Cold image subtraction

CT X-ray computed tomography

CW Continuous wave

EOF Empirical Orthogonal Function

FEA Finite element analysis

IRT Infrared thermography

JHFP Jute-hemp fiber hybrid polymer laminate

LLT Laser line thermography

LST Laser spot thermography

LT Lock-in thermography

Micro-CT X-ray micro-computed tomography

Micro-LLT Micro-laser line thermography

Micro-LST Micro-laser spot thermography

Micro-VT Micro-vibrothermography

NDT Nondestructive testing

PCT Principal component thermography

PLST Partial least squares thermography

PPT Pulse phase thermography

PT Pulsed thermography

PW Plain weave

SCB Homogeneous Particleboards of Sugarcane Bagasse

THz Terahertz

TW Twill weave

US Unidirectional stitched

UT Ultrasonic C-scan

VT Vibrothermography

Dédicace si désiré

Texte de l'épigraphe

Source ou auteur

Acknowledgements

The last five years of my life has been filled with wonderful and challenging experiences for many reasons and I have a lot to be grateful for.

I would like to express my sincere gratitude and appreciation to my supervisor, Professor Xavier Maldague, for providing me guidance and encouragement. I appreciate the opportunity to work in such a professional but friendly environment.

I want to thank all the members of the Computer Vision and Systems Laboratory at Laval University. Specially I would like to mention Dr. Clemente Ibarra-Castanedo who helped me a lot during my Ph. D. and is always willing to help, listen and discuss new ideas; and Dr. Annette Schwerdtfeger who always so kindly helped me revising my texts.

I am very grateful for the collaboration with all team members of the CRIAQ COMP-501 project. Specially I would like to thank Prof. François Robitaille and Prof. Simon Joncas who helped me with the composite samples. Additionally the financial support of the industrial partners: Bell Helicopter (Canada) Inc., Bombardier Inc., Hutchinson Inc., Delastek Inc., Texonic Inc., CTT group through the following agencies: Natural Sciences and Engineering Research Council of Canada (NSERC), Consortium for Research and Innovation in Aerospace in Quebec (CRIAQ) and Canada Research Chair in Multipolar Infrared Vision (MiViM).

I would also like to acknowledge the bilateral project supported by the governments of Québec and Bavaria, Ministère des Relations Internationales and Ministry of External Affairs. Specially the support of Dr. Ulf Hassler from Fraunhofer EZRT (Germany).

I would also like to thank Dr. Stefano Sfarra from University of L'Aquila (Italy) and Marc Genest from National Research Council (NRC) Canada for their assistance.

I also want to extend my gratitude and appreciation to the thesis committee members for their time to read this thesis and for their valuable recommendations that contributed for the enrichment of the final version of this document.

Introduction

Background

Quality control (QC) is playing an increasingly important role for modern industrial production. This enhances the need of advanced image diagnostic techniques [7]. Image diagnostics has been applied in many sectors of QC, e.g., monitoring of electronic chips or dies in semiconductor production lines, defect inspection during automatic manufacturing and damage detection of composite materials in the aerospace industry, etc [8; 9]. Image diagnostics includes a wide group of analytical techniques used in science and industry to evaluate the properties of materials, components, or systems preventing potential damages after manufacturing or in service [10; 11]. During the manufacturing and applications of composite materials, besides employing advanced manufacturing techniques to raise the production rate, the utilization of reliable and cost-effective condition monitoring, fault diagnosis, non-destroctive testing (NDT), and structural health monitoring is very important [12; 13; 14]. In this direction, the inspection of post-impact damages of industrial aerospace composite materials via image diagnostic techniques is becoming more and more common [15].

Infrared thermography (IRT) technique is based on the recording of images and is gaining increasing attention in the recent years due to its fast inspection rate, contactless nature, spatial resolution and acquisition rate improvements of infrared cameras. In addition, the development of advanced image processing techniques plays an important role in its exponential increment [16; 17]. IRT can be used to assess and predict the structural integrity beneath the surface by measuring the distribution of infrared radiation and converting the measurements into a temperature scale [18]. Among the whole set of experimental set-ups, optical excitation thermography has been applied due to its ability to retrieve quantitative information concerning the defects. In addition, mechanical excitation thermography is also attracting increasing attention due to the powerful excitation approach.

The thesis is based on the image diagnosis and evaluation of different composite materials by IRT, ultrasonic C-scan (UT), X-ray computed tomography (CT) and continuous wave terahertz imaging (CW THz) for the comparative purpose. In addition, new IRT techniques are also proposed.

Research Objective

The main objective of the research is to evaluate different composite materials by IRT, UT, CT and CW THz for the comparative purpose. Advanced image processing technique will also contribute to the evaluation. New IRT techniques are also proposed to address the new issues in the field of NDT&E. Finally, a comprehensive and comparative analysis based on image diagnostics was conducted in view of potential industrial applications.

Organization

The thesis is organized into 7 chapters.

In Chapter 1, different NDT&E techniques are reviewed: 1) optical excitation thermography including PT and LT, 2) UT, 3) CT, 4) CW THz.

In Chapter 2, the common and recently developed data analyzing and image processing methods are reviewed: 1) pulsed phase thermography (PPT), 2) partial least square thermography (PLST), 3) principal component thermography (PCT), 4) basic thermal signal reconstruction (B-TSR), 5) cold image subtraction (CIS).

In Chapter 3, optical excitation thermography was used to evaluate six carbon fiber dry preforms with different textile structures, thicknesses and defects. Comprehensive comparisons were conducted for: 1) providing the thermographic characteristics of different preforms; 2) summarizing the capability of image diagnostic/processing techniques; and 3) offering the most feasible monitoring modality for industrial manufacturing.

In Chapter 4, optical and mechanical excitation thermography were used to evaluate impacted mineral and vegetable fiber composites including basalt fiber reinforced polymer laminates (BFRP), jute/hemp fiber hybrid polymer laminates (JHFP), and homogeneous particleboards of sugarcane bagasse (SCB). In addition, UT and CW THz imaging were also carried out on the mineral fiber laminates. Finally, a comprehensive comparison of different techniques for natural fiber composites detection was conducted.

In Chapter 5, optical and mechanical excitation thermography were used to investigate basalt fiber reinforced polymer (BFRP), carbon fiber reinforced polymer (CFRP) and basalt-carbon fiber hybrid specimens subjected to impact loading. Of particular interest, two different hybrid structures including sandwich-like and intercalated stacking sequence were used. In particular, PT and LT were compared with x-ray computed tomography (CT) for validation.

In Chapter 6, a new micro-laser line thermography (micro-LLT) is presented. X-ray micro-computed tomography (micro-CT) was used to validate the infrared results. Then, a finite element analysis (FEA) is performed. The geometrical model needed for finite element discretization was developed from micro-CT measurements. The model is validated for the experimental results. The same infrared image processing techniques were used for the ex-

perimental and simulation results for comparative purposes. In addition, a new micro-laser spot thermography (micro-LST) and micro-vibrothermography (micro-VT) were also proposed thanks to the use of micro-lens. Finally a comparison of micro-laser excitation thermography and micro-ultrasonic excitation thermography is conducted.

In Chapter 7, a CW THz (0.1 THz) imaging system was used to inspect paintings on canvas both in reflection and in transmission modes. In particular, two paintings were analyzed: in the first one, similar materials and painting execution of the original artwork were used, while in the second one, the canvas layer is slightly different. Flash thermography was used herein together with the THz method in order to observe the differences in results for the textile support materials. The canvas textiles can be considered as composite materials.

Chapter 1

A Review of NDT&E techniques

In this chapter, we will review the modern NDT&E techniques proposed in the literature.

1.1 Optical Excitation Thermography in this research

Optical excitation thermography includes pulsed thermography (PT) and lock-in thermography (LT) experimental set-ups among others.

In PT, photographic flashes or high-energy lamps are used to generate a heat pulse on the specimen surface. The heat transmits itself through the specimen, by diffusion, and then returns to the specimen surface. As time elapses, the surface temperature decreases uniformly for a specimen without internal flaws. On the contrary, subsurface discontinuities can be thought of as resistances to heat flow that change the diffusion rate and produce abnormal temperature patterns at the surface. If these patterns are large enough, then they can be detected with an IR camera and only a few mK as $\triangle$T is needed for the detection of thermal imprints using modern thermographic imaging equipment [4; 19].

The Fourier equation for the propagation of a Dirac heat pulse in a semi-infinite isotropic solid by conduction is:

$$T(z,t) = T_0 + \frac{Q}{\sqrt{k\rho c_p \pi t}} e(-\frac{z^2}{4\alpha t}) \tag{1.1}$$

where, $Q[J/m^2]$ is the energy absorbed by the surface and $T_0[K]$ is the initial temperature.

The Dirac heat pulse consists of periodic waves at all frequencies and amplitudes. A photographic flash provides an approximately square-shaped heat pulse, which can be considered as a convenient approximation. Therefore, the signal can be decomposed by periodic waves at several frequencies. The shorter the pulse, the broader the range of frequencies.

LT, derived from photothermal radiometry, is also known as a modulated technique. In LT configuration, the absorption of modulated optical heating leads to a temperature modulation,

which transmits itself through the specimen as a thermal wave. When the thermal wave is reflected by the defect boundary, the superposition to the original thermal wave will lead to the transformation of the response signal amplitude and phase on the surface. These signals are simultaneously recorded by the IR camera. Photothermal radiometry is a raster point-by-point technique which requires a long acquisition time, especially for deep defects (low modulation frequencies). Sinusoidal waves are typically used in LT, which has the following advantages: 1) frequency and shape of the response are preserved, and 2) only the amplitude and phase delay of the wave may change [4; 19].

Heat diffusion through a solid can be described by Fourier's law of heat diffusion [20]:

$$\bigtriangledown^2 T - \frac{1}{\alpha} \cdot \frac{\partial T}{\partial t} = 0 \tag{1.2}$$

where, $\alpha = k/\rho c_p [m^2/s]$ is the thermal diffusivity of the material, $k[W/mK]$ is thermal conductivity, $\rho[kg/m^3]$ is the density, and $c_p[J/kgK]$ is the specific heat at constant pressure.

Fourier's law for a periodic thermal wave propagating through a semi-infinite homogeneous material can be expressed as [21]:

$$T(z,t) = T_0 e^{(-z/\mu)} cos(\frac{2\pi \cdot z}{\lambda} - \omega t) \tag{1.3}$$

where, $T_0[^\circ C]$ is the initial temperature change, $\omega = 2\pi f[rad/s]$ is the modulation frequency, $f[Hz]$ is the frequency, $\lambda[m]$ is the thermal wavelength: $\lambda = 2\pi\mu$, and $\mu[m]$ is the thermal diffusion length, which determines the rate of decay of the thermal wave as it penetrates through a material:

$$\mu = \sqrt{\frac{2 \cdot \alpha}{\omega}} = \sqrt{\frac{\alpha}{\pi \cdot f}} \tag{1.4}$$

The amplitude and the phase delay can be calculated from the Fourier transform as detailed in section 2.1.

1.2 Mechanical Excitation Thermography

Vibrothermography (VT) uses mechanical waves to stimulate internal defects without heating the surface as in optical excitation thermography. Photothermal radiometry can be considered as the predecessor of optical thermography; VT should be the successor of optoacoustics or photoacoustics phenomena in which microphones or piezoceramics in contact with the specimen and a lock-in amplifier were used to detect the thermal wave signature from a defect. In VT, ultrasonic waves travel through a specimen, in which an internal defect results in a complex combination of absorption, scattering, beam spreading and dispersion of the waves. The waves generate heat which subsequently travels by conduction in all directions [22]. An IR camera faces the surfaces of the specimen to capture the defect signature [4].

1.3 Ultrasonic C-scan (UT)

Ultrasonic C-scan is a well-established NDT method which has the ability to detect flaws in either the partial or entire thickness of the materials[23]. It has been widely used to detect flaws in metals[24]. It is also increasingly used to detect composites due to its flexibility and convenience.

It is a challenge to detect thick 3D CFRP using ultrasonic c-scan due to its complex internal structure. The complex internal structure can cause attenuation and scattering of ultrasonic beams[25]. Ultrasonic c-scan has been widely used to detect voids and laminates in composites[26].

1.4 X-ray Computed Tomography (CT)

The division between what is considered 'conventional' computed tomography and 'micro-tomography' is an arbitrary one, but generally the term micro-tomography is used to refer to results obtained with at least 50-100 μm spatial resolution [27]. CT has become a familiar technique. Recently it is also increasingly gaining popularity as an accessible laboratory technique for NDT of materials and components, especially due to the recent appearance of several commercial systems. Such instruments offer the potential for the widespread use of micro-CT as a tool for characterization of damage in composite materials [28].

Application of micro-CT to composite materials was concentrated on metal-matrix and ceramic-matrix composites in the past. The spatial scale of features in these materials including fiber location and waviness [29], fiber breakage [30], local porosity and density [31], void volume [32], fatigue crack growth [33], etc. are accessible to micro-CT. However, recently some studies on polymer matrix composites have also been reported. In 2000, impact damage including fiber fracture and delamination in T300/914 carbon fiber/epoxy laminates was characterized [34]. In 2002, impact damage in an epoxy/E-glass composite was also measured [35]. In 2004, micro-CT was used to determine internal structure in a polymer foam reinforced with short fibers [36]. In 2005, a study was undertaken to assess the capabilities and limitations of micro-CT for fiber-reinforced polymer-matrix composites, where different specimens with a variety of damage types, geometries and dimensions were investigated to assess the effect of the system resolution on the ability to determine the internal geometry of flaws including delamination, matrix crack, and especially micro-crack, which is a subject of critical interest in the study of fiber-reinforced polymer-matrix composite laminates [28]. In 2006, an evaluation of micro-CT was performed to determine the geometry of fiber bundles and voids in glass fiber reinforced polymers (GFRP). As a consequence, each fiber bundle and inter bundle voids can be observed separately [37].

1.5 Continuous Wave Terahertz Imaging (CW THz)

The electromagnetic waves range inherent to THz spectroscopy is located between 0.1 THz and 10 THz. THz wave generation is a challenge because the THz range is located at the boundary of electronics (based on the motion of electrons) and the photonics (based on the atomic transitions of electrons) modes of EM wave generation. However, the development of photonics and electronics in recent years has enabled the compact yet sophisticated THz imaging systems [38]. The principles of continuous wave (CW) imaging has been known for several decades [39; 40]. Pulse imaging can provide depth, frequency-domain or time-domain information of the object, while CW imaging can only yield intensity data using a fixed frequency source and a single detector [41]. However, in THz imaging, a CW imaging system is compact, simple and relatively low-cost without a pump–probe system. Simultaneously, the complexity of the optics involved can be greatly reduced [42]. A recent THz time-domain system uses a shaker-technique to reduce measurement time, so the total observation time depends on scanning itself. Therefore, both pulse and CW THz systems can provide fast scanning. Regarding scientific research, simplicity is the main advantage of CW THz while the key advantage of pulse THz is flexibility, in which all the information is recorded within a single measurement to be processed in order to acquire the needed information for different applications. Since the frequency spectrum of CW THz is narrow, a large F-number Fresnel lens can be used to increase the resolution by focusing onto a spot [43].

In order to introduce the reader to the “result analysis" section it is important to describe the main physical concepts at the base of the THz method, as well as the experimental set up used to record the data. Usually, materials have different reflection and absorption coefficients for THz radiation, *e.g.*, metals are better reflectors, polar liquids such as water are excellent absorbers, and anisotropic materials such as composites have variable reflectance relative to the fibre direction. The THz refractive indices and absorption coefficients are related to the material's structure and properties. The Claausius-Mossotti equation (Eq. 1.5) [44] is usually used to calculate the refractive indices, which links the dielectric constant ε to the microscopic polarizability P,

$$\frac{\varepsilon - 1}{\varepsilon + 2} = \frac{4\pi}{3} N_A \frac{\rho}{M} P \tag{1.5}$$

where N_A is Avogadro's number, ρ is the mass density, and M is the molecular weight.

The model developed by Schlömann [45] and Strom [46] is usually used to calculate the absorption coefficients. The model explains far-infrared absorption in amorphous materials in terms of disorder-induced coupling of radiation into the acoustic photon modes [47].

CW THz wave propagations in uniform solid materials is linear, and the transmission intensity can fit Beer's Law very well. For instance, in case of wood inspection, it is known that spruce

absorption correlates with its density in the THz range, and this can be used for density mapping [48]. The derived CW THz absorption coefficient of various timbers can be obtained as follows [49]:

$$\frac{\alpha}{\rho} \approx 4.69 \tag{1.6}$$

where, $\alpha[cm^{-1}]$ is the absorption coefficient at 0.1 THz and $\rho[gcm^{-3}]$ is the material density.

Chapter 2

Infrared Image Processing

In this chapter, we will review the infrared image processing techniques proposed in the literature.

2.1 Pulsed Phase Thermography (PPT)

Discrete Fourier transform (DFT), or more precisely fast Fourier transform (FFT) on thermographic data was first proposed by Maldague and Marinetti in 1996 [50]. DFT can be used to extract amplitude and phase information from LT and PT data. DFT can be written as [51]:

$$F_n = \triangle t \sum_{k=0}^{N-1} T(k \cdot \triangle t) exp^{(-j2\pi nk/N)} = Re_n + Im_n \tag{2.1}$$

where, j is the imaginary number ($j^2 = -1$), n designates the frequency increment ($n = 0, 1, \ldots N$), $\triangle t$ is the sampling interval, Re and Im are the real and the imaginary parts of the transform, respectively.

Re and Im are used to estimate amplitude and phase [52]:

$$A_n = \sqrt{Re_n^2 + Im_n^2} \tag{2.2}$$

$$\phi_n = tan^{-1}(\frac{Im_n}{Re_n}) \tag{2.3}$$

DFT can be used with any waveform and has the advantage of de-noising the signal. FFT can also be implemented instead of DFT for phase and amplitude transform due to its fast processing. The most important characteristic of phase and amplitude transform is that they provide the possibility to obtain quantitative results in a straightforward manner. A relationship exists between the depth z of a defect and the thermal diffusion length μ. Physico-mathematical expressions have been proposed, such as:

$$z = C_1 \cdot \mu = C_1 \cdot \sqrt{\frac{\alpha}{\pi \cdot f_b}} \tag{2.4}$$

where, f_b is known as the blind frequency - the frequency at which a given defect has enough (phase or amplitude) contrast to be detected, while C_1 is calculated after a series of experiments.

It has been observed that $C_1 \approx 1$ for amplitude transform [53], while reported values for phase transform are in the range of 1.5 to 2 [53], with $C_1 = 1.82$ typically adopted for similar cases such as the present [54]. Therefore, for NDT applications, phase transform is more important than amplitude because it can retrieve the deeper information. The frequency components can be derived from the time spectra as follows:

$$f_n = \frac{n}{N \cdot \triangle t} \tag{2.5}$$

where, n designates the frequency increment ($n = 0, 1, \ldots N$), $\triangle t$ is the time step, and N is the total number of frames in the sequence.

Phase ϕ_n is particularly important because it is less affected than raw thermal data by environmental reflections, emissivity variations, non-uniform heating, surface geometry, and orientation. These phase characteristics are very attractive not only for qualitative inspections but also for quantitative characterization of materials [19; 4]. This technique is also known as pulse phase thermography (PPT) [50].

2.2 Partial Least Square Thermography (PLST)

Partial least square (PLS) methods relate the information present in two data tables that collect measurements on the same set of observations. PLS methods proceed by deriving latent variables which are optimal linear combinations of the variables of a data table. Indeed, one of the advantages of these techniques is the possibility of analyzing simultaneously two matrices X and Y, taking into account the relationship between each other. One of these matrices is necessarily the data matrix, the second one could be the time vector or a model matrix. After choosing a number of components c (usually, similar to the useful components in principal component analysis – PCA) PLS performs the simultaneous decomposition of both X and Y. Mathematically, PLS is expressed as follows:

$$X = T \cdot P^T + E \tag{2.6}$$

$$Y = U \cdot Q^T + F \tag{2.7}$$

where, P and Q are defined as loadings, T is an orthogonal matrix defined as scores and E and F are residuals. If $X \in R^{nxs}$ and $Y \in R^{nxm}$, then the loading $P \in R^{sxc}$, the loading $Q \in R^{mxc}$ and the score $T \in R^{nxc}$. In Equations 2.6 and 2.7, $T(n \times a)$ is known as the scores matrix and its elements are denoted by $t_a(a = 1, 2, \ldots, A)$. The scores can be considered as a small set of underlying or latent variables responsible for the systematic variations in X.

The matrices $P(N \times a)$ and $Q(M \times a)$ are called loadings (or coefficients) matrices and they describe how the variables in T relate to the original data matrices X and Y. Finally, the matrices $E(n \times N)$ and $F(n \times M)$ are called residuals matrices and they represent the noise or irrelevant variability in X and Y, respectively.

It can be noted in Equations 2.6 and 2.7 that the X-scores (T) are predictors of Y and also model X, *i.e.*, both Y and X are assumed to be, at least partly, modeled by the same latent variables. The scores are orthogonal and are estimated as linear combinations of the original variables x_k with the coefficients, called weights, $x_{ka}(a = 1, 2, \ldots, A)$. Thus, the scores matrix T is expressed by:

$$T = X \cdot W \tag{2.8}$$

Once the scores matrix T is obtained, the loadings matrices P and Q are estimated through the regression of X and Y onto T. Next, the residual matrices are found by subtracting the estimated versions of TP_T and TQ_T from X and Y, respectively. Finally, the regression coefficients for the model are obtained using Equation 2.8:

$$B = W \cdot Q^T \tag{2.9}$$

which yields the regression model:

$$Y = XB + F = XWQ^T + F \tag{2.10}$$

The decomposition of the predictor X matrix is carried out using the nonlinear iterative partial least square (NIPALS) algorithm.

The application of PLRS to the square pulsed thermography (SPT) data is achieved by decomposing the raw thermal data into multiple PLS components, each component being orthogonal to each other. Since each of the PLS components is characterized by its variance, it is possible to identify via the PLS components different phenomena affecting the overall thermal regime. The thermal images obtained during the SPT inspection are typically arranged into a 3D matrix, whose x and y axes are represented, respectively, by i and j pixels, while the z axis corresponds to the k frame number. N_x and N_y correspond to the total number of pixels along the x and y directions, while N_T is the total number of frames (Fig. 2.1).

In order to perform the decomposition of the thermal data sequence into PLS components, it is firstly necessary to transform the 3D thermal data into a 2D raster-like matrix, as shown in Fig. 2.1. This process is known as unfolding. The unfolded X matrix (corresponding to the thermal sequence) has dimensions $N_T \times N_x \cdot N_y$ and physically represents NT observations (or samples) of $N_x \cdot N_y$ variables (or measurements). On the other hand, the dimension of the predicted matrix Y – defined by the observation time during which the thermal images were captured – is $N_T \times 1$. More information regarding the PLST technique can be found in [55].

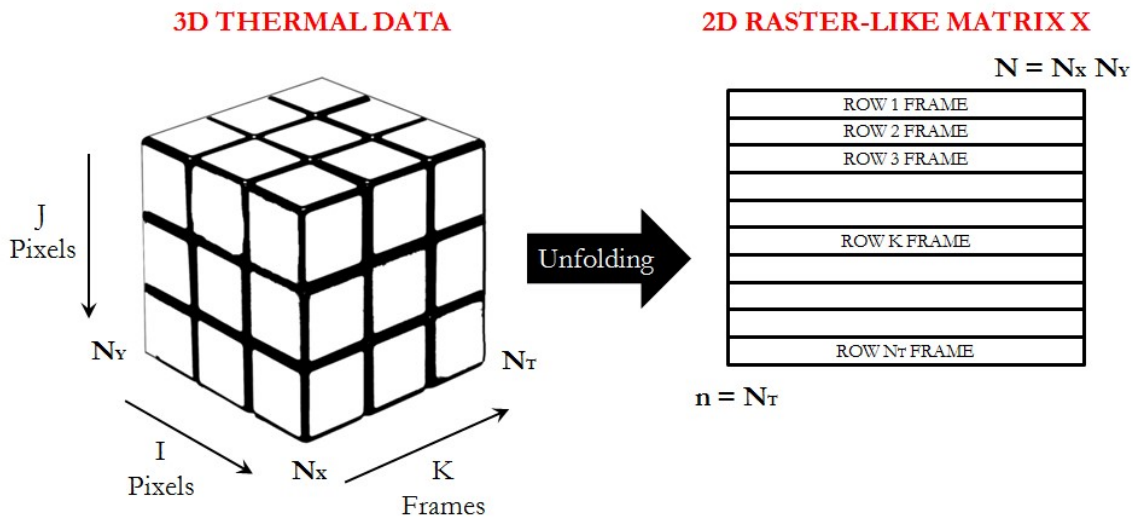

Figure 2.1: Schematic representation of the transformation of the 3D thermal data into a 2D raster-like matrix.

2.3 Principal Component Thermography (PCT)

Principal Component Analysis (PCA) used to process thermographic sequences to extract features and reduce redundancy by projecting the thermal response data onto a system of orthogonal components is known as PCT [56].

The PCA is a linear projection technique for converting a matrix A to a matrix of the lower dimension by projecting A onto a new set of principal axis. One simple approach to the PCA is to use Singular Value Decomposition (SVD). In general, a matrix A of the dimension $M \times N$ $(M > N)$ can be decomposed as [57]:

$$A = URV^T \tag{2.11}$$

where U is the eigenvector matrix of the dimension $M \times N$, R is an $N \times N$ diagonal matrix with positive or zero elements representing the singular values of matrix A, VT is the transpose of an $N \times N$ matrix.

For PCT, in order to apply the SVD to thermographic data, the 3D thermogram matrix representing time and spatial variations has to be reorganized as a 2D $M \times N$ matrix A [58; 2]. This can be done by rearranging the thermograms for every time as columns in A, as illustrated in Fig. 2.2a [2]. Under this configuration, the columns of U represent a set of orthogonal statistical modes known as Empirical Orthogonal Functions (EOFs) that describe the data spatial variations. On the other hand, the Principal Components (PCs), which represent time variations, are arranged row-wise in matrix VT. The resulting U matrix that provide spatial information can be rearranged as a 3D sequence as illustrated in Fig. 2.2b [2].

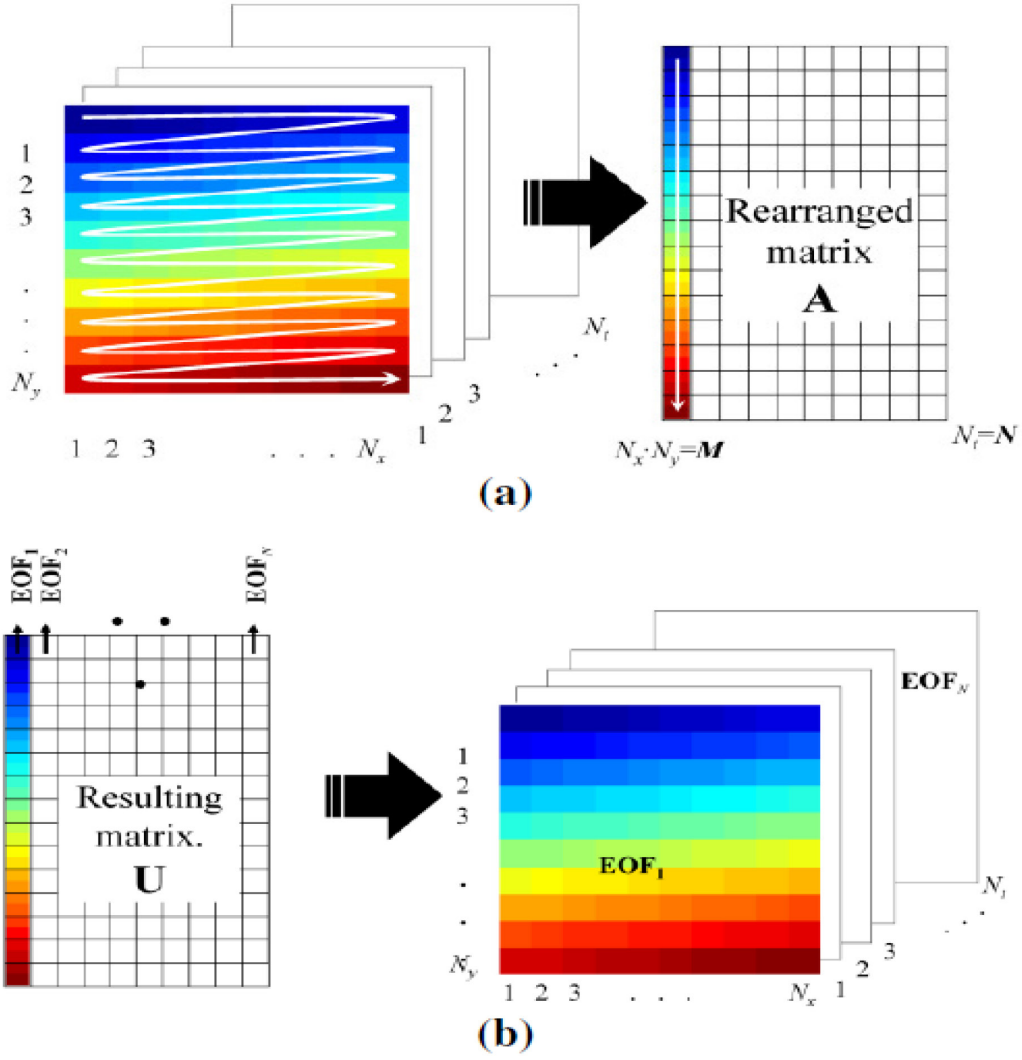

Figure 2.2: (a) Thermographic data rearrangement from a 3D sequence to a 2D A matrix in order to apply SVD, (b) rearrangement of 2D U matrix into a 3D matrix containing the EOFs [2].

Compared with FT that relying on prescribed basis functions (a set of sinusoidal basis functions), PCT method is an eigenvector based transform [57]. It is possible to achieve a compact representation for a complex signal by applying PCT. The first EOF will represent the most characteristic variability of the data; the second EOF will contain the second most important variability, and so on. Usually, 1000 thermogram sequence can be adequately represented with only 10 or less EOFs [58]. Beyond reducing redundancy, PCT is also proposed as a contrast enhancement approach [59].

2.4 Basic Thermographic Signal Reconstruction (B-TSR)

Thermographic Signal Reconstruction (TSR) [3] is widely used in commercial pulsed thermography systems. In TSR, a polynomial function is fit to each pixel time history to minimize temporal noise. Images created from the instantaneous logarithmic time derivatives of the fit function are typically viewed and analyzed, since the derivative images are much more sensitive to subsurface features than the original data sequence from the IR camera. Individual pixel time history derivatives can be evaluated quantitatively for automated evaluation or measurement of depth or thermal diffusivity. Once the polynomials have been calculated for each pixel, the coefficients may be archived instead of the original data sequence, resulting in significant degree of data compression.

It is important, though, to set the duration of pulse heating so as to accommodate the properties of the sample. In particular, TSR is sensitive to transient events during cooling. Therefore, a long heating period and late acquisition may diminish the positive effects of TSR. Fig. 2.3 shows a typical use of TSR on a 8 plies CFRP specimen.

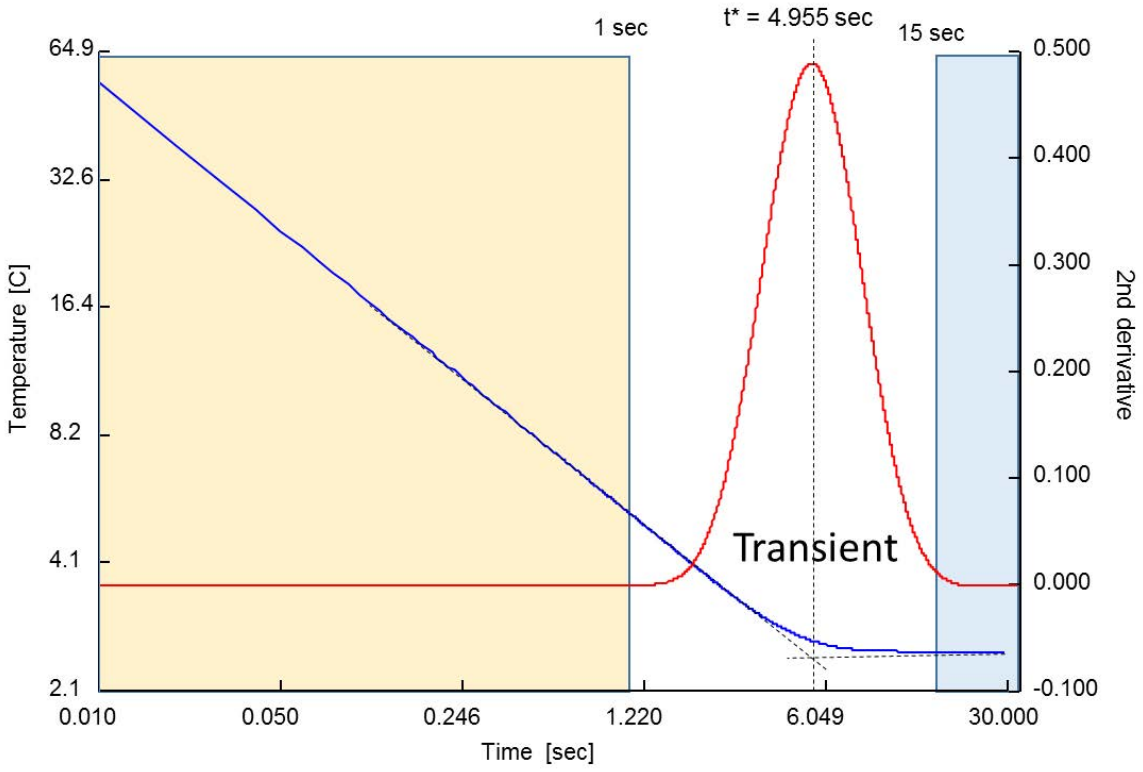

Figure 2.3: Typical use of TSR (model: 8 plies CFRP (0.0125" / ply)) [3]

The implementation of TSR that is used in industrial systems is based on patented and proprietary technology that has optimized specifically for performance with other components

in the system. In this study, we have used the basic form of TSR that has been reported in the literature, which we refer to as "B-TSR". Our polynomial calculation is based on a standard Matlab polynomial fit. Results presented here using B-TSR do not necessarily represent the performance of commercial TSR systems.

2.5 Cold Image Subtraction (CIS)

Cold image subtraction (CIS) is intended to reduce the effects of fixed artifacts in a thermographic sequence. For example, reflections from the environment such as residual heating coming from the lamps and even the reflection from the camera that appears during the acquisition. Since these artifacts are more or less constant during the whole acquisition, including before heating when the image is cold, this image or the average of several images can be subtracted before heating, so their effect can be reduced [60]. Figure 2.4 shows an example with an academic aluminum plate.

In Fig. 2.4, the cold image is affected by noise due to a non-uniform correction (NUC) which was badly performed. This happens when an old NUC is used. The noise can be seen in the raw sequence as well (the 2nd image in Fig. 2.4) although it is less evident since the temperature is higher.

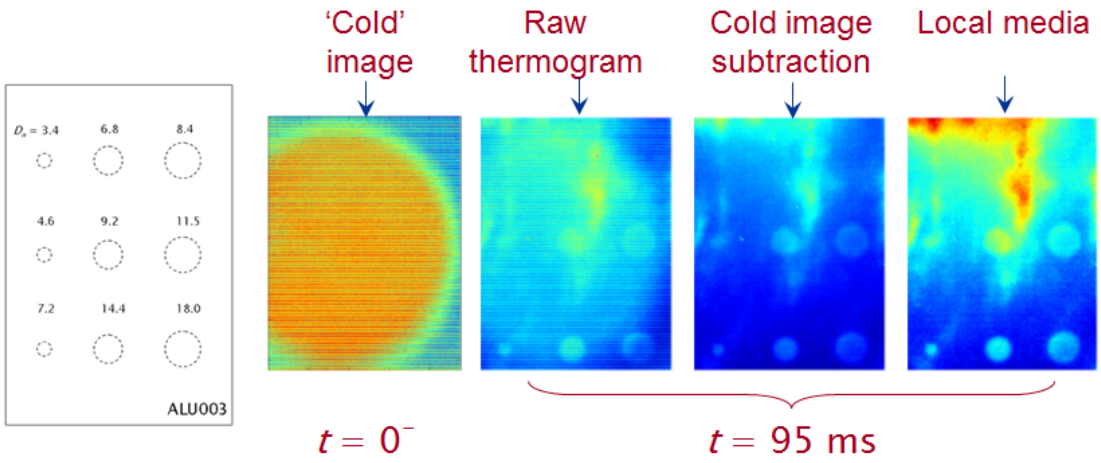

Figure 2.4: An example with an academic aluminum plate to explain cold image subtraction.

Cold image subtraction can be considered as a pre-processing step to improve the quality of the sequence and then one can use more advanced algorithms such as phase pulse thermography, principal component thermography, etc.

Chapter 3

Image Diagnosis for Industrial Carbon Fiber Dry Preform

3.1 Introduction

IRT, as an optical image diagnostic technique, has been used for composite materials [61; 62]. However, IRT use for monitoring of dry preform during industrial manufacturing is poorly documented in the open literature.

CFRP, are preferred for aircraft component construction due to their excellent mechanical properties, e.g. high strength/stiffness and low densities [63; 64]. However, manufacturing costs remain an obstacle to wider use. Nowadays, CFRP are often manufactured using out-of-autoclave liquid molding (LM) processes, which provide flexibility and reduce cost. However, laying down thin reinforcement fabrics during the stacking process results in low reproducibility. The use of advanced preforms, which are manufactured as assembled units, may alleviate this issue. Therefore, NDT is considered as a means of identifying defects in dry preforms during or after lay-down [14; 13]. NDT conducted on dry preforms prior to resin infusion can greatly improve reproducibility and reduce rejection rates. Among NDT techniques, IRT is increasingly and particularly attractive [65; 66].

In this work, pulsed and lock-in thermography were used to evaluate six carbon fiber dry preforms. Two of them are two-layered twill weave fabrics (thickness: ∼0.5 mm), one is a four-layered plain weave fabric (thickness: ∼1 mm), and the other three are stitched fabrics with two layers (thickness: ∼0.5 mm) and four layers (thickness: ∼1 mm). Flashes and halogen lamp set-ups were used, respectively. Quantitative analysis, which is important for NDT techniques, was conducted by phase transform. In addition, advanced image processing techniques including phase transform, CIS, B-TSR, PCT and PLST were used to process the thermographic data for comparative purposes. In particular, PLST, one of the newest advanced post-processing techniques, was extensively applied. Finally, comprehensive comparisons were

conducted for: 1) providing the thermographic characteristics of different preforms; 2) summarizing the capability of image diagnosis/processing techniques; and 3) offering the most feasible monitoring modality for industrial manufacturing.

3.2 Carbon Fiber Dry Preforms

The specimens were made from 3 Texonic carbon fiber fabrics: a 215 g/m^2 2×2 balanced twill weave (TW), a 197 g/m^2 balanced plain weave (PW), and a 285 g/m^2 unidirectional stitched fabric (US). The fabrics were made from Toho Tenax HTS40 fibers. The TW and PW fabrics used 3K yarns while the US fabric used 12K yarns. For each fabric, a 100 mm × 100 mm specimen composed of 2 or 4 layers was prepared. Layers were assembled into preforms using Airtec2 spray adhesive, and each specimen was compacted under 4.6 KPa for 300 seconds. For the TW and PW specimens where the yarns extend along 2 orientations in each ply: 0/90° or ±45° shown in Fig. 3.1, the defects were fabricated by removing yarns. For the

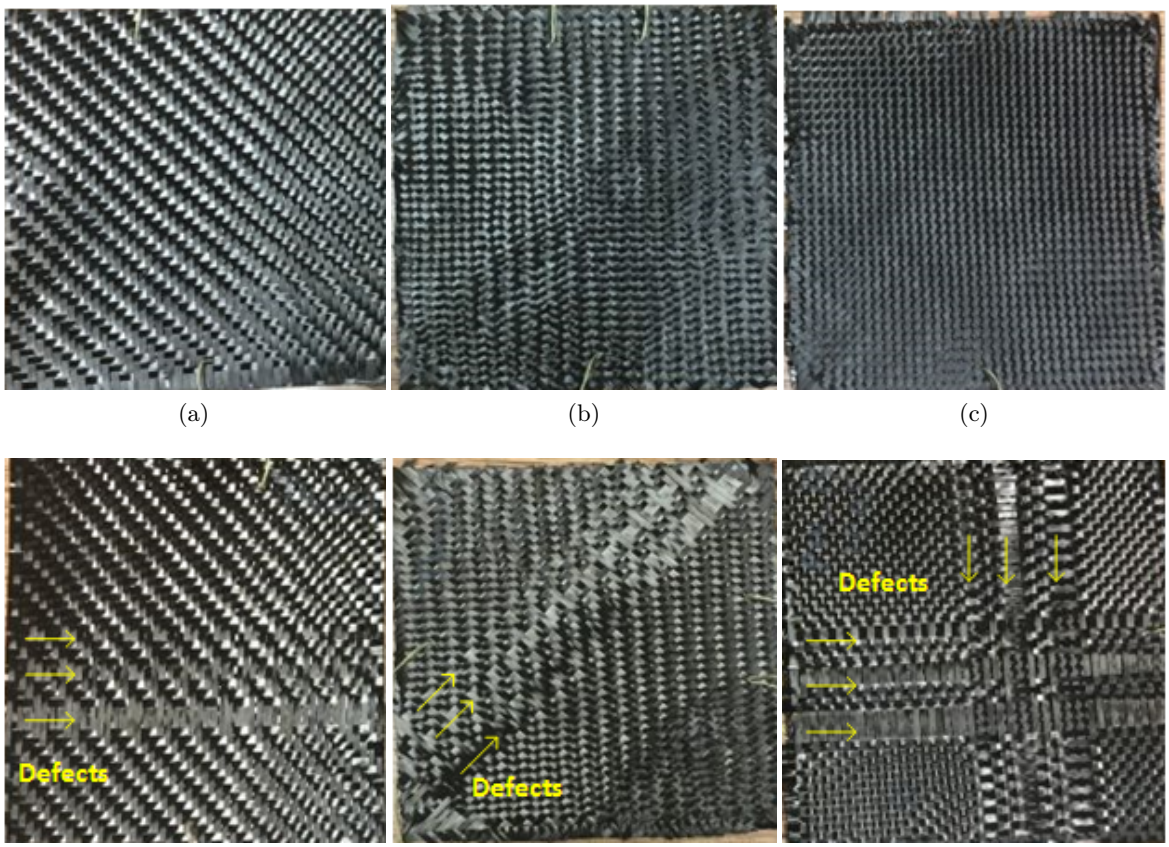

(a) (b) (c)

(d) (e) (f)

Figure 3.1: Photographs of TW and PW specimens: (a) TW-01: front side, (b) TW-02: front side, (c) PW-01: front side, (d) TW-01: rear side, (e) TW-02: rear side, (f) PW-01: rear side.

US specimens shown in Fig. 3.2, two types of defects were realized parallel or perpendicular

to the orientation of yarns by cutting stitches to enable the removal of yarns, or by cutting yarns. The width/orientation of layers and defects are shown in Table 3.1. Measured sample thicknesses were ∼1 mm for PW-01/US-03, and ∼0.5 mm for the other TW/US specimens. The defects selected in this work are typical in manufacturing, and the corresponded NDT is poorly documented in the open literature.

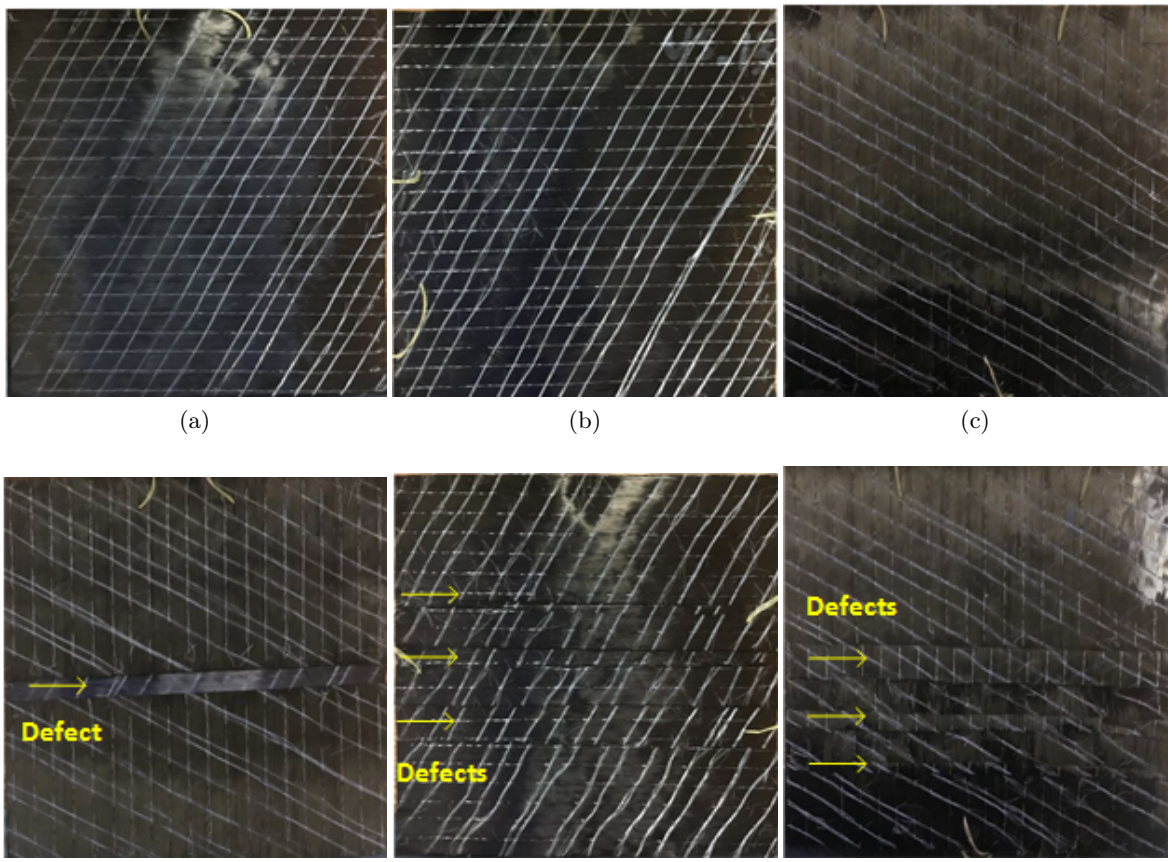

(a) (b) (c)

(d) (e) (f)

Figure 3.2: Photographs of US specimens: (a) US-01: front side, (b) US-02: front side, (c) US-03: front side, (d) US-01: rear side, (e) US-02: rear side, (f) US-03: rear side.

Table 3.1: Orientation/width of layers and defects.

		TW-01	TW-02	PW-01	US-01	US-02	US-03
Orientation of layer		0/90, 0/90	±45, ±45	±45, ±45, ±45, 0/90	0/90	90/90	90/90/90/90
Width & orientation of defect	1/2 yarn						
	1 yarn	⟷	↗	⟷ ↕	⟷	↕	⟷
	2 yarn	⟷	↗	⟷ ↕		↕	⟷
	3 yarn	⟷	↗	⟷ ↕		↕	⟷

⟷: defect along horizontal (0°); ↕: defect along vertical (90°); ↗: defect along right-leaning diagonal (±45°).

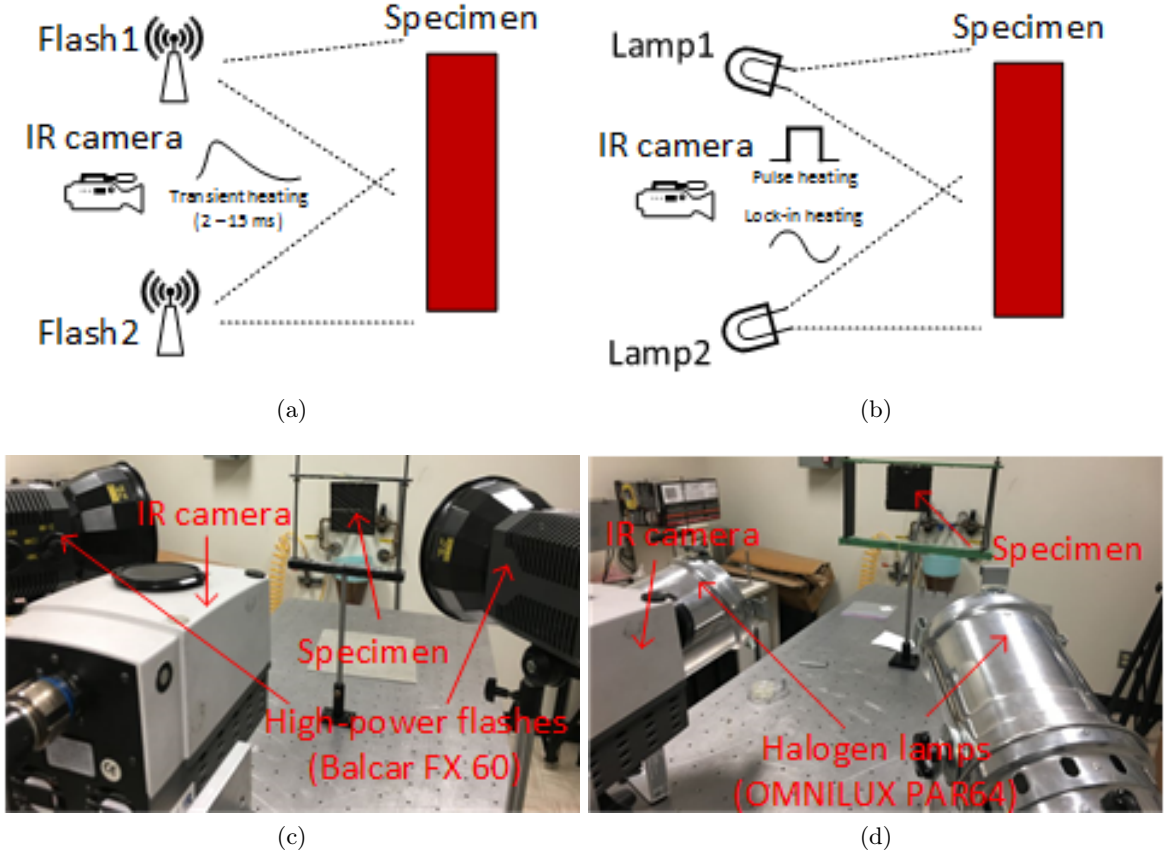

Figure 3.3: Optical excitation thermography set-ups: (a) schematic set-up for PT using flashes, (b) schematic set-up for PT and LT using lamps, (c) experimental set-up for PT using flashes, (d) experimental set-up for PT and LT using lamps.

3.3 Experimental Configurations

Fig. 3.3a and 3.3c show the schematic and experimental set-up for PT using photographic flashes, and two Balcar FX 60 (6.4 KJ each, 5 ms duration) photographic flashes were used in this set-up. Figs. 3.3b and 3.3d show the schematic and experimental set-up for PT and LT using halogen lamps, and two OMNLUX PAR64 (1000 W, 5 s duration) halogen lamps were used correspondingly. A mid-wave IR camera (FLIR Phoenix, InSb, 3 -5 μm, 640 $\times$ 512 pixels) was used to record the temperature profile. Three modalities were used: a) flashes set-up with 300 frames cooling time and 88 fps; b) flashes set-up with 10 s cooling time and 55 fps; and c) halogen lamps set-up with 15 s cooling time and 55 fps. In this work, RMF and CIS were performed prior to phase transform, B-TSR, PCT and PLST in PT; RMF was performed prior to Fourier transform and PCT in LT.

3.4 Experimental Measurement for Thermal Diffusivity

According to Eq. 2.4, the thermal diffusivity α is a parameter of particular interest for calculating the depth by phase transform. α can be obtained by either theoretical calculation or experimental measurement.

In the theoretical calculation method, α can be expressed as follows according to Eq. 1.1:

$$\alpha = \frac{k}{\rho c_p} \tag{3.1}$$

where, $c_p[J/KgK]$ is the specific heat at constant pressure, $\rho[Kg/m^3]$ is the density, and $k[W/mK]$ is the thermal conductivity.

For composite materials, α can be calculated by [67; 68; 69]:

$$\alpha_{composite} = \sum_{1}^{N} (W_f \cdot \alpha_{material})_N \tag{3.2}$$

where, N is the number of constituent materials in the composite, and W_f is the weight fraction material.

Eq. 3.2 is linked to the fact that the α parameter is composed of physical quantities, but not composed of pseudo-physical quantities, as happens for the C_p parameter. Therefore, taking into account the Buckingham theorem, it is possible to sum each layer for its volume fraction and mass fraction, respectively. This enables the obtaining of the final α and volume.

For carbon fiber dry preforms, the properties of both carbon fiber and air properties should both be considered. However, the weight fraction of air is difficult to quantify because of uncertainty over sample thickness. Therefore, an experimental measurement for α is more reasonable in this case.

In the experimental measurement method, the thermal diffusivity can be determined by exposing a sample of the material to a high-intensity, short duration heat pulse in the front face while recording the temperature evolution from the rear face. This approach was originally proposed by Parker [70], based on determination of the time of maximum surface. The diffusivity can be obtained using the known specimen thickness L:

$$\alpha = \frac{0.139 \cdot L^2}{t_{\frac{1}{2}}} \tag{3.3}$$

where $t_{\frac{1}{2}}$ is the time when the temperature reaches half the maximum value.

This technique was later refined using different time parameters. The resulting technique is called the partial times method, in which the following equations were introduced to estimate the diffusivity [71]:

$$\alpha = \frac{L^2}{t_{\frac{5}{6}}}[0.818 - 1.708 \cdot (\frac{t_{\frac{1}{3}}}{t_{\frac{5}{6}}}) + 0.885 \cdot (\frac{t_{\frac{1}{3}}}{t_{\frac{5}{6}}})^2] \tag{3.4}$$

$$\alpha = \frac{L^2}{t_{\frac{5}{6}}}[0.954 - 1.581 \cdot (\frac{t_{\frac{1}{2}}}{t_{\frac{5}{6}}}) + 0.558 \cdot (\frac{t_{\frac{1}{2}}}{t_{\frac{5}{6}}})^2] \tag{3.5}$$

$$\alpha = \frac{L^2}{t_{\frac{5}{6}}}[1.131 - 1.222 \cdot (\frac{t_{\frac{2}{3}}}{t_{\frac{5}{6}}})] \tag{3.6}$$

where, $\alpha[m^2/s]$ is the thermal diffusivity, which corresponds to the mean value of the three results; L is the specimen thickness; $t_{\frac{1}{2}}$, $t_{\frac{1}{3}}$ and $t_{\frac{5}{6}}$ correspond to the times when the temperature is equal to 1/2, 1/3, and 5/6 of the maximum value, respectively.

Estimations from any of these equations provide similar results. Fig. 3.4a shows the experimental measurement modality using the flashes set-up, and Fig. 3.4b shows an example for the calculation of the mean value α. The same IR camera and flashes were used to record the temperature profile. Table 3.2 shows the thermal diffusivity α obtained by theoretical

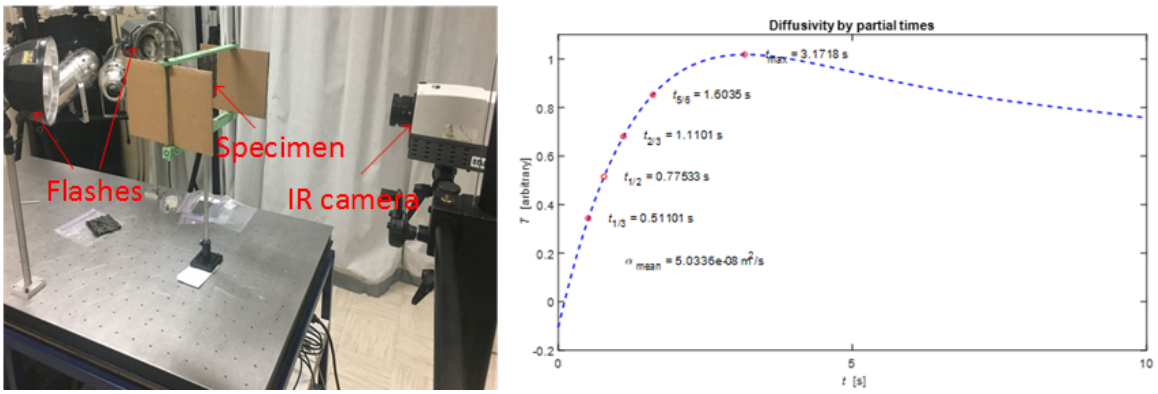

(a) (b)

Figure 3.4: (a) Experimental measurement set-up, (b) an example for the α calculation.

Table 3.2: Thermal diffusivity by theoretical calculation and experimental measurement.

	Specimen	Theoretical calculation	Experimental measurement
Thermal diffusivity α $[10^{-7}m^2/s]$	TW/PW	1.85	~1.6
	US	1.85	~0.5

calculation without considering air, and experimental measurements, respectively. In the theoretical calculation, the following carbon fiber properties were used: $c_p = 1296\ J/KgK$, $\rho = 1790\ Kg/m^3$, k =0.43 W/mK [72]. In the measurements, the TW and PW specimens showed similar thermal diffusivity, and the US specimens showed a similar value among themselves, but different values to TW and PW specimens. Therefore, mean value calculation were performed for the TW/PW and US specimens, respectively. This discrepancy may result from differences in air and carbon fiber value fraction difference, which is difficult to express in theoretical calculations in the case of dry preforms.

The measurement method cannot function properly when the specimen is thick, as heat cannot transfer throughout the specimen. In addition, the measurement is an approximate calculation, in which the specimen thickness plays an important role according to Eqs. 3.4 - 3.6. However, the measurement method is more appropriate than the theoretical calculation in this case due to the lack of information on the air volume fraction. Table 3.3 shows the calculated detection depth z according to the measured thermal diffusivity α and the modulated frequency f_b used in this work.

Table 3.3: Relationship between modulated frequency f_b and detection depth z.

Modulated frequency $f_b[Hz]$		2,9	1.1	0.65	0.35	0.2	0.08	0.065
Depth $z[mm]$	TW/PW	0.25	0.4	0.5	/	0.9	/	1.65
	US	0.15	/	0.3	0.4	0.5	0.8	0.9

3.5 Experimental Results and Analysis

Fig. 3.5 shows the phase transform results for the TW and PW specimens. The flashes set-up and 88 fps was used with a cooling time of 300 frames. Images from depths of 0.25 mm (2.9 Hz), 0.4 mm (1.1 Hz) and 0.5 mm (0.65 Hz) were obtained. Defects in the two-layered TW specimens were detected at a depth of 0.4 mm as shown in Figs. 3.5b and 3.5e, and they can be seen more clearly at a depth of 0.5 mm (Figs. 3.5c and 3.5f). No defects were detected at a depth of 0.24 mm (Figs. 3.5a and 3.5d) since there were no defects located at this depth. Defects were detected with increasingly clear features along with depth. Defects in the four-layered specimen PW-01 (Figs. 3.5g, 3.5h and 3.5i) were not detected as they are located deeper than 0.5 mm.

Fig. 3.6 shows B-TSR and PCT results for TW and PW specimens using the flashes set-up and 88 fps. In B-TSR, the 1st derivative results are clearer. For the four-layered PW specimen, defects were detected by B-TSR and PCT, as shown in Fig. 3.6g and 3.6i. PCT showed clearer results than phase transform, but the lack of quantitative analysis is a significant disadvantage. PLST can also provide additional results along with depth, as shown in Fig. 3.7. In PLST, 1st loading results are nearer to the surface than 2nd loading results, which are shallower than 3rd loading results. Similar to phase transform, defects were also detected with increasingly clear features along with depth. Again, defects in the four-layered specimen PW-01 were not detected. Although phase transform shows clearer results, PLST needs less processing time. However, PLST can only provide qualitative depth information, which is also a disadvantage compared with phase transform.

Fig. 3.8 shows phase transform results for US specimens obtained by the same modality as used for results shown in Fig. 3.5. Images at depths of 0.15 mm (2.9 Hz), 0.3 mm (0.65 Hz) and 0.4 mm (0.35 Hz) were obtained. The defects in the two-layered US specimens were detected

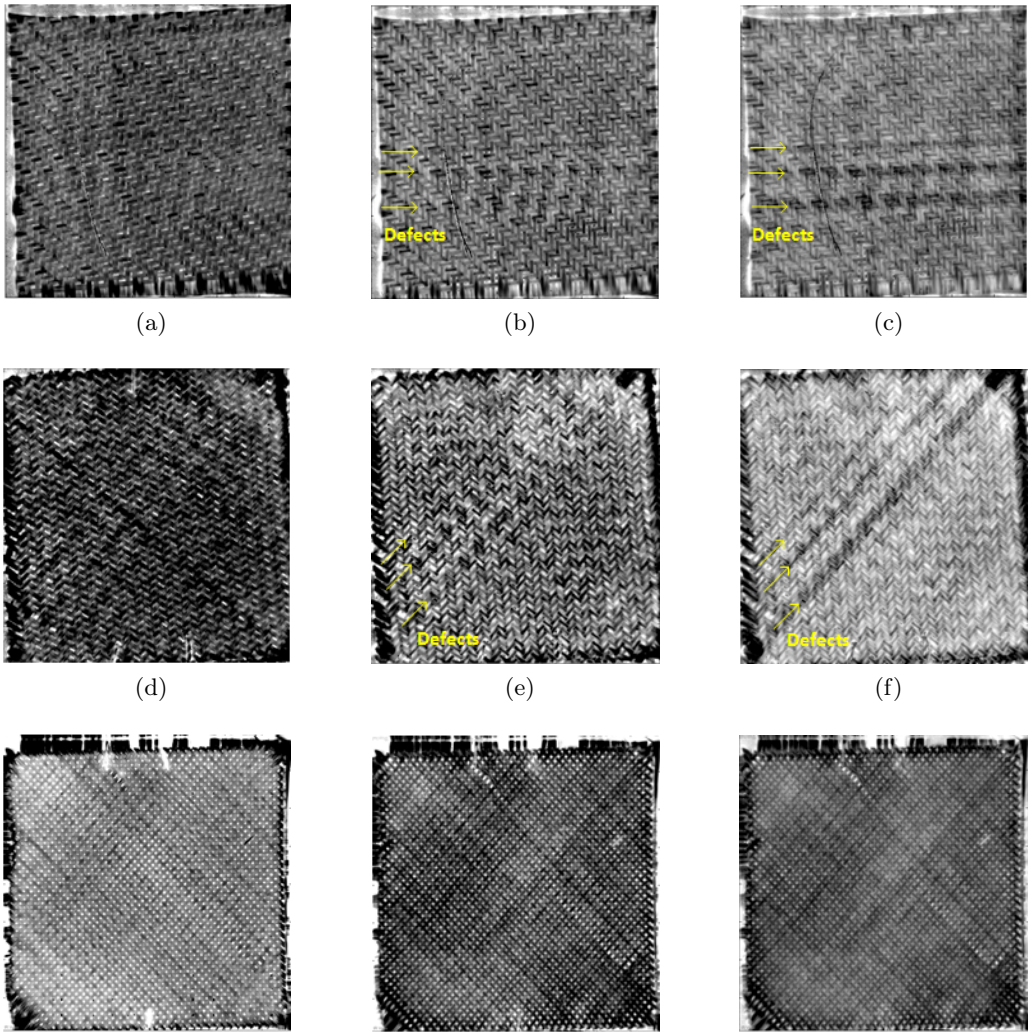

(a) (b) (c)

(d) (e) (f)

(g) (h) (i)

Figure 3.5: Phase transform results of TW/PW specimens using the flashes set-up and 88 fps: (a) TW-01: 0.25 mm, (b) TW-01: 0.4 mm, (c) TW-01: 0.5 mm, (d) TW-02: 0.25 mm, (e) TW-02: 0.4 mm, (f) TW-02: 0.5 mm, (g) PW-01: 0.25 mm, (h) PW-01: 0.4 mm, (i) PW-01: 0.5 mm.

in Figs. 3.8a - 3.8f, and they are increasingly clear as the depth increases. This observation concurs with the theoretical prediction because defects in the two-layered US specimens were fabricated from the middle depth approximately. Defects in the four-layered specimen US-03 (Figs. 3.8g, 3.8h and 3.8i) were not detected because they are located much deeper than 0.4 mm. Compared with TW/PW resutls, defects in US specimens can be detected at shallower depths due to the simpler structures of the preforms. However, detection at deeper depths is more difficult than with TW and PW specimens due to the lower thermal diffusivity value.

Figs. 3.9 and 3.10 show B-TSR, PLST and PCT results for US specimens obtained using the flashes set-up and 88 fps. Defects in the four-layered specimen US-03 were not detected due to

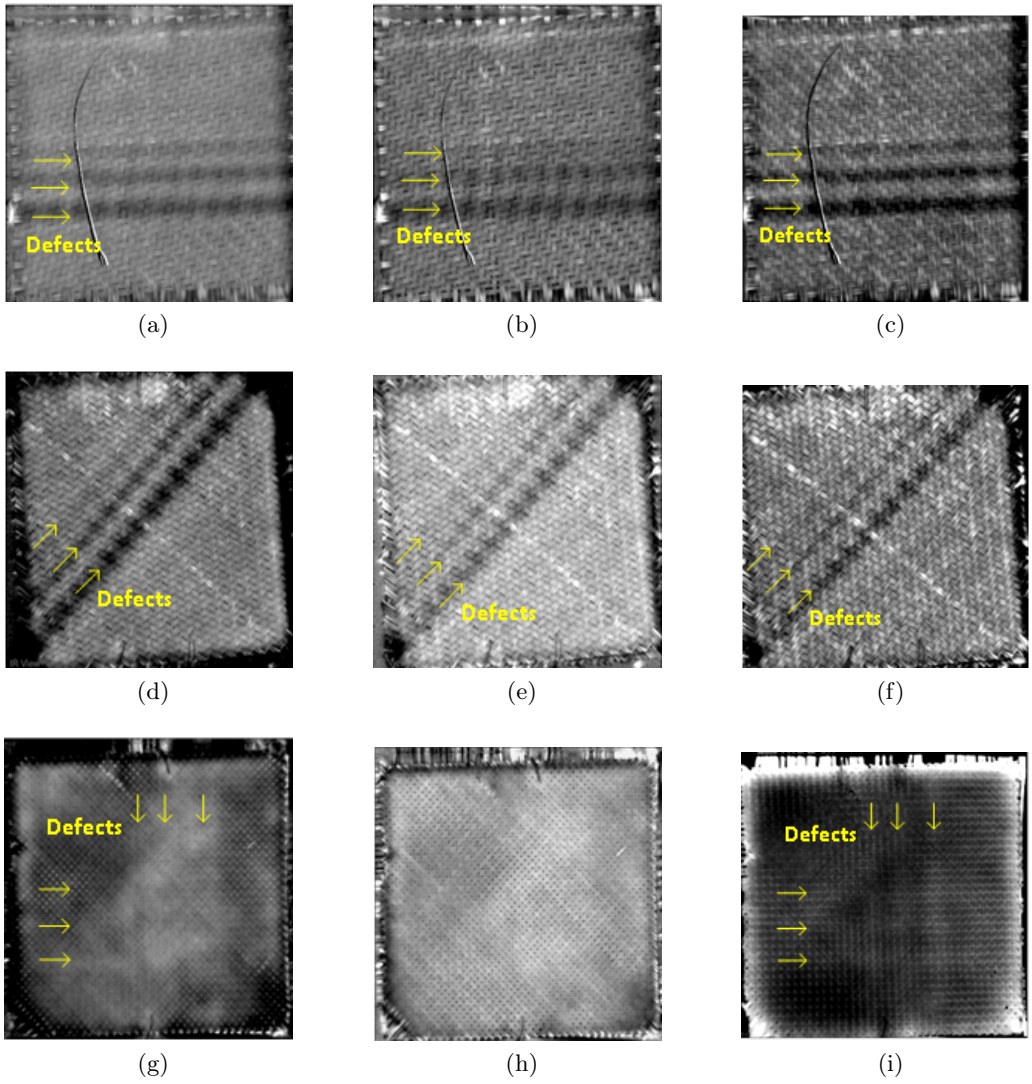

(a) (b) (c) (d) (e) (f) (g) (h) (i)

Figure 3.6: B-TSR and PCT results of TW/PW specimens using the flashes set-up and 88 fps: (a) TW-01: B-TSR (1st), (b) TW-01: B-TSR (2nd), (c) TW-01: PCT (EOF03), (d) TW-02: B-TSR (1st), (e) TW-02: B-TSR (2nd), (f) TW-02: PCT (EOF03), (g) PW-01: B-TSR (1st), (h) PW-01: B-TSR (2nd), (i) PW-01: PCT (EOF01).

the lower thermal diffusivity value. Similarly, PLST results are not as clear as those obtained with the other techniques. However, PLST requires less processing time and it can provide qualitative depth information.

Fig. 3.11 shows thermographic results for PW-01 and US-03 obtained with the flashes/halogen lamps set-ups and 55 fps. The cooling times were 10 and 15 s for the flashes/halogen lamps set-ups, respectively. For PW-01, the depths of 0.9 mm (0.2 Hz) and 1.65 mm (0.065 Hz) were investigated using the flashes/halogen lamps set-ups, respectively. For US-03, the depths of 0.5 mm (0.2 Hz) and 0.9 mm (0.065 Hz) were investigated correspondingly. Defects in PW-01

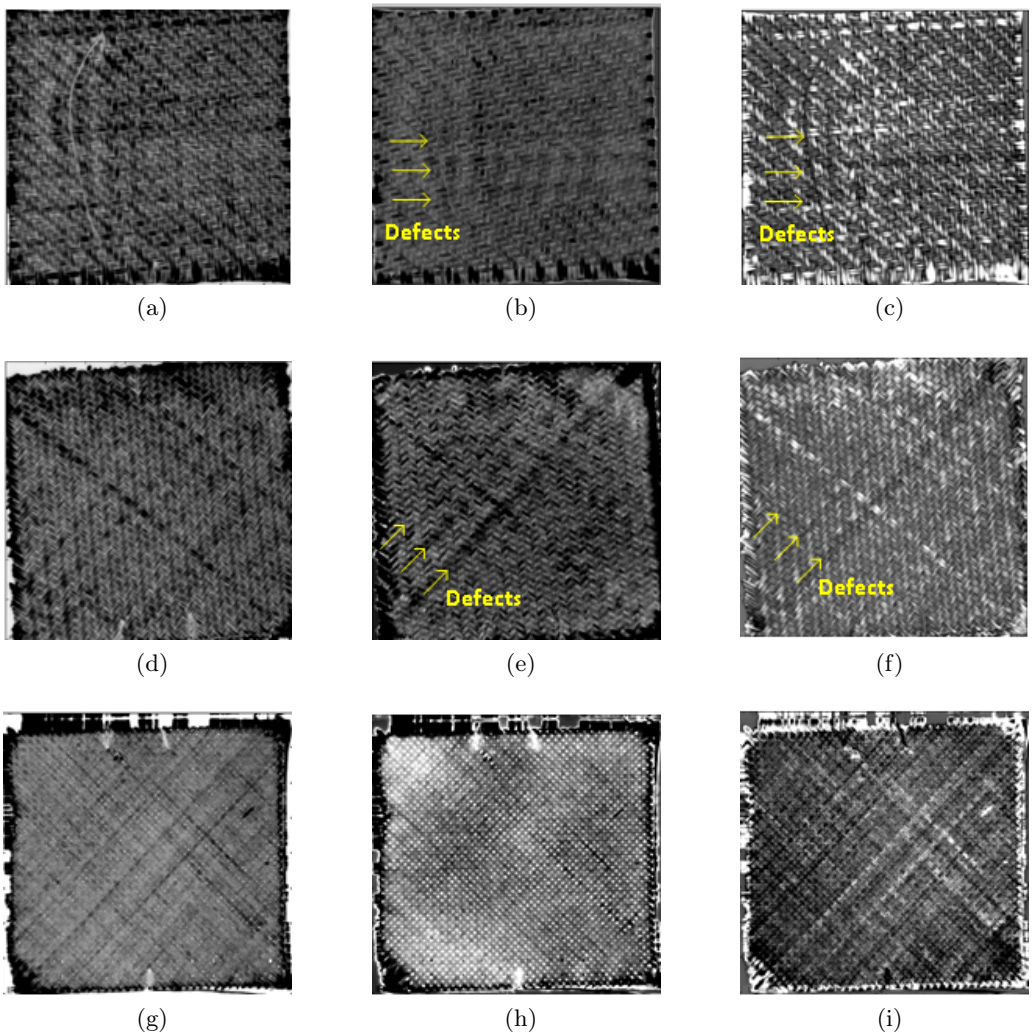

(a) (b) (c)

(d) (e) (f)

(g) (h) (i)

Figure 3.7: PLST results of TW/PW specimens using the flashes set-up and 88 fps: (a) TW-01: 1st loading, (b) TW-01: 2nd loading, (c) TW-01: 3rd loading, (d) TW-02: 1st loading, (e) TW-02: 2nd loading, (f) TW-02: 3rd loading, (g) PW-01: 1st loading, (h) PW-01: 2nd loading, (i) PW-01: 3rd loading.

were detected more clearly at a depth of 0.9 mm as shown in Fig. 3.11a, and they disappeared at a depth of 1.65 mm (Fig. 3.11b) because this is beyond the depths which can be successfully investigated in this specimen. Defects in US-03 were not detected at a depth of 0.5 mm (Fig. 3.11e), and a defect was detected at a depth of 0.9 mm (Fig. 3.11f), which coincides with the theoretical estimation. B-TSR and PCT show clearer results for both specimens. Detection in sample US-03 is more difficult than it is in the same-thickness PW-01, which may be due to its higher density as discussed in section 3.2. A possible solution is to increase the heat power by LT, which was also done in order to obtain additional information. The phase-based result at a depth of 0.8 mm (0.08 Hz and 3 periods) is shown in Fig. 3.12a, and the PCT result is shown in Fig. 3.12b. Indeed, phase-based LT shows clearer results and additional

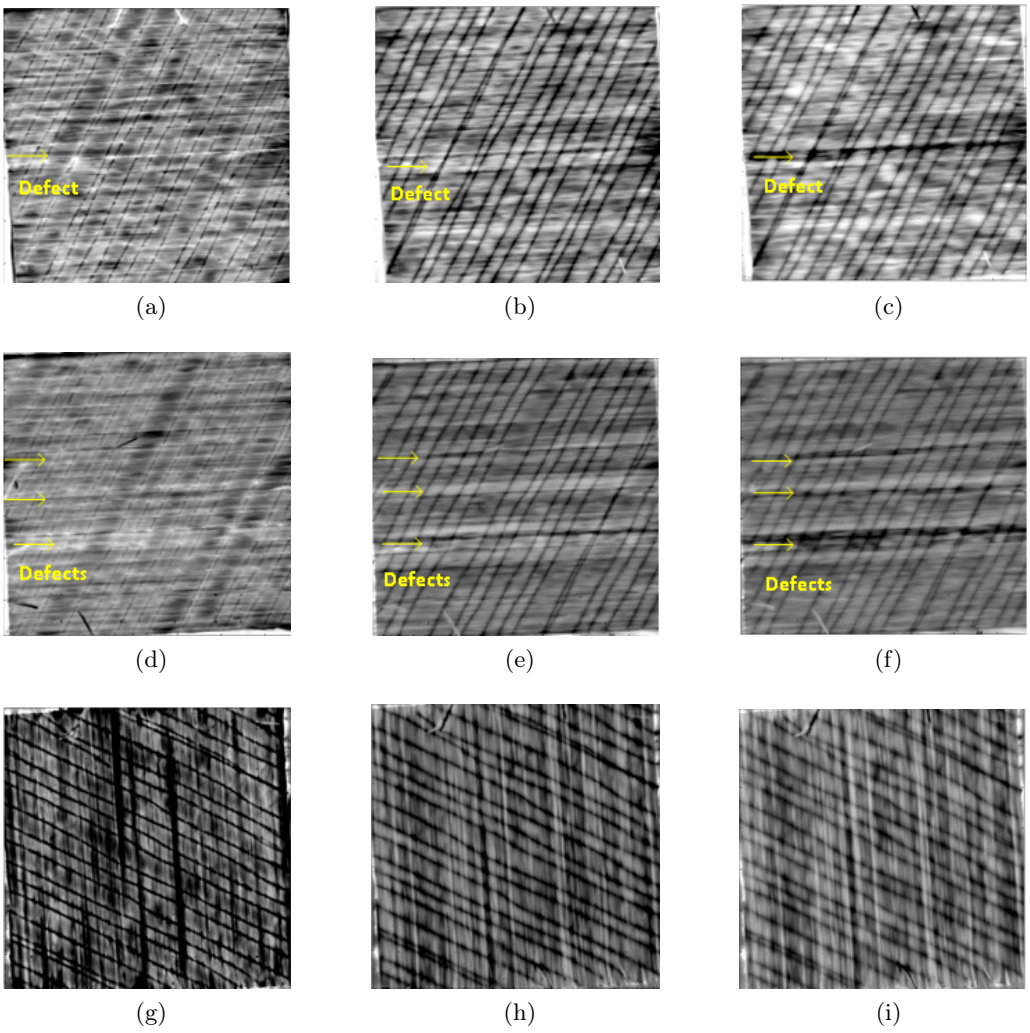

(a) (b) (c)

(d) (e) (f)

(g) (h) (i)

Figure 3.8: Phase transform results of US specimens using the flashes set-up and 88 fps: (a) US-01: 0.15 mm, (b) US-01: 0.3 mm, (c) US-01: 0.4 mm, (d) US-02: 0.15 mm, (e) US-02: 0.3 mm, (f) US-02: 0.4 mm, (g) US-03: 0.15 mm, (h) US-03: 0.3 mm, (i) US-03: 0.4 mm.

information compared with phase-based PT. However, the fabric was twisted (Fig. 3.12c and 3.12d) after 3 periods of heating because the thermoplastic stitch cannot sustain the higher thermal energy, which shows a great difference from composites. Therefore, PT is the more feasible solution for carbon fiber dry preforms inspection according to the previous analysis in this work.

3.6 Summary

Image diagnosis and characterization for carbon fiber dry preform was conducted and analyzed by optical excitation thermography in this chapter, which demonstrates feasible fast IRT-NDT modality for dry preforms inspection prior to resin infusion and manufacturing. The

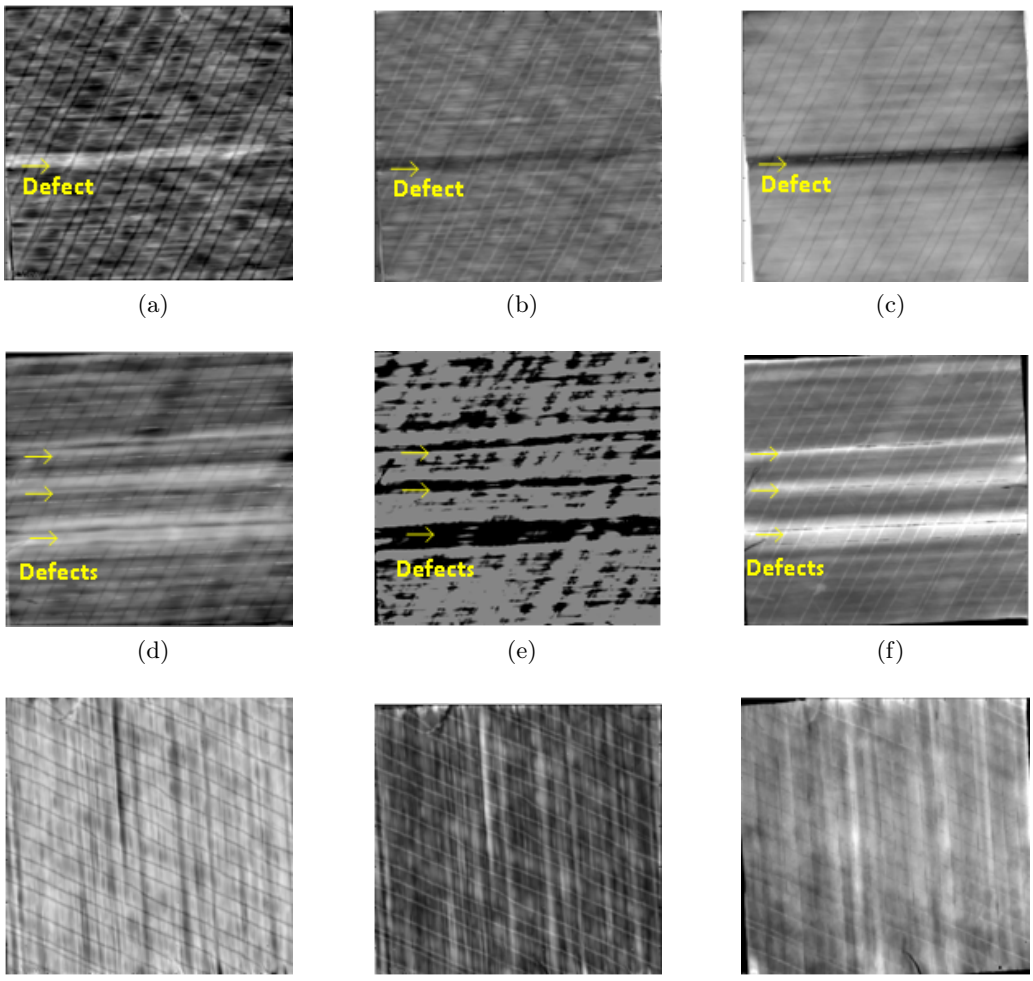

(a) (b) (c) (d) (e) (f) (g) (h) (i)

Figure 3.9: B-TSR and PCT results of US specimens using the flashes set-up and 88 fps: (a) US-01: B-TSR (1st), (b) US-01: B-TSR (2nd), (c) US-01: PCT (EOF01), (d) US-02: B-TSR (1st), (e) US-02: B-TSR (2nd), (f) US-02: PCT (EOF01), (g) US-03: B-TSR (1st), (h) US-03: B-TSR (2nd), (i) US-03: PCT (EOF01).

air and carbon fiber weight fraction difference leads to a discrepancy in thermal diffusivity, which is difficult to bring to light using theoretical calculation. Therefore, an experimental measurement of the thermal diffusivity prior to inspection is needed in the case of dry preforms. For higher density specimens, deeper detection is more difficult and requires more energy than for lower density specimens due to greatly different thermal diffusivities of the constituent materials.

Table. 3.4 shows the performance of different thermographic techniques for dry carbon fiber preform inspection (the comparison is based on the specimens used in this work). Overall, IRT can provide clear results by phase transform, B-TSR, PCT and PLST. Among these techniques, B-TSR and PCT show the clearest results. The lack of quantitative analysis is a

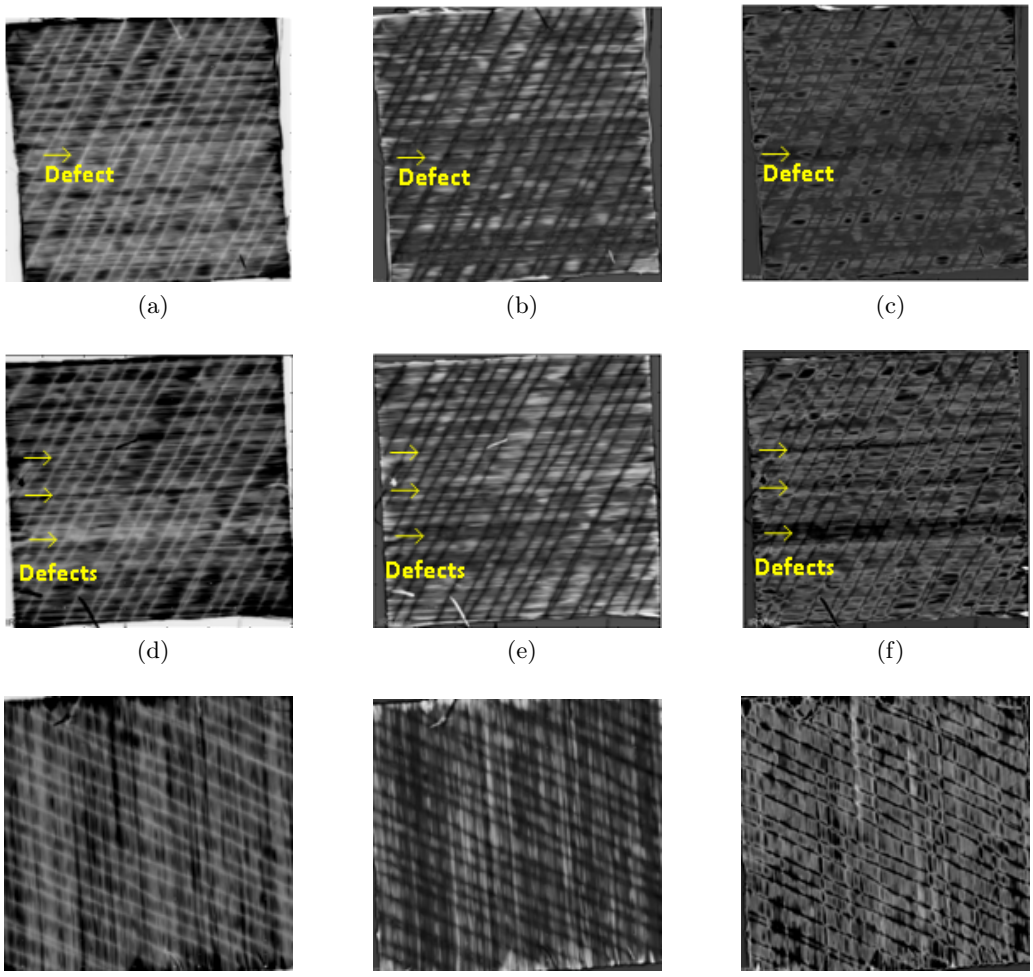

(a) (b) (c) (d) (e) (f) (g) (h) (i)

Figure 3.10: PLST results of US specimens using the flashes set-up and 88 fps: (a) US-01: 1st loading, (b) US-01: 3rd loading, (c) US-01: 5th loading, (d) US-02: 1st loading, (e) US-02: 3rd loading, (f) US-02: 5th loading, (g) US-03: 1st loading, (h) US-03: 3rd loading, (i) US-03: 5thUS loading.

Table 3.4: Performance of thermographic methods.

Defect identification ability		B-TSR ≈ PCT > phase transform ≈ PLST
Technical simplicity (less processing time)		B-TSR ≈ PCT ≈ PLST > phase transform
Quantitative analysis	Shallow-defect	PT (phase)^1 ≈ B-TSR
	Deep-defect	PT (phase)^2 ≈ B-TSR ≈ LT (phase)
Qualitative depth information	Shallow-defect	PT (phase)^1 ≈ B-TSR ≈ PLST
	Deep-defect	PT (phase)^2 ≈ B-TSR ≈ PLST ≈ LT (phase)

PT (phase)^1: flashes modality; PT (phase)^2: halogen lamps modality;

disadvantage of PCT [73]. Phase transform can provide quantitative analysis and additional information, which is often important for a NDT technique. PLST can also show additional results as the depth increases, but not as clearly as phase transform. PLST can only provide qualitative depth information, but it needs less processing time than phase transform. The

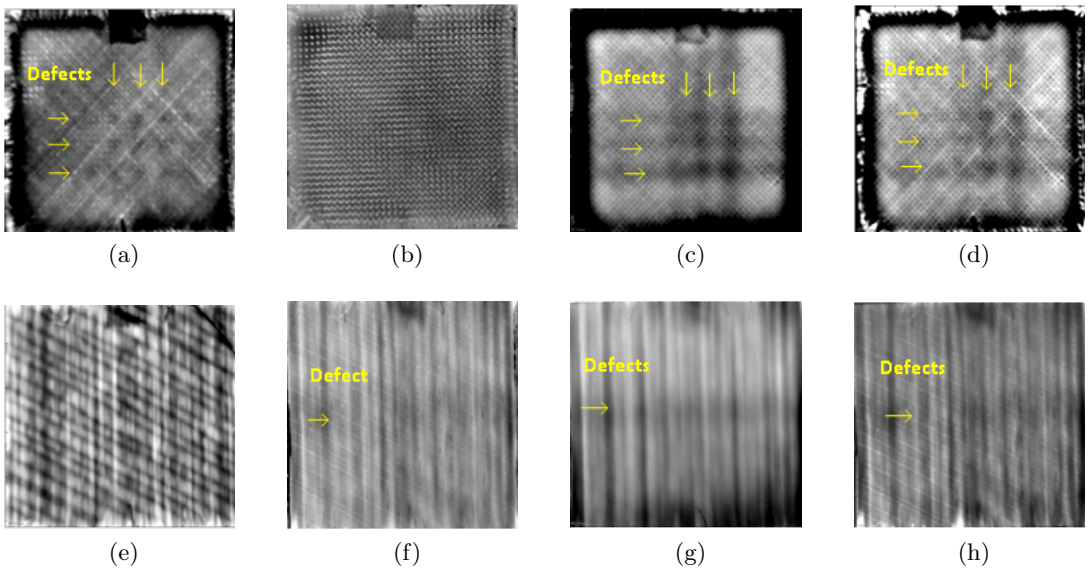

(a) (b) (c) (d)

(e) (f) (g) (h)

Figure 3.11: Thermographic results of PW-01 and US-03 using the flash/halogen lamps set-ups and 55 fps: (a) PW-03: 0.9 mm, (b) PW-01: 1.65 mm, (c) PW-01: B-TSR (1st), (d) PW-01: PCT (EOF03), (e) US-03: 0.5 mm, (f) US-03: 0.9 mm, (g) US-03: B-TSR (1st), (h) US-03: PCT (EOF03).

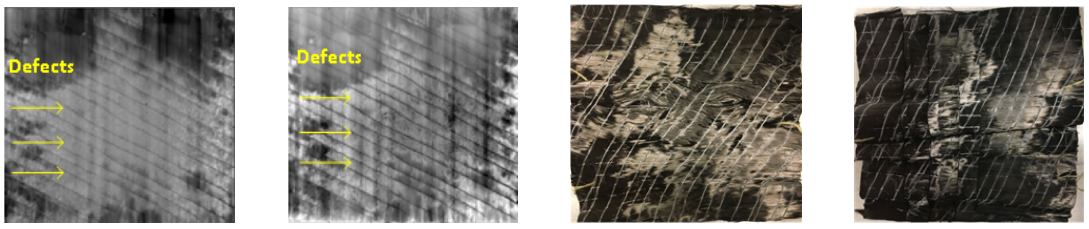

(a) (b) (c) (d)

Figure 3.12: (a) US-03: Phase-based LT (0.8 mm), (b) US-03: PCT (EOF04), (c) US-03: twisted front photo, (d) US-03: twisted rear photo.

flashes modality can detect shallow-defects because it can reach higher frequency. On the contrary, the halogen lamps modality is better for deep-defects detection.

Differently from composites, dry preforms featuring thermoplastic stitches cannot sustain high energy heating so that LT is inappropriate in such a case. Although this may limit the maximum detection depth, IRT is a more feasible technique for dry preforms inspection compared with CT, which are much more expensive and time-consuming [60; 74]. Of interest, B-TSR and PCT are more appropriate for fast detection. Therefore, the development of an automatic system for identifying defects in dry preforms based on infrared computer vision could be built for industrial applications [75; 76].

Chapter 4

Image Diagnosis and Characterization for Natural Fiber Composites

4.1 Introduction

Natural fibers, including vegetable and mineral fibers, are increasingly used for composites due to their low environmental impact. Among mineral materials, basalt is attracting increasing attention thanks to its advantages in terms of mechanical properties, sound insulation properties, low water absorption, good resistance to chemical attack, high operating temperature range, low environmental impact and lack of carcinogens and health hazards. Basalt, which is usually found in volcanic rocks originating from frozen lava with a melting temperature between 1500°C and 1700°C, was mainly used as reinforcement of both thermoset and thermoplastic polymers in the last decade. The investigations of vegetable fibers in the open literature show acceptable mechanical properties and low cost, but moisture sensitivity and low adhesion to hydrophobic polymer matrices [77]. Among them, jute, hemp and bagasse fibers are attracting increasing attention.

Low-velocity impact is usually considered as a major threat to fiber reinforced polymer composites. Such foreign object loading may occur during the process of manufacturing, assembly, maintenance, and operation. The impact damage can greatly affect the residual mechanical properties of composites even if the damage is barely visible (e.g., delamination and back-face splitting can reduce the residual strength by as much as 60%) [77]. The post-impact damage is becoming increasingly important for the behavior of natural fiber composites, as they are usually reported to exhibit a limited resistance to impact loading.

In this work, optical and mechanical excitation thermography is used to evaluate impacted basalt fiber reinforced polymer laminates (BFRP), jute-hemp fiber hybrid laminates (JHFP), and homogeneous particleboards of sugarcane bagasse (SCB). Of particular interest, SCB is a type of more recent vegetable fiber composite whose NDT is new in the field. Phase transform

was performed for quantitative analysis in optical excitation thermography, in which the time domain to frequency domain transform was carried out to obtain depth information. Phase-based thermography for natural fiber composites is poorly documented in the open literature. Advanced image processing techniques, including CIS and PCT, were also used to process the data. In addition, UT and CW THz imaging were used on the mineral fiber laminates. Finally, a comprehensive comparison of different techniques for natural fibers composites detection was conducted.

4.2 Natural Fiber Composites

4.2.1 Basalt Fiber Reinforced Polymer Laminates (BFRP)

The laminates were manufactured by resin transfer molding with a fiber volume fraction of 0.38 ± 0.02 and a thickness of 3 ± 0.1 mm. The plain weave basalt fabric (BAS 220.1270.P) with a surface weight of 220 g/m^2 and a vinylester resin (DION 9102) were used for the matrix. A hemispherical impactor with a 12.7 mm diameter tip was used and the samples were clamped to a square frame with a 73 mm square window [77]. Three impact energies (equal to 7.5, 15 and 22.5 J shown in Fig. 4.1) were used in this study.

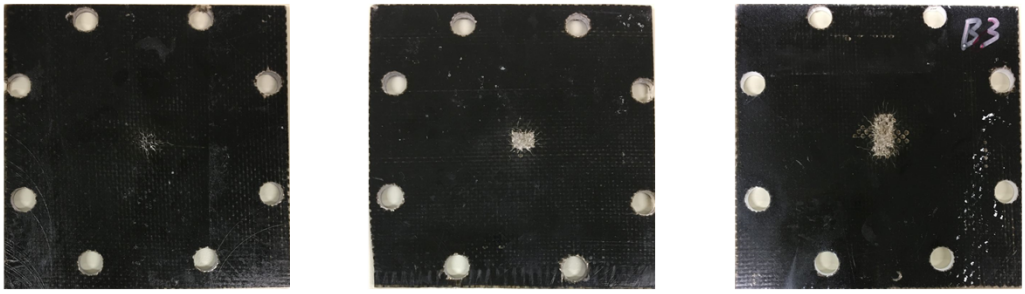

(a) (b) (c)

Figure 4.1: BFRP specimens (rear side): (a) 7.5 J, (b) 15 J, (c) 22.5 J.

4.2.2 Jute-Hemp Fiber Hybrid Laminates (JHFP)

The laminates were manufactured using hemp fibers decorticated and bleached using sodium chlorite in optimized conditions and jute hessian cloth (plain weave) of areal weight 250 g/m^2 (impregnated with I-SX10 LEGNO epoxy resin and SX10 LEGNO 33%). The layup of the laminates includes six inner layers of jute plain weave placed at 0°/0°/45°/-45°/0°/0°, sandwiched between two nonwoven hemp mats. The composites include 30 (±2) wt.% of jute fiber and 20 (±1.5) wt.% of hemp fiber. The laminates were produced using a hand lay-up procedure in a closed matching mold of dimensions 220 × 250 × 3.7 (±0.2) mm^2 by applying a slight pressure of ca. 0.02 MPa. The dimensions of the samples are 140 × 220 × 2.8 (±0.1)

mm. A hemispherical nose of 12.7 mm diameter was used to impact three laminates (Fig. 4.2) [78].

(a) (b) (c)

Figure 4.2: Jute/hemp fiber hybrid laminates (rear side): (a) plate No. 1, (b) plate No. 2, (c) plate No. 3.

4.2.3 Homogeneous Particleboards of Sugarcane Bagasse (SCB)

The high-density homogeneous particleboards of SCB and polyurethane resin based on castor oil followed the methodology defined in [79], assuming a nominal density of 800 kg/m^3 and dimensions of 0.55 × 0.55 × 0.016 m. Initially, the SCB was oven dried at a temperature of 60°C for 24 hours to reduce the moisture content to around 12%. After drying, it was sieved in a sieve shaker. The bagasse particles retained in the sieve mesh with openings greater than 2 mm were milled in a knife mill to produce particles of size up to 8 mm. The particles with a size of less than 2 mm were removed from the manufacturing process because they are not suitable for the step of dispersing the resin. Subsequently, the particles of SCB were introduced in a planetary mixer and the adhesive polyurethane resin based on castor oil was added, in a proportion of 15% by weight of the dry mass of bagasse, for better uniformity in the distribution of the adhesive in particles. After this mixing period, the particles were introduced into a mattress forming mold, with dimensions of 0.55 × 0.55 m and pressed with a pressure of 5 MPa at a temperature of 100 °C, for a period of 10 min. At the end of the pressing process, the complete curing process of the resin required a period of 72 hours [80].

(a) (b) (c) (d)

Figure 4.3: SCB specimens (front side): (a) 5 J, (b) 10 J, (c) 20 J, (d) 30 J.

Low velocity impact tests at four different energy levels, namely 5, 10, 20 and 30J (Fig. 4.3) were carried out using an instrumented drop-weight impact testing machine (CEAST/Instron 9340). During all impact tests, a steel mass was attached to the steel impactor with a hemispherical cup of 20 mm diameter for a total weight of 3 kg. The different energy levels were obtained by changing the height of release of the impactor. The specimens were clamped circumferentially along a diameter of 40 mm in a pneumatic-actuated clamping fixture. During the test, the time histories of impact force and the initial impact velocity were recorded. Post-impact, the permanent dent depth of each coupon was measured using a non-contact profilometer (Taylor-Hobson Talyscan 150) with a scanning speed of 10500 μm/s. The dent depth as a function of impact energy is shown in Table 4.1 [80].

Table 4.1: Dent depth as a function of impact energy.

Impact energy [J]	5	10	20	30
Dent depth [μm]	592	1128	1469	1545

4.3 Experimental Configurations

4.3.1 Optical Excitation Thermography

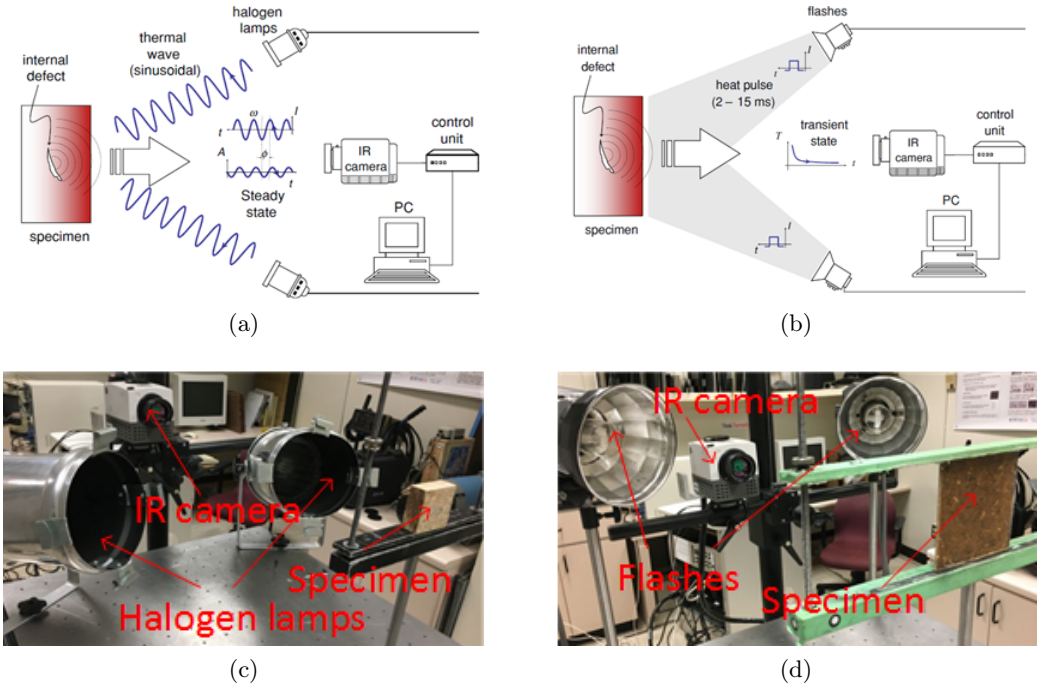

(a) (b)

(c) (d)

Figure 4.4: Optical excitation thermography set-ups: (a) schematic set-up for LT [4], (b) schematic set-up for PT (flashes) [4], (c) experimental set-up for LT/PT (halogen lamps), (d) experimental set-up for PT (flashes).

Figs. 4.4a and 4.4c show the schematic and experimental set-up for LT. Two 'OMNLUX PAR64' (1000 W) halogen lamps were used to generate lock-in sinusoidal signals. A mid-wave IR camera 'FLIR Phoenix' (Table 4.2) was used to record the temperature profile.

Table 4.2: Flir Phoenix (MWIR) technical specifications [1].

Technical specification	Explanation/value
Detector type	Indium Antimonide (InSb)
Cold filte bandpass	3.0 - 5.0 μm standard
Pixel resolution	640 (H) $\times$ 512 (V) pixels
Spec performance	$<$ 25 milliKelvin

Fig. 4.4b shows the schematic set-up for photographic flash modality. For high-energy lamp modality, the pulse excitation signal is the only difference shown in Fig. 4.4a. Figs. 4.4c and 4.4d show the experimental set-ups. Two 'OMNLUX PAR64' (1000 W, 5 s duration) halogen lamps/Balcar FX 60 (6.4 KJ each, 5 ms duration) producing photographic flashes were used. The same mid-wave IR camera with the frame rate of ~55 fps was used. The cooling time is 15 s/20 s for flashes/halogen lamps modality, respectively.

4.3.2 VT

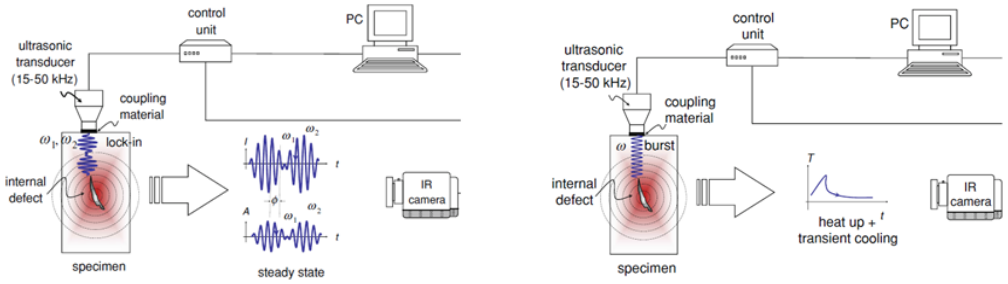

(a) (b)

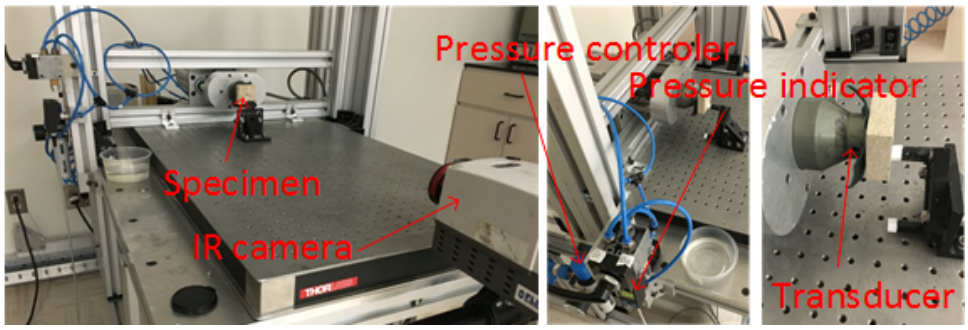

(c)

Figure 4.5: VT set-up, (a) schematic set-up using lock-in signals [4], schematic set-up using pulse signals [4], (c) experimental set-up.

Fig. 4.5 shows the VT set-up. The same IR camera with the frame rate of ∼55 fps was used. The transducer was pressed (200 Pa) against the specimen and two periods of 0.2 Hz (10 s) lock-in ultrasonic waves were delivered.

4.3.3 UT

In this work, UT experiments were conducted in reflection mode; water was used as the wedge and the back wall signals were used for imaging. The UT experimental set-up in Fig. 4.6 consists of a ′Olympus OmniScan MX′, a probe ′Olympus PANAMETRICS-NDT A310S 5 MHz/0.25″ ′, a robotic x-y glider scanner ′IAI Robo Cylinder RCP2′ for raster scanning, and a water tank. The distance between the probe and the specimen is ∼10 mm, and the system resolution is 0.2 mm.

Figure 4.6: UT experimental set-up.

4.3.4 CW THz

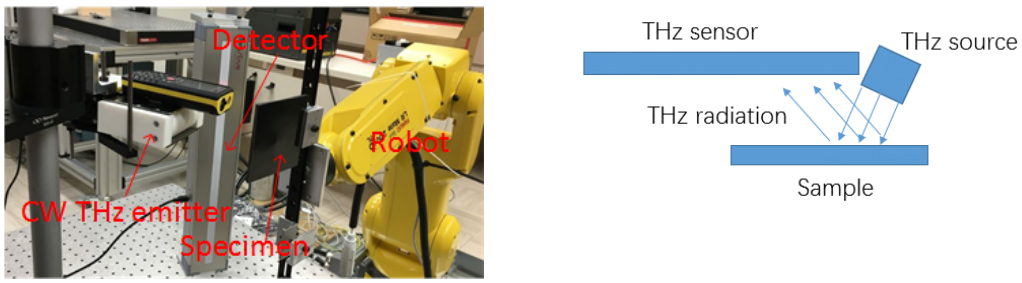

(a) (b)

Figure 4.7: CW sub-THz imaging system in reflection mode: (a) experimental set-up, (b) schematic set-up.

The CW THz system (Fig. 4.7) uses IMPAct ionization Transit Time (IMPATT) diodes to exploit ∼0.1 THz CW imaging, and the system resolution is ∼3 mm. It consists of a detector ′TeraSense Linear-1024′, a CW emitter ′TeraSense TS 1603′, and a robot ′Funac LR Mate

200iD 7L′ to perform a line scanning. The detector has a spectral range of 40 GHz - 0.7 THz and a frame rate of ∼8.2 fps. The pixel size of the detector is 1.5 mm × 1.5 mm, and the number of pixels is 1024 (256 × 4). The emitter has an optimized frequency of ∼0.1 THz and 1 μs rise/fall time (TTL Modulation). The detector records 256 × 4 pixels (384 mm × 6 mm) into one frame. The distance from the specimen to the CW emitter/detector was ∼10 cm.

4.4 Experimental Results and Analysis

According to Eq. 2.4, the thermal diffusivity α is a parameter of particular importance for calculating the depth by phase transform. α can be expressed as follows according to Eq. 1.1:

$$\alpha = \frac{k}{\rho c_p} \tag{4.1}$$

where $c_p[J/KgK]$ is the specific heat at constant pressure, $\rho[Kg/m^3]$ is the density, and $k[W/mK]$ is the thermal conductivity.

For composite materials, α can be calculated by:

$$\alpha_{composite} = \sum_{1}^{N} (weightfractionmaterial \cdot \alpha_{material})_N \tag{4.2}$$

where N is the number of constituent materials in the composites.

In this work, the thermal diffusivity α was obtained by calculating c_p, ρ and k in Table 4.3.

Table 4.3: Physical properties of materials.

	Basalt fiber (63%)	Vinyl ester resin (37%)	BFRP
k $[W/mK]$	0.031	0.229	0.104
ρ $[Kg/m^3]$	2630	1220	2108.3
C_p $[J/KgK]$	860	1000	1083.8
	Jute (30%) / hemp (20%) fibers	Epoxy resin I-SX10 (50%)	JHFP
k $[W/mK]$	0.365 / 0.04	0.229	0.232
ρ $[Kg/m^3]$	1460 / 25	1100	993
C_p $[J/KgK]$	1360 / 1800	1000	1268
	Bagasse fiber (60%)	Polyurethane resin (40%)	SCB
k $[W/mK]$	0.475	0.209	0.369
ρ $[Kg/m^3]$	520	1200	792
C_p $[J/KgK]$	3601.8	1400	2720.6

Fig. 4.8 shows the PT results of BFRP. Phase transform was performed by Eqs. 2.1 and 2.3 as discussed previously, and then the depth information was obtained by Eqs. 2.4 and 4.1 using the physical properties in Table 4.3. The images from the depths of 0.28 mm (0.6 Hz), 0.85 mm (o.065 Hz) and 1 mm (0.048 Hz) were obtained in flashes and halogen lamps modalities, respectively.

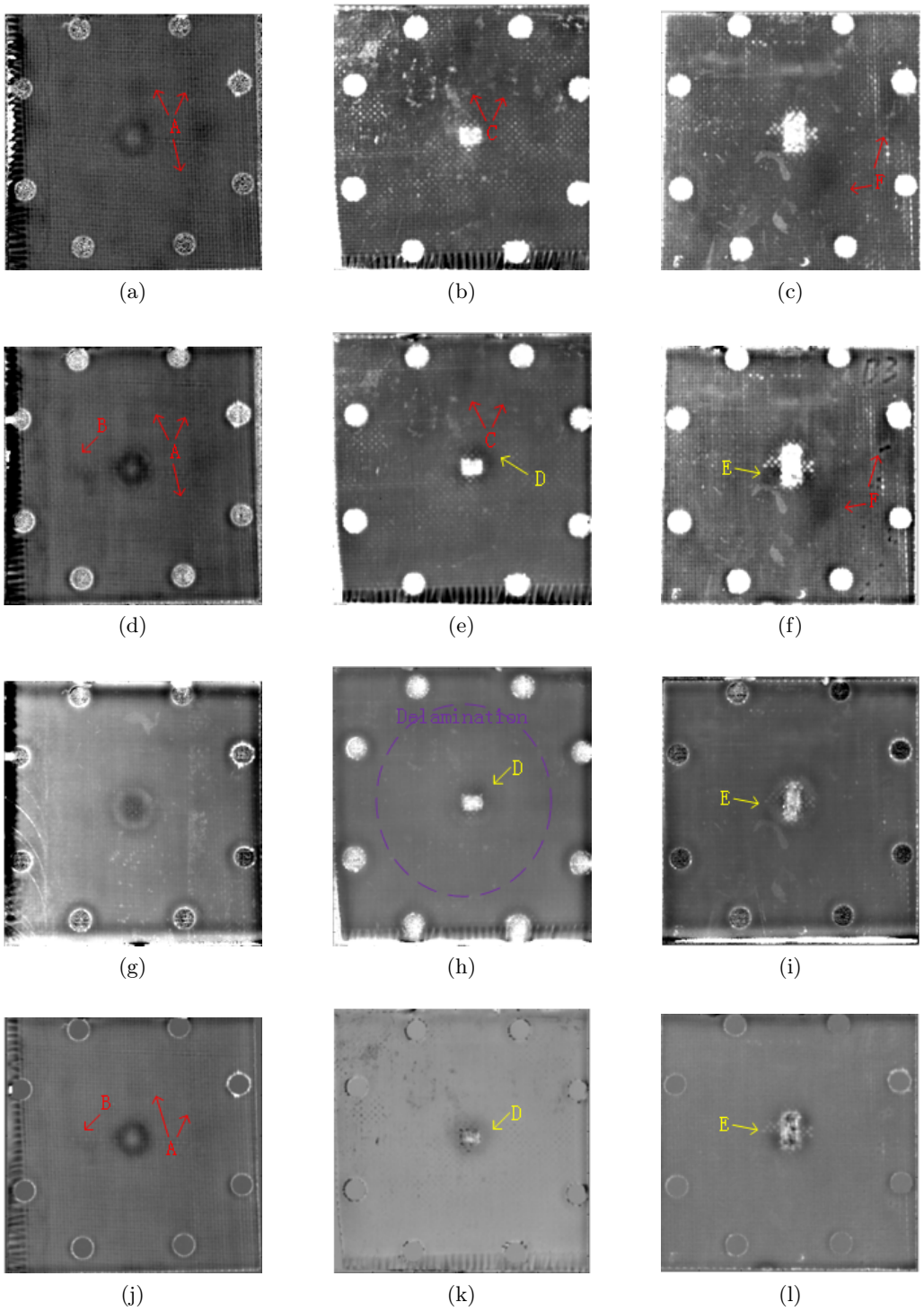

(a) (b) (c)

(d) (e) (f)

(g) (h) (i)

(j) (k) (l)

Figure 4.8: PT results of BFRP: (a) 7.5 J: 0.28 mm, (b) 15 J: 0.28 mm, (c) 22.5 J: 0.28 mm, (d) 7.5 J: 0.85 mm, (e) 15 J: 0.85 mm, (f) 22.5 J: 0.85 mm, (g) 7.5 J: 1 mm, (h) 15 J: 1 mm, (i) 22.5 J 1 mm, (j) 7.5 J: PCT (EOF03), (k) 15 J: PCT (EOF04), (l) 22.5 J: PCT (EOF03).

In Figs. 4.8a and 4.8b, the resin-rich areas A and C were detected at the depth of 0.28 mm, and were barely detected at the depths of 0.85 mm (Figs. 4.8d and 4.8e), then were not detected at all at the depth of 1 mm (Figs. 4.8g and 4.8h). The resin-rich areas B and F were detected at the depth of 0.85 mm (Figs. 4.8d and 4.8f) in the clearest view; they were not detected at the depth of 1 mm (Figs. 4.8g and 4.8i). The delamination in Fig. 4.8h (marked in purple) was detected at the depth of 1 mm, which suggests its depth. The impact damage (marked in yellow) grew along with the depth increase. Overall, flashes modality provided clearer results than halogen lamps modality, and phase transform can provide the additional information. In particular, it can provide the depth information via frequencies for quantitative analysis, which is advantageous.

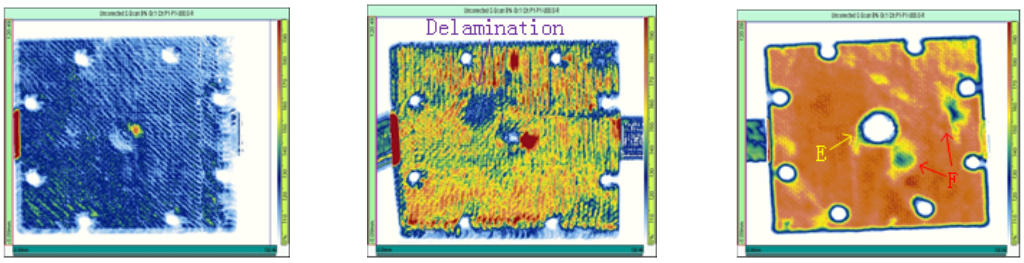

(a) (b) (c)

Figure 4.9: UT results of BFRP: (a) 7.5 J, (b) 15 J, (c) 22.5 J.

Taking into account the UT results in Fig. 4.9, the PT results evidently provided more information, especially for resin-rich areas (marked in red). The VT results in Fig. 4.10 only showed clear identification for delamination, but not for resin-rich and impact damage areas. The delamination was shown more clearly in the front-side inspection in Fig. 4.11.

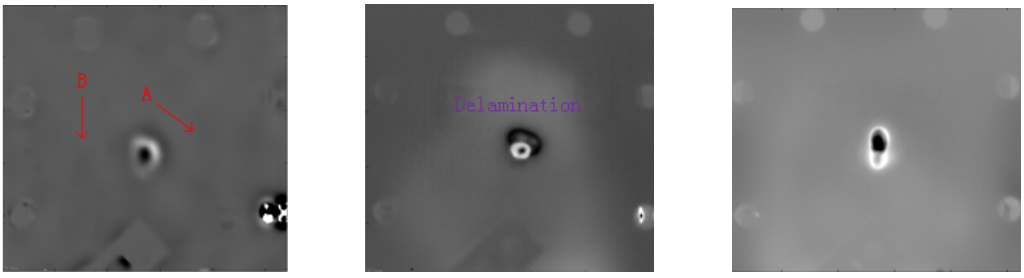

(a) (b) (c)

Figure 4.10: VT results BFRP: (a) 7.5 J: PCT (EOF06), (b) 15 J: PCT (EOF03), (c) 22.5 J: PCT (EOF02).

PPT provided additional information (Fig. 4.11e, 4.11f and 4.11g), in which the delamination shrinked along with the depth increase. CW sub-THz can detect the delamination, but showed a rough result (Fig. 4.11c). This may be caused by the low resolution (∼3 mm) linked to its low radiation frequency (∼0.1 THz). The depth information in CW inspection is inaccessible.

The intensity curve of the CW sub-THz result in Fig. 4.11d showed the delamination feature, which is deepest in the central zone. The fiber information was not detected in BFRP.

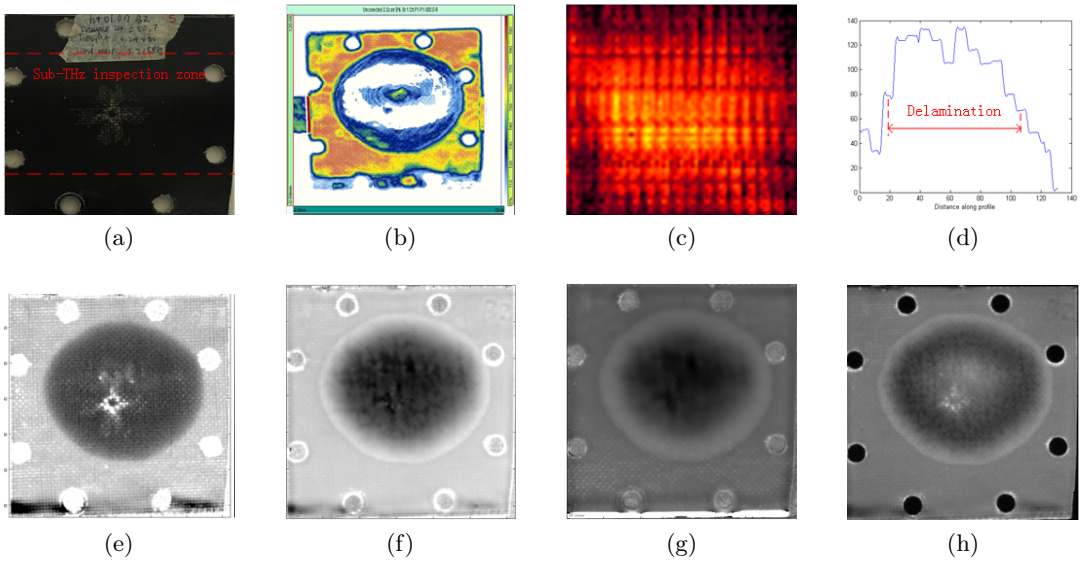

Figure 4.11: Front-side results of 15 J BFRP: (a) photo, (b) UT result, (c) CW sub-THz result, (d) intensity curve for sub-THz result, (e) phase: 0.28 mm, (f) phase: 0.85 mm, (g) phase: 1 mm, (h) PCT: EOF03.

Fig. 4.12 shows the thermographic results of JHFP. The results are linked to the flashes modality because it provides clearer results, and the full thickness can be detected due to the higher thermal diffusivity α. The images from the depths of 0.44 mm (1 Hz) and 1.72 mm (0.066 Hz) were obtained by phase transform. Impact damage areas (marked in yellow) other than the visible zones were detected, but not as clear as that in BFRP. The resin-rich areas (marked in red) were clearly detected. The fibers can be identified very clearly, which provides the possibility for the evaluation of fiber orientation. PPT (Fig. 4.12a - 4.12f) provided more information than PCT (Fig. 4.12g - 4.12i) and VT (Fig. 4.12j - 4.12l), especially for the identification of the flaws by means of defect depth retrieval via frequencies. PCT showed the clear identification for both resin-rich and impact damage areas, but the impossibility to perform a quantitative analysis is the disadvantage. VT only showed the impact damage areas, although additional information of resin-rich areas and fibers can be visualized.

Fig. 4.13 shows the thermographic results of SCB. The images from the depths of 1.65 mm (0.066 Hz) and 1.94 mm (0.048 Hz) were obtained. The resin-rich areas were detected, and the fibers can be identified. The fiber orientation evaluation is more difficult in the case of SCB due to the thermal characteristics. The impact damage areas A and B in Figs. 4.13a, 4.13b, 4.13e and 4.13f were not detected at the depths of 1.65 mm and 1.94 mm because they are too close to the surface. The impact damage area C was detected at the depth of 1.65 mm in Fig. 4.13c, and the impact damage area D was detected at depths of both 1.65 mm

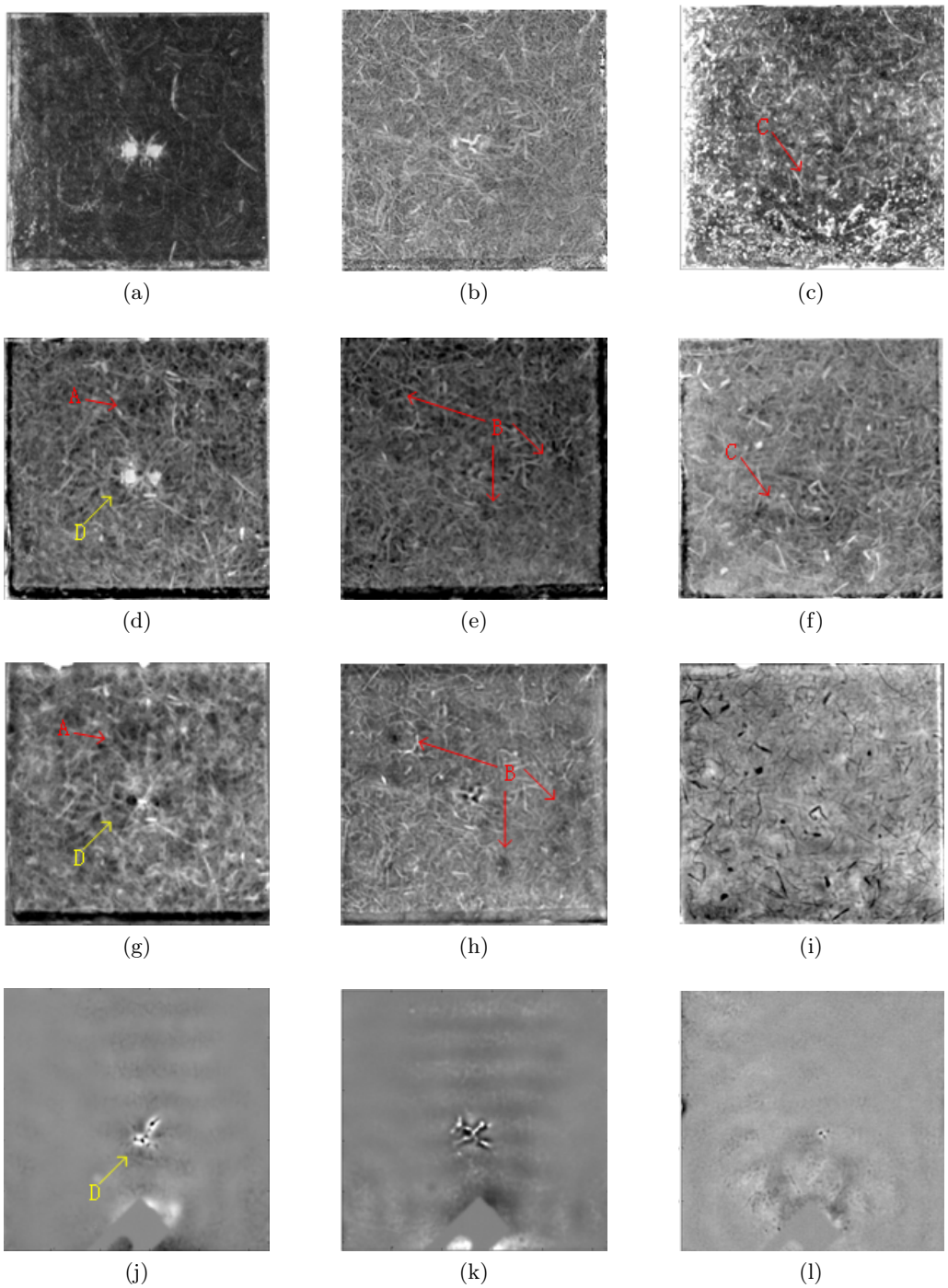

Figure 4.12: IRT results of JHFP: (a) plate No.1: 0.44 mm, (b) plate No.2: 0.44 mm, (c) plate No.3: 0.44 mm, (d) plate No.1: 1.72 mm, (e) plate No.2: 1.72 mm, (f) plate No.3: 1.72 mm, (g) plate No.1: PT (PCT: EOF02), (h) plate No.2: PT (PCT: EOF03), (i) plate No.3: PT (PCT: EOF03), (j) plate No.1: VT (PCT: EOF04), (k) plate No.2: VT (PCT: EOF04), (l) plate No.3: VT (PCT: EOF06).

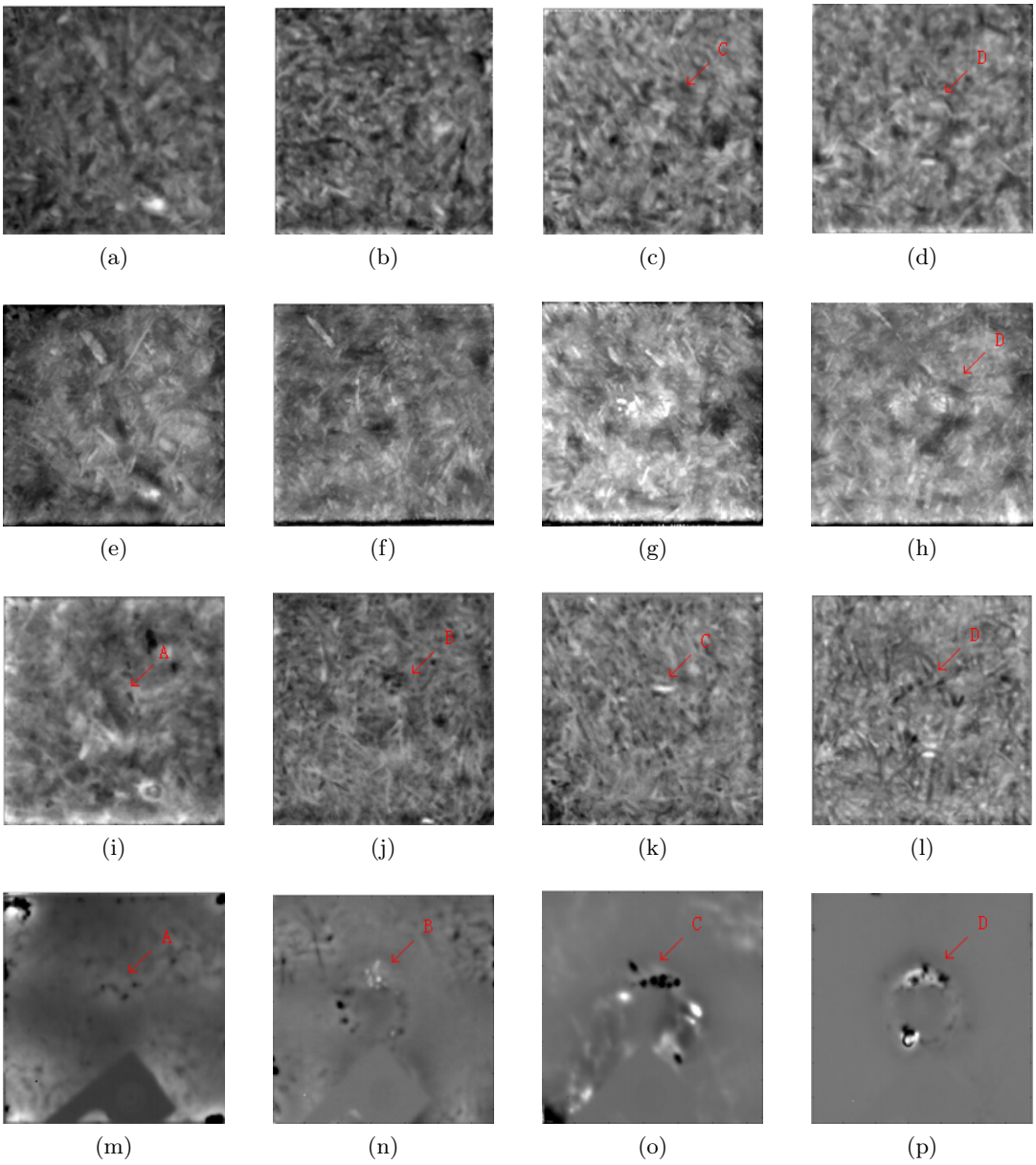

(a) (b) (c) (d)

(e) (f) (g) (h)

(i) (j) (k) (l)

(m) (n) (o) (p)

Figure 4.13: IRT results of SCB: (a) 5 J: 1.65 mm, (b) 10 J: 1.65 mm, (c) 20 J: 1.65 mm, (d) 30 J: 1.65 mm, (e) 5 J: 1.94 mm, (f) 10 J: 1.94 mm, (g) 20 J: 1.94 mm, (h) 30 J: 1.94 mm, (i) 5 J: PT (PCT: EOF), (j) 10 J: PT (PCT: EOF), (k) 20 J: PT (PCT: EOF), (l) 30 J: PT (PCT: EOF), (m) 5 J: VT (PCT: EOF), (n) 10 J: VT (PCT: EOF), (o) 20 J: VT (PCT: EOF), (p) 30 J: VT (PCT: EOF).

and 1.94 mm in Figs. 4.13d and 4.13h. The depth information is a little bit deeper than the mechanical measurement because the thermal diffusivity α value was calculated using similar and reasonable data present in the scientific literature. Nevertheless, the growing trend of the impact damage areas coincides with the theoretical estimation. The impact damage areas in the four specimens can be detected by PCT. Of interest, VT showed the clearest results for

the impact damage inspection of SCB.

Table 4.4: Relationship between modulated frequency f_b and depth z.

Frequency f_b [Hz]		0.2	0.1	0.08	0.05	0.02	0.01
Depth z [mm]	BFRP	0.49	0.69	0.77	0.98	1.55	2.19
	JHFP	0.99	1.39	1.56	1.97	3.12	4.41
	SCB	0.95	1.34	1.50	1.90	3.00	4.25

Table 4.4 shows the relationship between modulated frequency f_b and depth z according to Eq. 2.4 for phase-based LT. Fig. 4.14 shows the LT (phase) results of SCB at depths of 0.95 mm, 1.9 mm and 4.25 mm. The impact damage area A was not detected at the depths of 0.95 mm and 1.9 mm in Figs. 4.14a and 4.14e because it is located so close to the surface. The impact damage area B was detected at the depth of 0.95 mm in Fig. 4.14b, but not at the depth of 1.9 mm in Fig. 4.14f, which coincides with the mechanical measurement. The impact damage areas C and D were detected at the depths of 0.95 mm (Figs. 4.14c and 4.14d) and 1.9 mm (Figs. 4.14g and 4.14h) which is due to the calculation of the thermal diffusivity α from literature data. All the impact damage areas were not detected at the depth of 4.25 mm. The growing trend of impact damage in SCB coincides with the theoretical estimation. The resin-rich areas were also detected by phase-based LT, which showed clearer results, but the longer inspection time is the disadvantage.

4.5 Summary

Table 4.5 shows the capabilities of NDT techniques for natural fibers composites. Overall, IRT shows clearer results than UT and CW THz. Phase-based PT and LT can provide depth information and clearer results for more features than PCT and VT. VT can only show clearer results for the delamination in BFRP and the impact damage detection in SCB. The flashes modality can provide clearer results than halogen lamps modality, but the latter can detect deep-defects. On the contrary, quantitative analysis for shallow-defects is available in the flashes modality because a higher frequency could be reached. The fiber identification is difficult for BFRP, but feasible for JHFP and SCB - the more recent eco-friendly composite. In addition, the delamination was not found in the two vegetable fiber laminates, which may be caused by the different structures compared to BFRP - the mineral fiber composite.

In the future work, more advanded cutting edge image processing techniques such as truncated-correlation photothermal coherence tomography (TC-PCT) [81; 82] may improve the test sensitivity and resoluation for detection of subsurface details. In addition, the laser-based IRT techniques may provide additional information for the inspection of natural fiber composites [83; 63]. A finite element analysis (FEA) may also contribute to the research [74; 66].

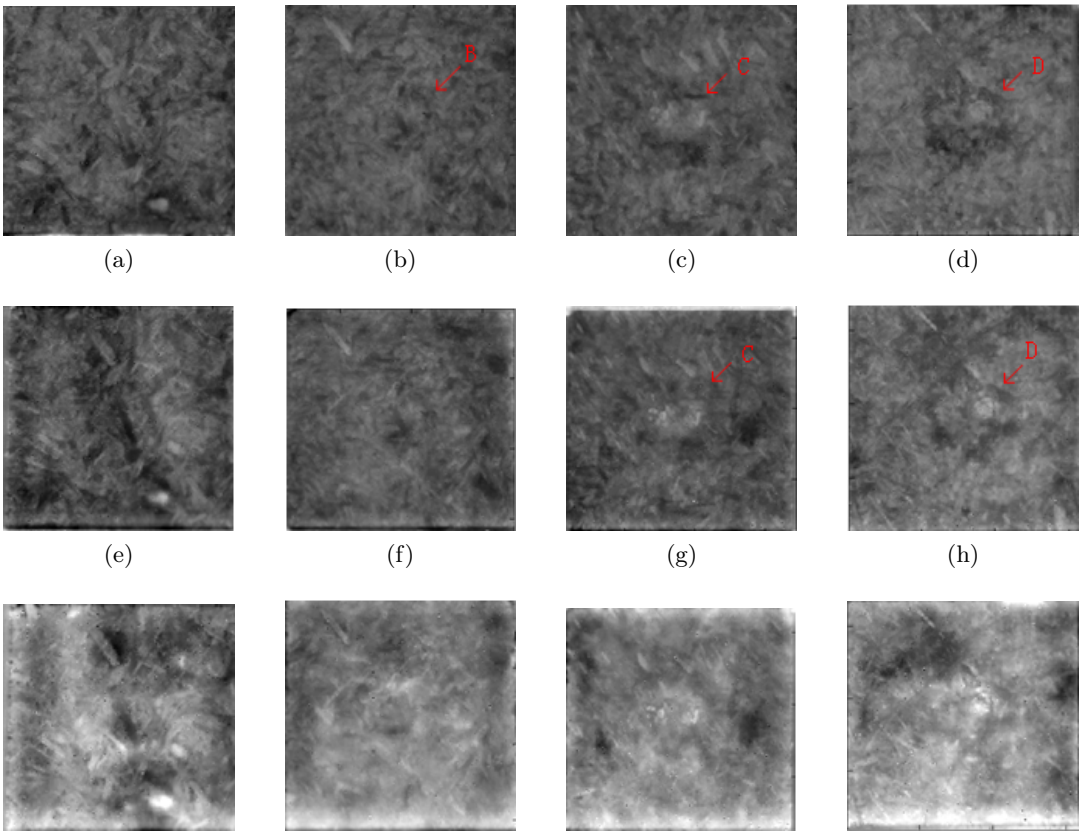

Figure 4.14: Phase-based LT results of SCB: (a) 5 J: 0.95 mm, (b) 10 J: 0.95 mm, (c) 20 J: 0.95 mm, (d) 30 J: 0.95 mm, (e) 5 J: 1.9 mm, (f) 10 J: 1.9 mm, (g) 20 J: 1.9 mm, (h) 30 J: 1.9 mm, (i) 5 J: 4.25 mm, (j) 10 J: 4.25 mm, (k) 20 J: 4.25 mm, (l) 30 J: 4.25 mm.

Table 4.5: Capabilities of different techniques.

Type of materials		BFRP	JHFP	SCB
Type of defect	Resin-rich	LT (phase) > PPT > PT (PCT) > VT (PCT)	LT (phase) > PPT > PT (PCT)	LT (phase) > PPT > PT (PCT)
	Impact damage	LT (phase) > PPT > PT (PCT) > VT (PCT) > UT	LT (phase) > PPT > PT (PCT) > VT (PCT)	VT (PCT) > LT (phase) > PPT > PT (PCT)
	Fiber identification	Unavailable	LT (phase) > PPT > PT (PCT)	LT (phase) > PPT > PT (PCT)
	Delamination	VT (PCT) > LT (phase) > PPT > PT (PCT) > UT > CW THz	No data	No data
Quantitative	Shallow-defect	PPT^1 > LT (phase)	PPT^1 > LT (phase)	PPT^1 > LT (phase)
	Deep-defect	LT (phase) > PPT^2	LT (phase) > PPT^2	LT (phase) > PPT^2

PPT^1: flashes modality; PPT^2: halogen lamps modality;

Chapter 5

Image Diagnostics of Impact Damage in Basalt and Carbon Fiber Composites

5.1 Introduction

Given the high specific stength and stiffness, CFRP are often used in the aerospace industry. However, their toughness is considerably low, therefore the impact damage resistance is not very high. Impact damage is one of the most important threats for the aerospace industry. Impact loading due to unwanted objects may occur during the process of manufacturing, assembly, maintenance, and operation. Impact damage can greatly affect the residual mechanical properties of CFRP even if the damage is barely visible [84]. Several solutions have been proposed in the past to enhance the impact damage resistance including the toughening of the matrix material [85]. Another solution is represented by fiber hybridization (usually with high strain to failure fibers) [86]. In this regard, glass fiber is the best option mainly because it is inexpensive [87]. Basalt fibers can be considered as an interesting alternative to glass fibers taking into account the mechanical properties and the environmental benefits [88]. This type of fiber, obtained from basalt rocks, has been demonstrated to be effective for the reinforcement of polymeric matrices [89; 90].

An in-depth study of impact damage in hybrid composites composed of basalt and carbon fibers has not been well documented yet in the open literature centred on thermographic diagnosis, while concerning basaltic materials, a couple of works should be taken into account in view of the discussion of section 5.4 [91; 92]. In this work, optical and mechanical excitation thermography were used to inspect BFRP, CFRP and basalt-carbon fiber hybrid specimens. Interestingly, two different hybrid structures including sandwich-like and intercalated (i.e., alternating sequence of basalt and carbon fabrics) were used. The advantages and disadvantages

of the two structures were studied. In addition, PPT based on phase transform was used to estimate the damage depth for QE in the optical excitation experimental set-up. PLST and PCT techniques were also used to process the raw thermographic data. CT, as an established technique, was used to validate the thermographic results. Finally, a comprehensive and comparative analysis was conducted in view of future industrial applications.

5.2 Basalt-Carbon Hybrid Composites

Concerning the materials used in this work, the plain weave basalt (BAS 220.1270.P) and carbon (CC160) fabrics have a fiber areal weight of 220 g/m^2 and 160 g/m^2, respectively. Bi-component epoxy resin (EC157+W152 MR) was selected as the polymeric matrix. The specimens were manufactured by a Resin Transfer Moulding (RTM) system and were cured for 12 h at room temperature and 4 h at 70 °C. All of the specimens have thirteen layers with similar overall fiber volume fraction, thickness and the dimension of 180 mm × 60 mm (Table 5.1). The hybrid specimen (BCs) was stacked as a sandwich structure with seven carbon

Table 5.1: Thickness and fiber volume fraction of specimens.

Specimen	Thickness $[mm]$	Fiber volume fraction	Dimension $[mm \times mm]$
B	3.40±0.05	0.315±0.01	180 × 60
C	3.50±0.04	0.325±0.01	180 × 60
BCs	3.50±0.04	0.319±0.01	180 × 60
BCa	3.45±0.05	0.321±0.01	180 × 60

fiber layers (core) and three basalt fiber layers (skins) for each side. The hybrid specimen (BCa) has seven basalt fiber layers and six carbon fiber layers alternatively stacked, keeping basalt plies as outer layers on both sides. Non-hybrid BFRP (B) and CFRP (C) specimens were also manufactured for comparative purposes. A falling dart impact machine (CEAST 9350) was used for low-velocity impact testing. All of the specimens were tested at 12.5 J by keeping constant the indenter mass (6.929 kg) with a hemispherical impact head (12.7 mm of diameter). The circular specimen holder has an external diameter of 60 mm and inner diameter of 40 mm [93].

Fig 5.1 shows the photographs of the impact regions from the rear side. CFRP specimen shows penetration of the dart through the thickness with splitting due to their brittle nature (Fig. 5.1b). On the contrary, BFRP specimen shows delamination without back surface splitting. BCs and BCa show an intermediate damage pattern with respect to BFRP and CFRP specimens. In particular, bulge is present on the surface of BCa. At least, this is true after a visual inspection.

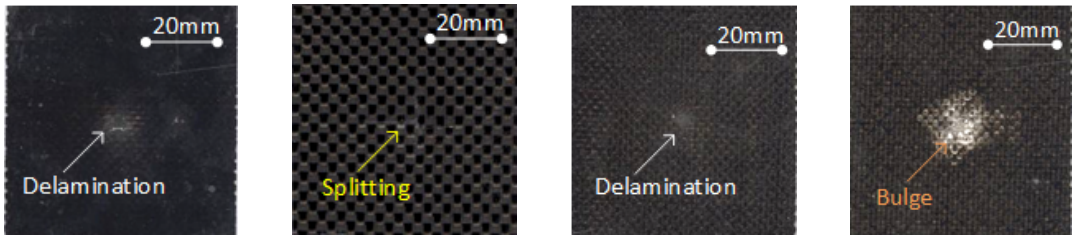

(a) (b) (c) (d)

Figure 5.1: Photographs of the impact regions (rear side): (a) B, (b) C, (c) BCs, (d) BCa.

5.3 Experimental Configurations

5.3.1 Optical Excitation Thermography

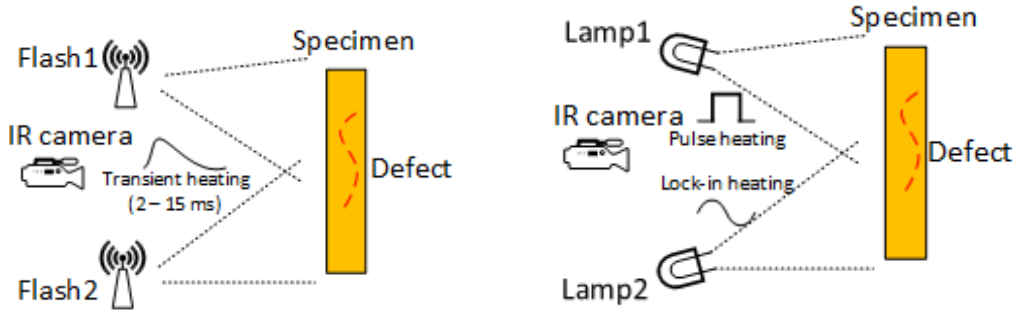

(a) (b)

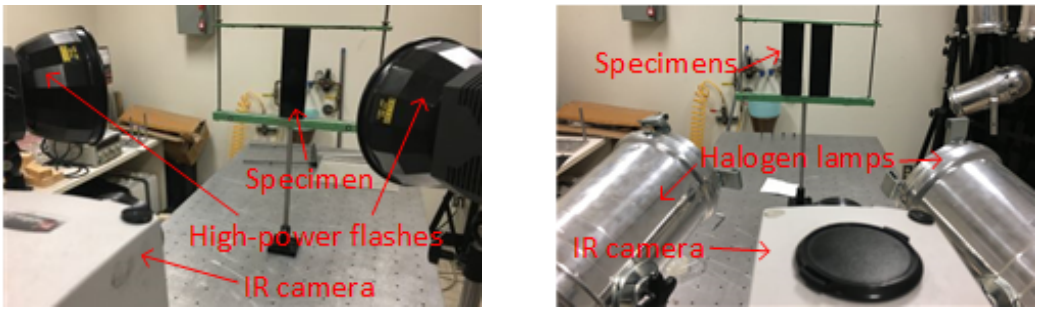

(c) (d)

Figure 5.2: Optical excitation thermography configurations: (a) schematic set-up for PT using flashes, (b) schematic set-up for LT and PT using lamps, (c) experimental set-up for PT using flashes, (d) experimental set-up for LT and PT using lamps.

Fig. 5.2a shows the schematic set-up for photographic flash modality, while the high-energy lamp modality is shown in Fig. 5.2b. Figs. 5.2c and 5.2d show the real experimental set-ups. Two Balcar FX 60 (6.4 KJ, 2 ms duration) producing optical flashes were used in this configuration, while two 'OMNLUX PAR64' (1000 W, 5 s duration) halogen lamps were applied as second and last thermal stimulus. A mid-wave IR camera with the frame rate of

~55 fps was used. The cooling times were set at 10 s and 20 s for flashes and halogen lamps modalities, respectively.

5.3.2 VT

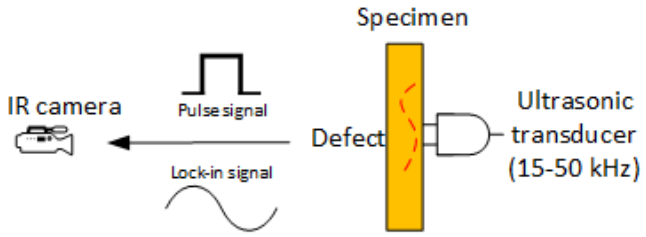

(a)

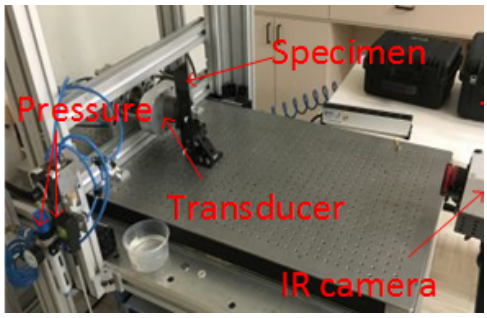

(b)

Figure 5.3: VT configuration, (a) schematic set-up, (b) experimental set-up.

Fig. 5.3 shows the VT set-up. The previous IR camera with the same frame rate equal to ~55 fps was used. The transducer was pressed (200 Pa) against the specimen and two periods of 0.2 Hz (10 s) lock-in ultrasonic waves were delivered.

5.4 Experimental Results and Analysis

In this work, all the images have the same scale as that in Fig. 5.1 (20 mm marked in white). RMF and CIS were performed prior to the application of PPT, PCT and PLST in PT regime, while RMF was applied prior to the application of phase transform in LT.

Fig. 5.4 shows the PCT results from the PT configuration using the flashes set-up. The BFRP specimen has the largest delaminated area among all the specimens (Fig. 5.4a), while the CFRP specimen has the smallest delaminated area in which the back surface splitting is also present (Fig. 5.4b). The BCs specimen (Fig. 5.4c) possesses a similar behaviour to that of the BFRP specimen. The BCa specimen with a bulge (Fig. 5.4d) shows a similar delaminated area as that of the BCs specimen, but slightly less extensive. This indicates the presence of less delamination in BCa specimen than that observed in the BCs specimen. Of particular interest,

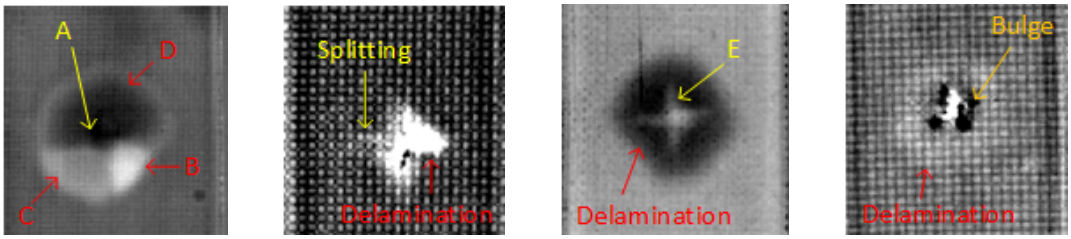

(a) (b) (c) (d)

Figure 5.4: PCT results of PT: (a) B: EOF 04, (b) C: EOF 04, (c) BCs: EOF 04, (d) BCa: EOF 04.

cross-shaped defects A and E were detected in the BFRP and BCs specimens, although they are clearer in Fig. 5.4c. In addition, regions B, C and D have different thermal signatures, as shown in Fig. 5.4a. This may indicate that B, C and D are located at different depths. PCT results linked to PT inspection and working with halogen lamps have similar results and for this reason, they are omitted from the text.

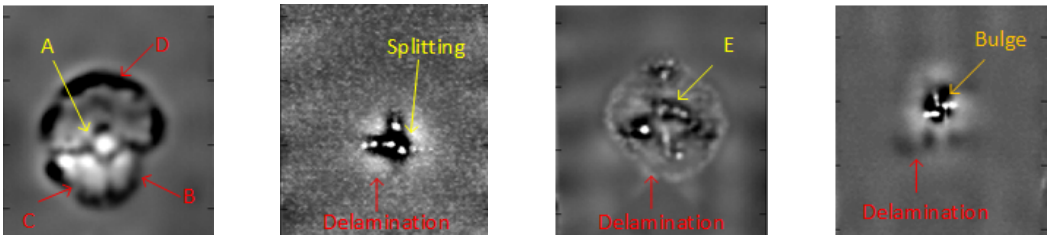

(a) (b) (c) (d)

Figure 5.5: PCT results of VT: (a) B: EOF 03, (b) C: EOF 03, (c) BCs: EOF 04, (d) BCa: EOF 03.

Fig. 5.5 shows the PCT results of VT. BFRP and BCs specimens show clearer delaminated areas than CFRP and BCa specimens. Cross-shaped defects A and E were inspected more clearly in Figs. 5.5a and 5.5c. Differently from PT results, regions B, C and D show the same contrast due to internal excitation (Fig. 5.5a). The delamination in the BCa specimen was also detected, but not as evident as in the PT results. VT results show an improved contrast, although PT can provide additional information. Table 5.2 shows the damaged areas obtained from PCT in PT and VT.

Table 5.2: Damaged areas obtained from PCT in PT and VT.

Specimen		B	C	BCs	BCa
Damaged area $[mm^2]$	PT	1267	296	936	787
	VT	1135	191	1045	469

Thermographic images obtained along with the increase of depth are useful for further analysis.

PLST, which can provide images along with the increase of depth, was used to process the PT data. Fig. 5.6 shows the PLST results. Halogen lamps were used since they can detect

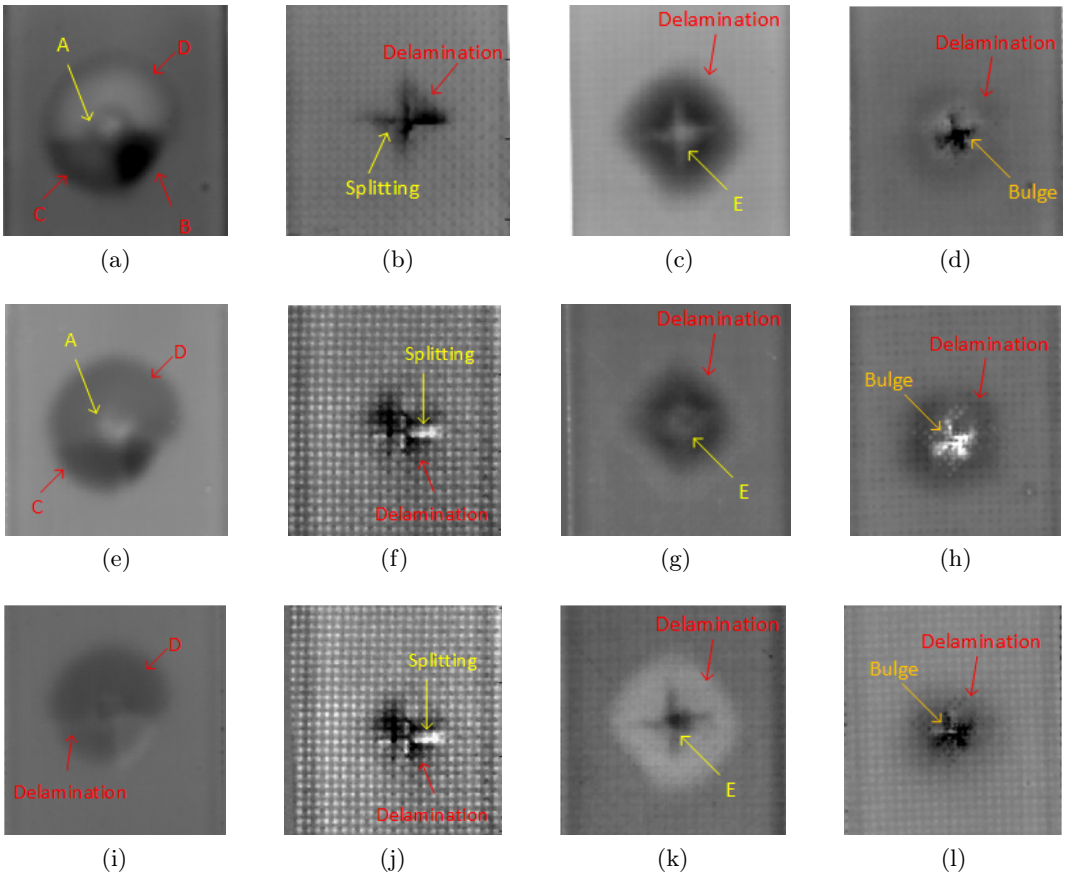

Figure 5.6: PLST results: (a) B: Loading 01), (b) C: Loading 01, (c) BCs: Loading 01, (d) BCa: Loading 01, (e) B: Loading 02, (f) C: Loading 02, (g) BCs: Loading 02, (h) BCa: Loading 02, (i) B: Loading 03, (j) C: Loading 03, (k) BCs:Loading 03, (l) BCa: Loading 03.

deeper depths than flashes. Table 5.3 shows the damaged areas obtained from PLST. PCT

Table 5.3: Damaged areas obtained from PLST.

Specimen		B	C	BCs	BCa
Damaged area $[mm^2]$	Loading 01	1110	192	897	644
	Loading 02	1006	254	439	524
	Loading 03	837	286	892	403

can detect larger damaged areas than PLST.

The delaminated area in the BFRP specimen decreases along with the increase of depth. This result is surprising, since BFRP has better toughness. The absorbed energy E_a created the delamination, but not splitting. Usually the delaminations are located near the back surface [94]. Of interest, region B is not present in Figs. 5.6e and 5.6i. This indicates that region

B is the nearest to the back surface and region D is located deepest (near to the impacted surface). On the other hand, the damaged area in the CFRP specimen increases along with the increase of depth. This is because splitting plays an important role in CFRP specimens.

The delaminated area in the BCa specimen decreases along with the increase of depth. However, BCs shows a different reaction after the impact in the middle of the depth axis (Fig. 5.6g). This result should be viewed taking into account that the sandwich-like cores consist of carbon fiber fabrics.

Although the PLST technique can link the loadings with the increase of the depths, it cannot provide quantitative values. This explains why PPT and LT were also used in this work; indeed, they can take advantage of phase transform to estimate the depth of images. Specifically, the thermal diffusivity α is a parameter of particular interest for calculating the depth by phase transform according to Eq. 2.4, and can be expressed as follows according to Eq. 1.1:

$$\alpha = \frac{k}{\rho c_p} \tag{5.1}$$

where, $c_p[J/kgK]$ is the specific heat at constant pressure, $\rho[kg/m^3]$ is the density, and $k[W/mK]$ is the thermal conductivity.

For composite materials, α can be calculated by [67; 68; 69]:

$$\alpha_{composite} = \sum_{1}^{N} (W_f \cdot \alpha_{material})_N \tag{5.2}$$

where, N is the number of constituent materials in the composite, and W_f is the fiber weight fraction.

Eq. 5.2 is linked to the fact that the α parameter is composed of physical quantities, but not of pseudo-physical quantities, in a similar manner as the C_p parameter. Therefore, taking into account the Buckingham theorem, it is possible to sum each layer for its volume fraction and mass fraction, respectively. This enables the final α and volume parameters to be obtained. Table 5.4 shows the thermal diffusivity α calculated according to Eq. 3.2, while Table 5.5

Table 5.4: Calculated thermal diffusivity α.

Specimen	B	C	B-C
Thermal diffusivity α $[10^{-7}m^2/s]$	0.88	2.08	1.43

shows the relationship between modulated frequencies f_b and depth z according to Eq. 2.4.

Fig. 5.7 shows the PPT results. It is possible to see how PPT displays similar images as those obtained using the PLST image processing (images along with the depth). However, PPT can provide the depth estimation. In the BFRP specimen, region B is the clearest at the depth of 0.68 mm and becomes blurry from the depth of 1.19 mm (Fig. 5.7i), while region C is the

Table 5.5: Relationship between modulated frequency f_b and depth z.

Modulated frequency $f_b[Hz]$		0.2	0.1	0.065	0.05	0.02	0.01
Depth $z[mm]$	B	0.68	0.96	1.19	1.36	2.15	3.05
	C	1.05	1.48	1.84	2.09	3.31	4.68
	B-C	0.87	1.23	1.52	1.74	2.75	3.88

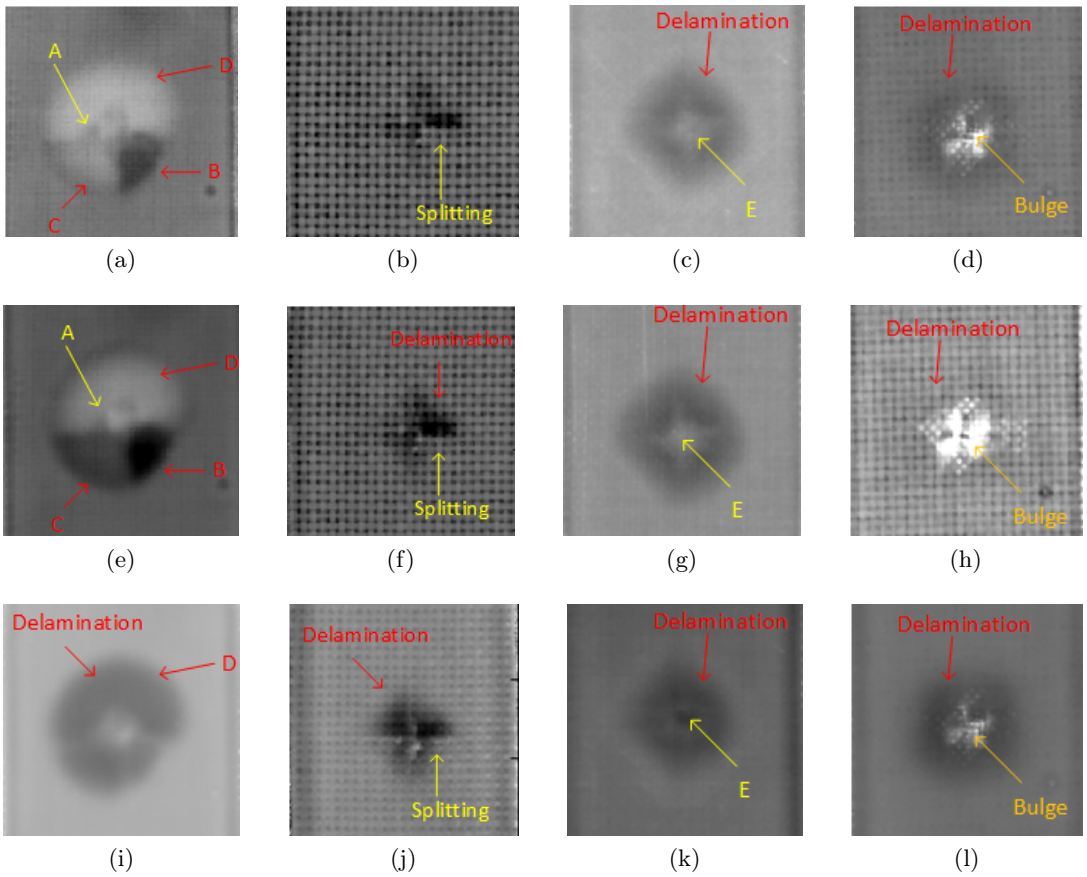

Figure 5.7: PPT results: (a) B: 0.68 mm, (b) C: 1.05 mm, (c) BCs: 0.87 mm, (d) BCa: 0.87 mm, (e) B: 0.96 mm, (f) C: 1.48 mm, (g) BCs: 1.23 mm, (h) BCa: 1.23 mm, (i) B: 1.19 mm, (j) C: 1.84 mm, (k) BCs: 1.52 mm, (l) BCa: 1.52 mm.

clearest at the depth of 0.96 mm (Fig. 5.7e). Region D appears between the depths of 0.68 mm and 1.19 mm. These features can indicate their depths. In the CFRP specimen, specific delaminated areas appear at the depths of 1.05 mm and 1.48 mm. Along with the depth, an increasing damage is shown. In order to probe deeper depths, LT was used and these results are shown in Fig. 5.8.

In the hybrid specimens, BCa shows a decreasing delamination along with the depth. However, BCs shows a particular reaction after the impact loading at the depth of 1.52 mm, as shown in Fig. 5.7k. This result coincides with the corresponding PLST results (Fig. 5.6g). This may be caused by the sandwich-like structure (carbon fiber fabric core). PLST can detect larger

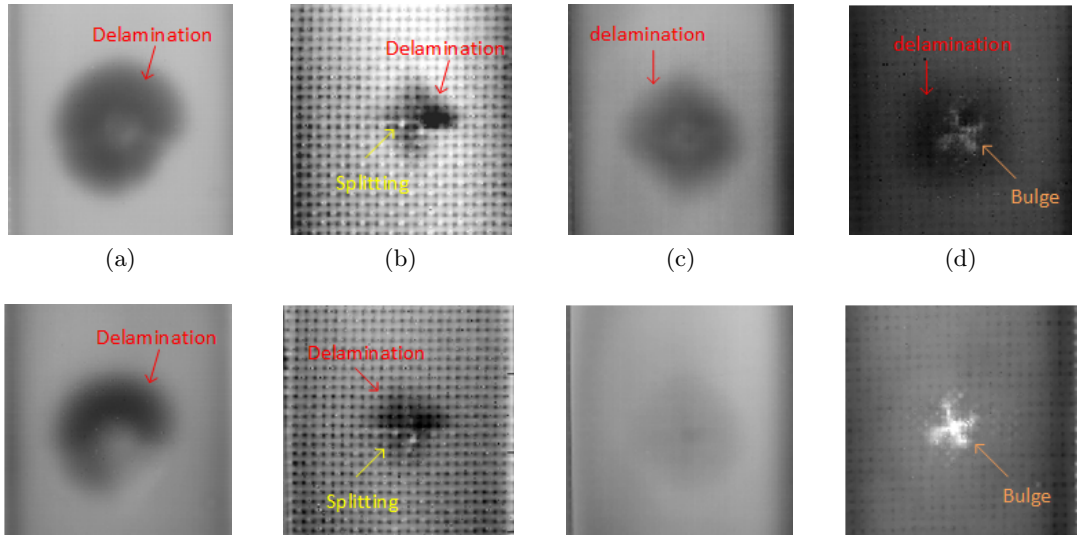

Figure 5.8: LT results: (a) B: 2.15 mm, (b) C: 2.09 mm, (c) BCs: 2.75 mm, (d) BCa: 2.75 mm, (e) B: 3.05 mm, (f) C: 3.31 mm, (g) BCs: 3.88 mm, (h) BCa: 3.88 mm.

damaged areas than PPT and LT. The delamination in Fig. 5.8c is more similar to that shown in Figs. 5.7c and 5.7g. This is of particular interest, since the depth of 2.75 mm is located in the basalt fiber fabric layers. Figs. 5.8g and 5.8h show less information because 3.88 mm is out of the depth for these types of specimens. Table 5.6 shows the damaged areas obtained from PPT and LT.

Table 5.6: Damaged areas obtained from PPT and LT.

Specimen		B	C	BCs	BCa
Damaged area $[mm^2]$	0.2 Hz	1059	140	850	587
	0.1 Hz	1020	243	830	567
	0.065 Hz	930	258	523	561
	0.05 Hz	/	261	/	/
	0.02 Hz	923	275	721	540
	0.01 Hz	709	/	/	/

Fig. 5.9 shows the 100 μm-resolution CT slices, which were used to validate the thermographic results. In BFRP specimen, the largest delamination appears at a depth of 0.1 mm (Fig. 5.9a). Region B is the clearest at a depth of 0.6 mm (Fig. 5.9e), while region C appears at a depth of 0.8 mm (Fig. 5.9i). Regions B and C disappear at a depth of 1 mm (Fig. 5.9m), while region D is the clearest at this depth. The delamination is the slightest at the depth of 3.3 mm (Fig. 5.9q). These CT slices validate the thermographic results obtained from PPT and LT by depth increase. In the CFRP specimen, specific delamination appears at the depths of 0.5 mm and 1.7 mm (Figs. 5.9f and 5.9j). The largest delamination is shown at the depth of

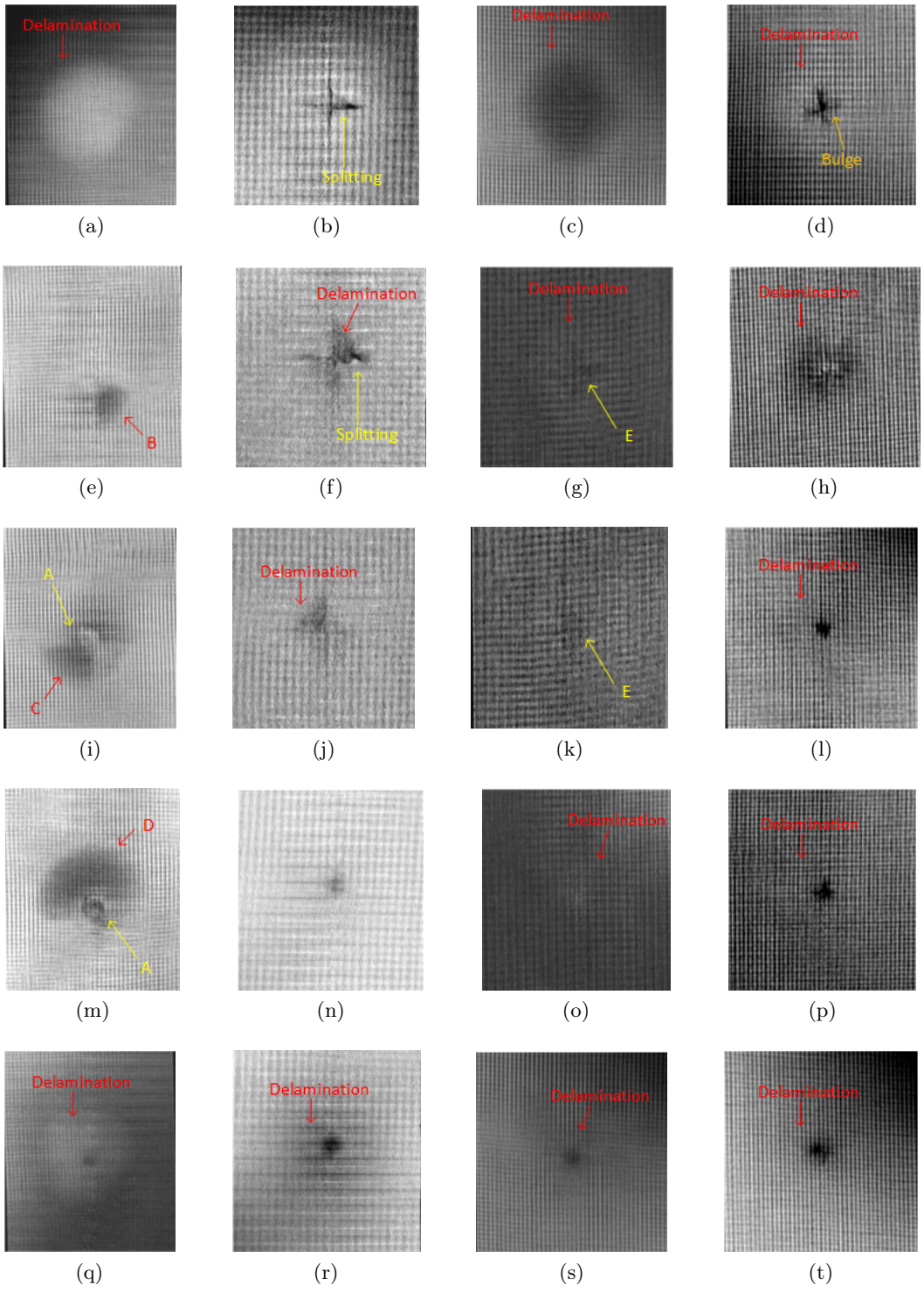

Figure 5.9: CT slices: (a) B: 0.1 mm, (b) C: 0.1 mm, (c) BCs: 0.1 mm, (d) BCa: 0.1 mm, (e) B: 0.6 mm, (f) C: 0.5 mm, (g) BCs: 0.8 mm, (h) BCa: 0.8 mm, (i) B: 0.8 mm, (j) C: 1.7 mm, (k) BCs: 1.7 mm, (l) BCa: 1.7 mm, (m) B: 1 mm, (n) C: 3 mm, (o) BCs: 2.7 mm, (p) BCa: 2.7 mm, (q) B: 3.3 mm, (r) C: 3.3 mm, (s) BCs: 3.3 mm, (t), BCs: 3.3 mm.

3.3 mm. These CT slices also validate the thermographic results linked to CFRP in PPT, LT and PLST.

In the slices of the hybrid specimens, BCs shows a decreasing delamination extension along with the depth, which compares quite well the thermographic results. BCs shows the largest delaminated area at a depth of 0.1 mm (Fig. 5.9c). Then, the delamination decreases along with the depth. However, it shows a sharply decreasing delaminated area at a depth of 1.7 mm (Fig. 5.9k), which is located at the middle depth (carbon fiber fabric core). This feature also coincides with the PPT (Fig. 5.7g) and PLST (Fig. 5.6g) results. Overall, the 100 μm-resolution CT slices can validate the thermographic results by depth increase, although the thermographic images are clearer.

5.5 Summary

Both optical and mechanical excitation thermography are useful image diagnostics for impact damage in BFRP, CFRP and basalt-carbon fiber hybrid composites. If compared to the 100 μm-resolution CT technique which was used to validate the thermographic results, IRT has the abilities to provide clear images and additional information. PCT can detect the largest damaged areas, while PPT and LT can identify the smallest damaged areas. However, the depth values of defects can be estimated in PT and LT by phase transform. PLST can also provide thermographic images (Loadings) linked to the increment of the depth. However, it cannot provide quantitative information, which is of paramount interest. These advanced image processing techniques enhance the advantages of IRT.

Absorbed energy E_a was more easily converted into delamination in BFRP thanks to its lower interlaminar shear strength. On the contrary, E_a created back surface splitting in CFRP thanks to its inherent limited ductility. Hybridization with basalt fibers improved the toughness of carbon-based laminates to a different extent depending on the stacking sequence. The basalt-carbon fiber hybrid specimen (BCs) with sandwich-like structure shows a pronounced delaminated area similar to that observed in the BFRP specimen, while the basalt-carbon fiber hybrid specimen (BCa) with alternately stacked structure shows characteristics much more similar to those of the CFRP specimen. Summarizing, a more extensive delaminated area was detected in the BCs specimen than in the BCa specimen. This is because delaminations are probably more numerous in the BCa specimen, but less extensive due to the multiple basalt-carbon interfaces. However, BCa shows a bulge on the back side of impact.

This study provides a reference for taking advantage of different basalt-carbon fiber hybrid structures for specific industrial applications [74; 66]. In particular, it confirmed the possibility of detecting damage at different depths. This is of particular interest with a view to correlating the damage and its extension with the residual properties of composite laminates. A simulation using the finite element method (FEM) may contribute to the further understanding of

sandwich-like and alternating stacked structural characteristics subjected to known velocities of impact.

Chapter 6

Image Diagnosis for Micro-sized Flaws in CFRP

6.1 Introduction

Three-dimensional (3D) CFRP are increasingly used for aircraft construction due to their exceptional stiffness and strength-to-mass ratios. Composites made from 3D textile preforms can reduce both the weight and manufacturing cost of advanced composite structures within aircraft, naval vessels and the blades of wind turbines [95]. The in-plane stiffness and strength of 3D woven composites are lower; while the out-of-plane properties are higher compared to conventional 2D laminates [96]. Assembly of 3D complex composite structures requires efficient joining methods. The most frequently used joint found in structural applications is the T-joint.

The purpose of T-joints is to transfer flexural, tension and shear loads to the skin. T-stiffeners are used extensively in aircraft wings in order to prevent skin buckling during wing loading. However, designing composite joints is more difficult than metallic joints due to the mechanical properties of composite materials [97].

In the design of T-joints, filler is inserted in T-joints and resin is used to reinforce the structure. The fiber insertion technique has the potential of creating a low-cost T-joint with improved damage tolerance and failure strength [98]. However, incomplete infusion of T-joints core (dry-core) is a typical issue. Figure 6.1 shows typical dry-core in a non-stitched CFRP T-joint.

Stitching [99] is used to reduce dry-core and reinforce T-joint structure [100]. However, stitching might lead to new types of flaws due to the characteristics of its structure.

NDT of composite materials is complicated due to the wide range of flaws encountered (including delamination, micro-cracking, fiber fracture, fiber pullout, matrix cracking, inclusions,

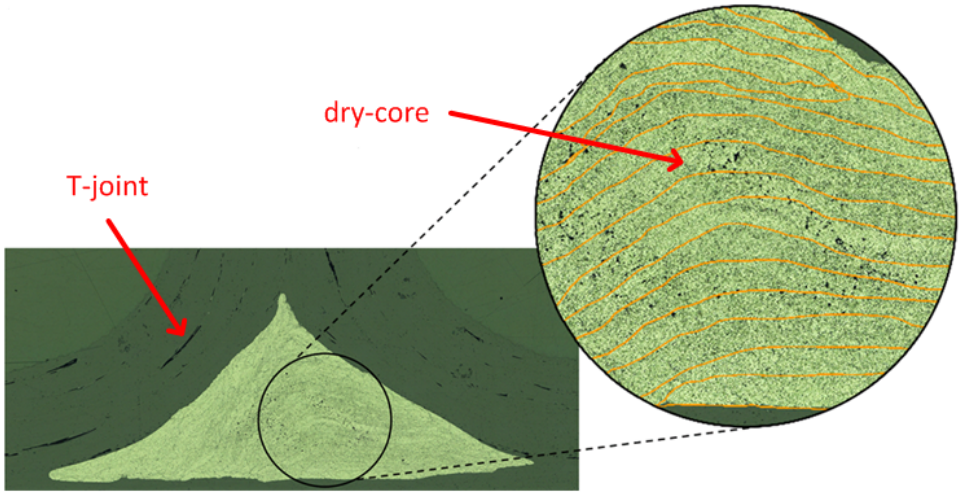

Figure 6.1: Typical dry-core in a non-stitched CFRP T-Joint (microscopic inspection).

voids, and impact damage). The ability to quantitatively characterize the type, geometry, and orientation of flaws is essential [101] [14]. The ability to identify and characterize such micro-sized flaws accurately is challenging. [60]

IRT is becoming increasingly popular in the recent years as a NDT technique due to its fast inspection rate, contactless, spatial resolution and acquisition rate improvements of infrared cameras as well as the development of advanced image processing techniques. It is used for diagnostics and monitoring in several fields such as electrical components, thermal comfort, buildings, artworks, composite materials and others [64].

In this work, established techniques including microscopic inspection, UT, PT, VT, LST using lock-in method are performed to detect a stitched 3D T-joint CFRP. A new micro-LLT is used to detect a stitched CFRP T-joint. An 18 μm resolution micro-CT is used to validate the infrared results. A comparison of the micro-LLT and micro-CT is conducted. Then, a FEA simulating the infrared results is performed. The geometrical model needed for finite element discretization is developed from the micro-CT. There is little information in the open literature on FEA for IRT on micro-sized flaws. The infrared experimental results are explained on based of the FEA.

In addition, lock-in micro-LLT is also proposed on the basis of lock-in technique and pulsed pulsed micro-LLT. Micro-VT and micro-LST are also proposed by using a micro-lens. These new techniques are also used to investigate the submillimeter porosities in the stitched T-joint CFRP specimen. Finally a comparison of the experiments and simulation is conducted.

6.2 T-joint CFRP

6.2.1 Materials System

The T-joint specimen selected for this evaluation was sewn using stacked TC-06-T 3K carbon fiber. The 3D architecture was woven using 3K/12K carbon fiber. A continuous row of stacked 12K tow fiber was used for insertion. A toughened epoxy resin infusion system was selected.

6.2.2 Fabrication

The T-joint specimen was fabricated using 3D preform consisting of multiple layers of woven fabric. The complete 3D fabrication model is shown in Fig. 6.2a. A high-resolution photograph of the fabrication is shown in Fig. 6.2b.

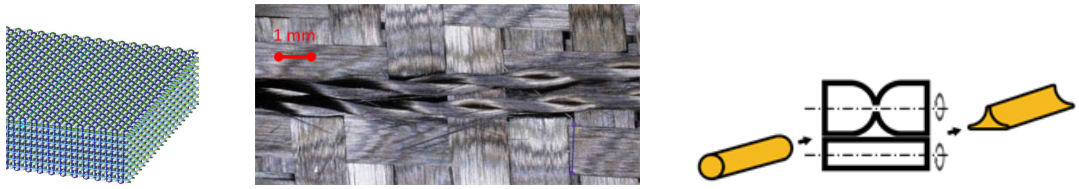

(a) (b) (c)

Figure 6.2: (a) The complete 3D fabrication model, (b) a high-resolution photography of the preform, (c) the procedure of a triangular-shaped noodle processing for T-joint insertion.

The noodle for the T-joint insertion was pre-shaped through compaction. During processing, the twisted round-shaped stacked 12K carbon fiber tows were placed into the molding tool and compacted to a triangular-shape as the tool was clamped together. The noodle processing procedure is shown in Fig. 6.2c. After the fiber insertion process was completed, the resin infusion process was initiated.

6.2.3 Geometry

For composites, meso-geometry can influence processing and performance properties. To describe the meso-geometry, the textile unit cell model is shown in Fig. 6.3a. The complete single layer preform model is shown in Fig. 6.3b.

The geometrical model describing the internal geometry is developed on the basis of the method proposed by Ito and Chou [102]. The model consists of four intertwined yarns surrounded by the isotropic matrix. There are two warp yarns in the longitudinal direction and two fill yarns in the transverse direction. Each yarn is a unidirectional composite in the material coordinate system with orthotropic properties [103].

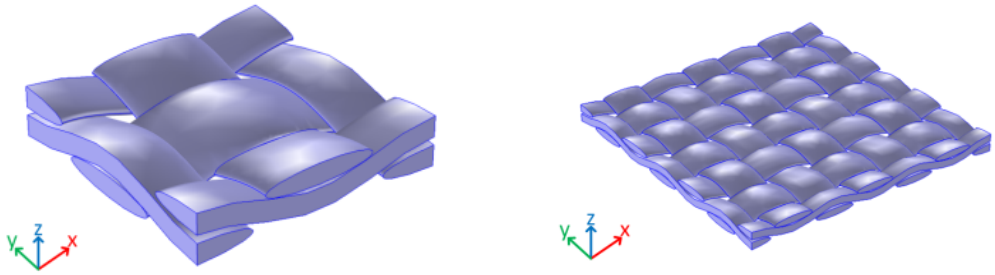

(a) (b)

Figure 6.3: (a) The textile unit cell model (mm), (b) the single layer preform model.

The equations proposed by Ito and Chou [102] for the yarn geometry is used for developing the geometrical model. The warp yarn path curve on the fill face is described by

$$z_0(x) = \frac{h_y}{2}\sin(\frac{2\pi}{a}x), where -\frac{a}{4} < x < \frac{a}{4} \tag{6.1}$$

and the fill yarn cross-section curve on the same face by

$$z_1(x) = \frac{2h_c}{a-2a_g}\sqrt{(2x-a_g)(a-a_g-2x)} + h_y - h_c, where \frac{a_g}{2} < x < \frac{a}{4} \tag{6.2}$$

where h_y is the yarn thickness, a is the dimension of the model in either the fill or warp directions (warp or fill faces, respectively), a_g is the gap width between two adjacent transverse yarns, and

$$h_c = \frac{h_y}{2}(\sin(\frac{\pi a_g}{a}) + 1) \tag{6.3}$$

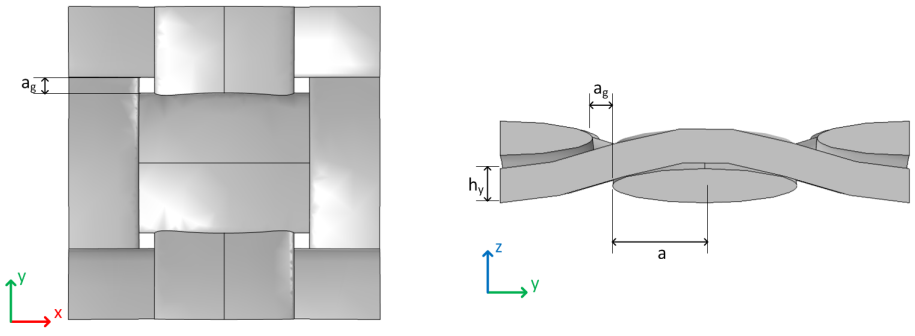

Figure 6.4: The model geometrical relation.

The model geometrical relation is shown in Fig. 6.4. The values of the parameters are shown in Table 6.1.

Table 6.1: The model geometrical parameters

Geometrical Parameters	Value
Weave length in warp direction, a^w (mm)	6
Weave length in fill direction, a^f (mm)	6
Gap width in warp direction, a_g^w (mm)	0.3
Gap width in fill direction, a_g^f (mm)	0.3
Yarn thickness, h_y (mm)	0.6

6.2.4 Specimen

The complete stitched T-joint is shown in Fig. 6.5a. The sample contains 6 stitching lines. The purpose of the stitching is to consolidate the T-joint structure and to reduce dry-core. The sample measures 152 mm in length, 148 mm in width, 63 mm in height, and 5 mm in thickness (excluding the T-stringer), as shown in the figure.

The front side of the sample is shown in Fig. 6.5b. A 10 mm × 152 mm zone was inspected using micro-LLT and micro-CT.

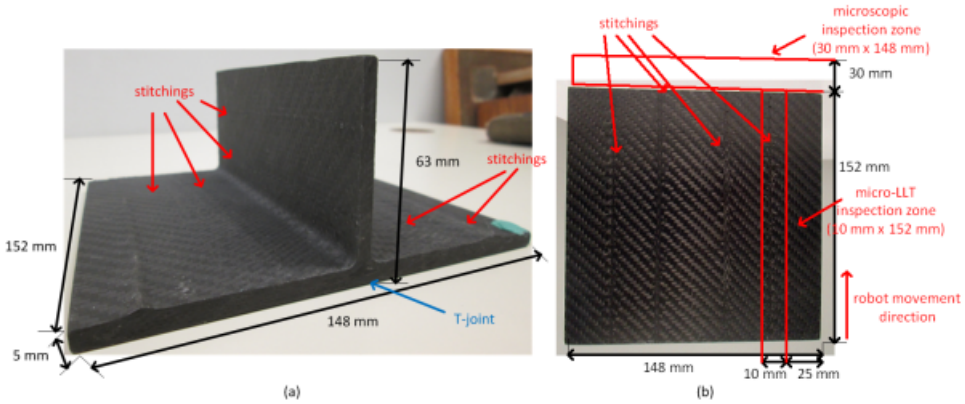

Figure 6.5: (a) Complete stitched 3D T-joint sample, (b) front side of the sample.

6.3 Inspection Results Using the Established Techniques

6.3.1 Microscopic Inspection

Microscopic inspection was performed through cutting and polishing a part of 30 mm × 148 mm shown in Fig. 6.5. The purpose is to investigate the structure and internal flaws in the sample.

The grinding and polishing procedure is automated, as is the procedure for the stitching of many images obtained by auto-focal and self-travelling microscope. These procedures are thus automated, but they require supervision. Images are obtained using optical as opposed to

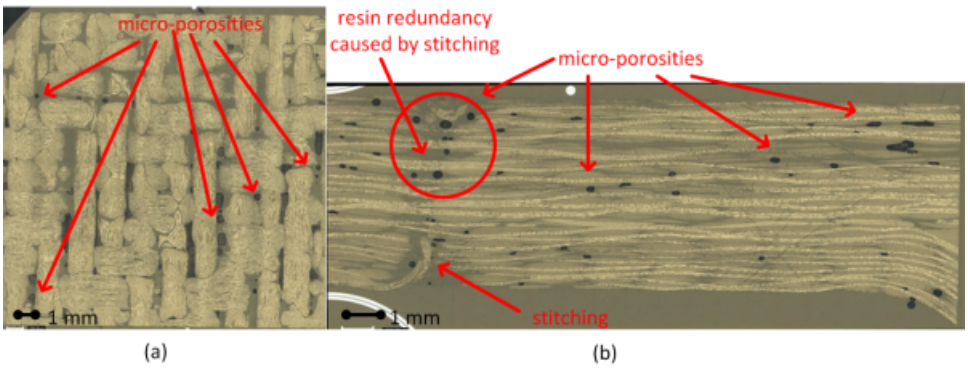

Figure 6.6: Microscopic inspection results of T-joint CFRP (a) top-section, (b) cross-section.

SEM, which requires polishing instead of gold sputtering. However, the overall time required for either device is probably comparable and optical is far more accessible. The physical size corresponding to the assembled image is about 12 mm × 12 mm, which is the largest that can be accommodated. The resolution of the inspection is 7 μm. The quality of the images is good and sufficient for inspection. There are scratches, watermarks and dirt on these first images but these can be sorted.

The microscopic inspection results are shown in Fig. 6.6. Figure 6.6a shows the micro-porosities in top-section. Figure 6.6b shows the stitching and micro-porosities in cross-section. The stitching is shown in the image. In Fig. 6.6b, more micro-porosities in resin redundancy zone are inspected than in other zones. Most micro-porosities measure a diameter of around 0.1 mm to 0.2 mm shown in Fig. 6.6.

6.3.2 UT

UT was performed to inspect the entire sample. Water immersion method was used. The detection results using the transducer with the frequency of 2.25 MHz are shown in Fig. 6.7. The images were acquired before the microscopic inspection. Figure 6.7a shows the detection result using pulsed-echo technique. Pulsed-echo technique uses a transducer to emit ultrasonic beams, and uses the same transducer to receive the reflected signals. Figure 6.7b shows the detection result using through-transmission technique. Through-transmission technique uses a transducer to emit ultrasonic beams, and uses another transducer with the same parameters to receive the transmitted signals on the opposite side. Figure 6.7c shows the color scale for signal amplitude percent.

In Fig. 6.7a, many abnormalities are detected. Some of them might be voids and porosities. However, it is a challenge to identify and characterize them due to the attenuation and scattering of the ultrasonic beams, which are caused by the complex internal structure. In Fig. 6.7b, three large-sized abnormalities are shown. They might be resin abnormalities or internal structural flaws. However they are also difficult to be identified and characterized accurately.

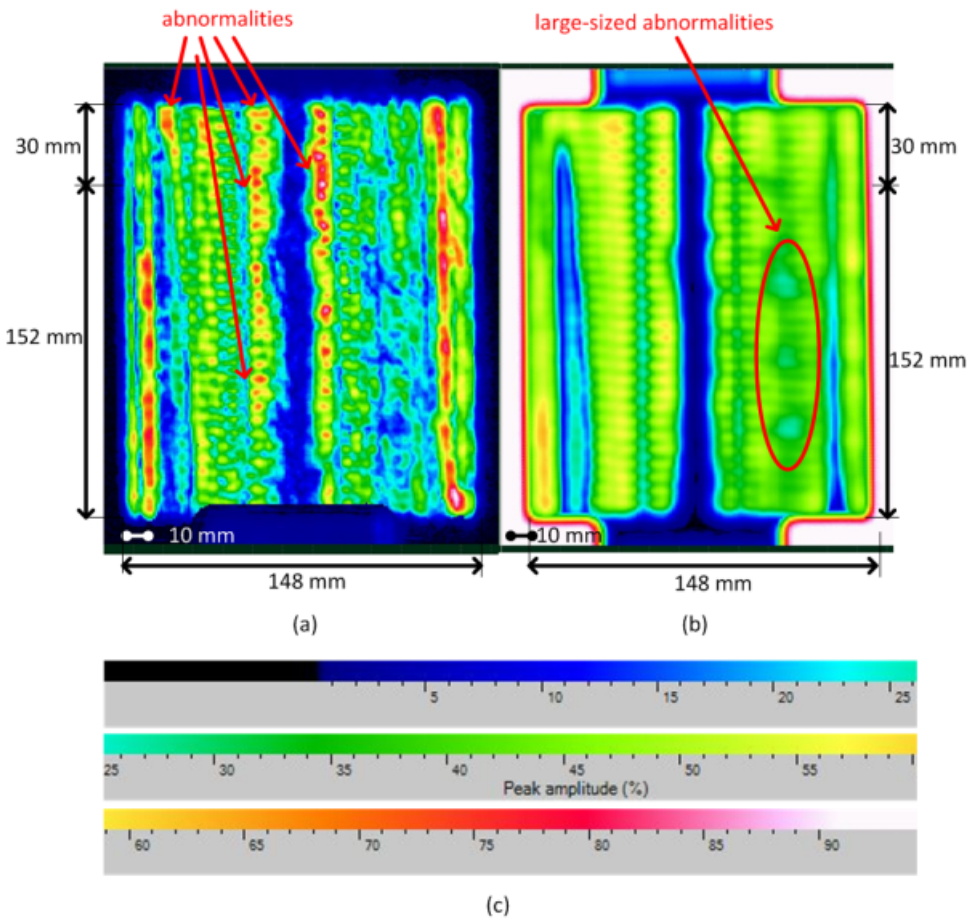

Figure 6.7: UT results of T-joint CFRP (2.25 MHz) (a) pulsed-echo, (b) through-transmission, (c) color scale for signal amplitude percent.

UT using transducers with the frequencies of 5 MHz, 10 MHz, 15 MHz were also performed. However, none of them can identify and characterize the internal flaws accurately.

6.3.3 PT

PT was performed to detect the sample. Figure 6.8a shows the classical pulsed thermography set-up [4]. Figure 6.8b shows the experimental set-up. In the set-up, a mid-wave infrared (MWIR) camera (FLIR Phoenix, InSb, 3-5 μm, 640 $\times$ 512 pixels) at a frame rate of 55 Hz was used to record the temperature profile. Two photographic flashes (Balcar FX 60 with pulse duration of 5 ms and producing 6.4 kJ per flash) were used to heat the sample.

Figure 6.9 shows the detection results before the microscopic inspection. Figure 6.9a shows the image from first derivative image processing. Figure 6.9b shows the image from second derivative image processing. In Fig. 6.9, some voids measured around 1 mm to 2 mm are inspected. PT can detect large-sized flaws. However it is a challenge to characterize submillimeter flaws. Several image processing methods were conducted. However, none of them can

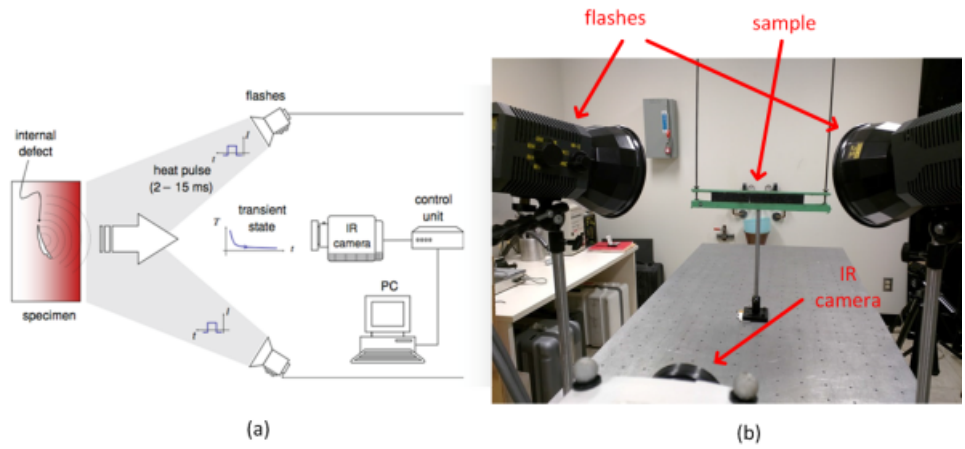

Figure 6.8: (a) Classical PT set-up[4], (b) experimental set-up.

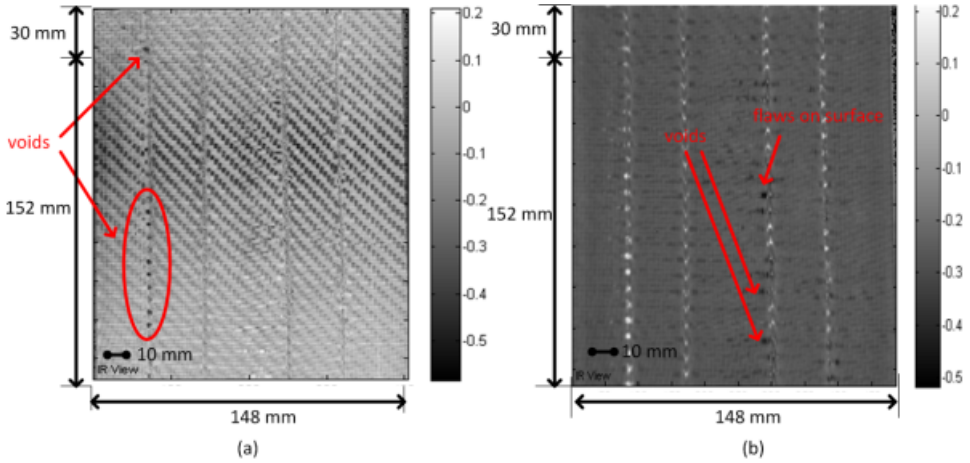

Figure 6.9: PT results of T-joint CFRP (a) first derivative, (b) second derivative.

identify and characterize submillimeter flaws.

6.3.4 VT

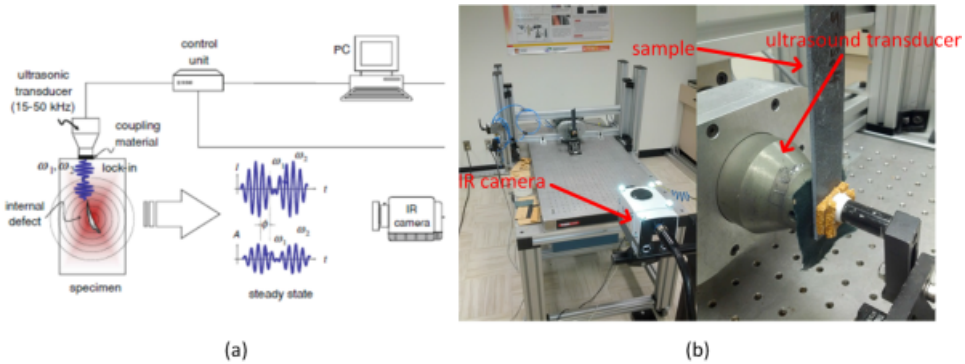

Figure 6.10: (a) Classical VT set-up[4], (b) experimental set-up.

Figure 6.10a shows the classical VT set-up[4]. Figure 6.10b shows the experimental set-up. In the set-up, a mid-wave infrared (MWIR) camera (FLIR Phoenix, InSb, 3-5 μm, 640 $\times$ 512 pixels) at a frame rate of 55 Hz was used to record the temperature profile. The transducer horn was pressed against the sample and a burst of ultrasound wave (20 kHz, 2200 W) at a modulation frequency of 0.25 Hz and with amplitude modulated between 10 - 30% of maximum power was delivered to the sample.

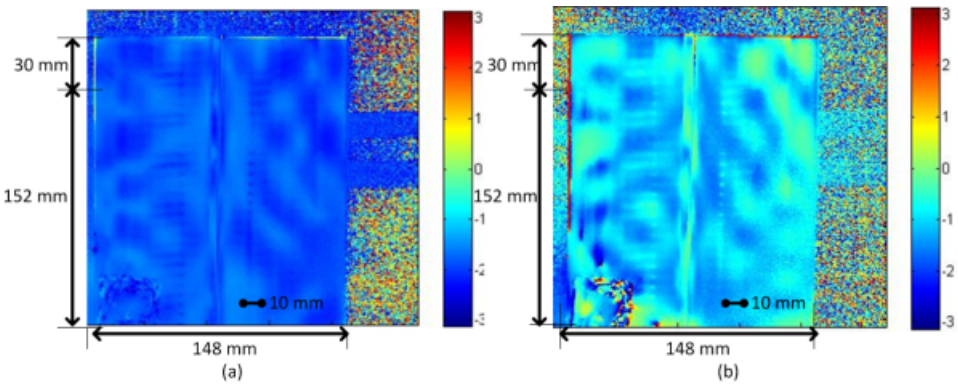

Figure 6.11: VT results of T-joint CFRP.

Figure 6.11 shows the detection results before the microscopic inspection. None of the two images can identify flaws. The potential reason is an heat source issue coupling caused by the complex internal structure.

6.3.5 LST and LT

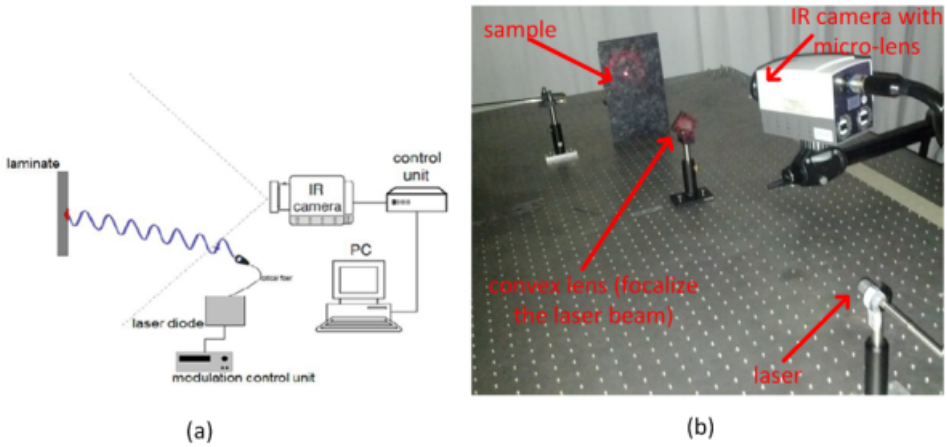

Figure 6.12: (a) Classical LST set-up[5], (b) experimental set-up[6].

Figure 6.12a shows the classical LST set-up[4]. Figure 6.12b shows the experimental set-up. In the set-up, a mid-wave infrared (MWIR) camera (FLIR Phoenix, InSb, 3-5 μm, 640 $\times$ 512 pixels) at a frame rate of 55 Hz was used to record the temperature profile. A diode-laser

was used for heating source. The laser wavelength is 805 nm. The laser beam power is 4.2 W. A convex lens was used to focalize the laser beam. A micro-lens was used to detect the submillimeter flaws. The magnification of the micro-lens is 1 ×. Lock-in method was used to identify and characterize the internal flaws.

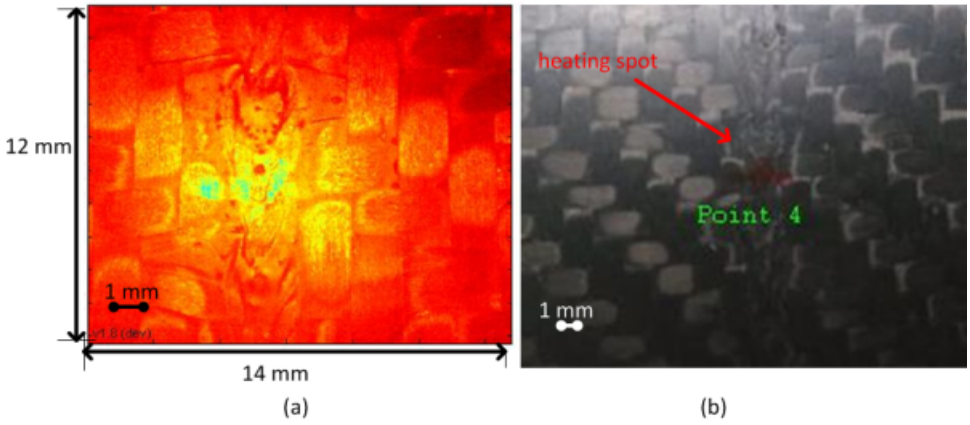

Figure 6.13: (a) image prior to heating, (b) heating spot.

Figure 6.13a shows the image prior to heating. The infrared image measures 12 mm × 14 mm. Point 4 is the heating spot shown in Fig. 6.13b.

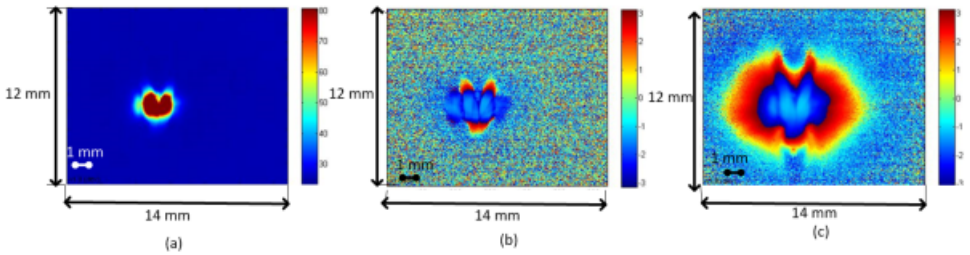

Figure 6.14: ST results of T-joint CFRP (locked-in method) (a) surface, (b) depth: 0.21 mm, (c) depth: 0.65 mm

Figure 6.14a shows the detection result on the surface. Figure 6.14b shows the result from the depth of 0.21 mm. Figure 6.14c shows the result from the depth of 0.65 mm. In Fig. 6.14, no defect is detected. LST can detect internal structure and flaws using lock-in method. However, it is a time-consuming technique. It is difficult to inspect the entire sample (152 mm × 148 mm) using laser spot thermography.

6.4 Micro Laser Line Thermography (Micro-LLT)

In conventional IRT set-up, a relatively homogenous heat source such as flash or halogen lamps is used to heat sample surface, and then temperature distribution on the surface is recorded with an infrared camera. Conventional IRT can detect a broad variety of defects, such as voids, pores, or delaminations [104]. However, it is difficult to detect micro-sized flaws due to CFRP structural complexity, which leads to heat diffusion abnormity, especially for interlayer detection.

To tackle this problem, LST may be an effective solution, which is currently experiencing intense research activities. This approach uses a laser spot to scan over sample surface. Changes in the heat conductivity lead to changes in the thermal footprint. This approach may effectively reduce the impact of CFRP structural complexity. However, this approach needs a massive amount of workload and time due to spot inspection feature. Therefore, in this work, a new approach 'micro-LLT' is presented to utilize LST's advantage, and to reduce its disadvantage.

LLT has been used to detect surface cracks [105]. Li et al. [105]used a beam expander and a cylindrical lens to convert a laser spot with a radius of around 0.9 mm to a laser line source. However, the detection of other types of flaws was poorly documented. In this work, a galvanometer scanning mirror with a frequency of 600Hz is used to generate a laser line [106]. A micro-lens was used to identify and characterize micro-sized flaws.

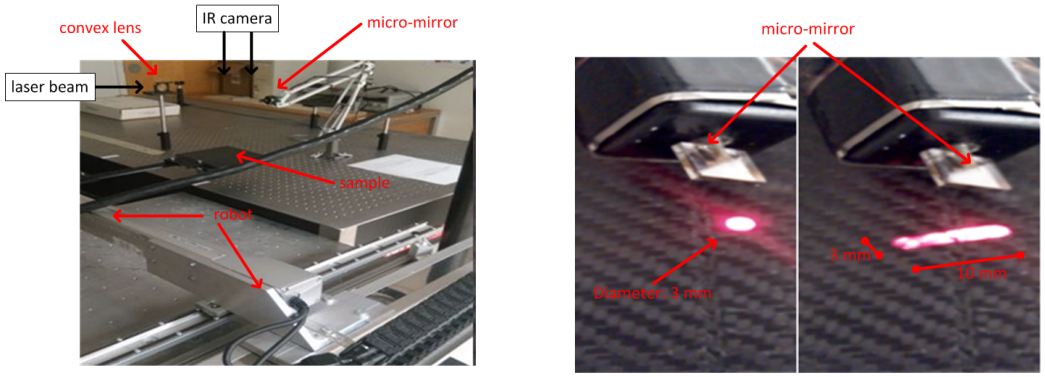

(a) (b)

Figure 6.15: (a) Micro-laser line thermography experimental set-up, (b) laser spot to laser line.

Figure 6.15a shows the experimental set-up for micro-LLT. In the set-up, the sample was fixed on a robot. A mid-wave infrared (MWIR) camera (FLIR Phoenix, InSb, 3-5 μm, 640 $\times$ 512 pixels) at a frame rate of 55 Hz was used to record the temperature profile. A diode-laser with wavelength of 805 nm, a beam power of 2.9 W, and a heating time of 0.5 s was used. A convex lens was used to focus the laser beam and a micro-lens was used to identify and

characterize the micro-sized flaws. The magnification of the micro-lens is 1×. A micro-mirror (7 mm diameter) was mounted between the IR camera and the sample. GSI G124 open loop optical scanner (±24° optical scan angle) was used to deflect the mirror. In Fig. 6.15b, the laser spot was converted to a laser line when the micro-mirror swung at the frequency of 600 Hz. Figure 6.15b shows the heat source. Its length is around 10 mm and its width is around 3 mm. [60]

Figure 6.5b shows the inspected zone. The laser line crosses a stitching line. The robot moved per 3 mm towards the direction shown in Fig. 6.5b. A total of 51 tests were performed to detect the 10 mm × 152 mm area shown in Fig. 6.5b.

A micro-CT inspection was performed on the same 10 mm × 152 mm zone shown in Fig. 6.5b. The resolution of the inspection is 18 μm. The purpose of the x-ray tomography inspection is to validate the micro-LLT results.

6.4.1 Experimental Results

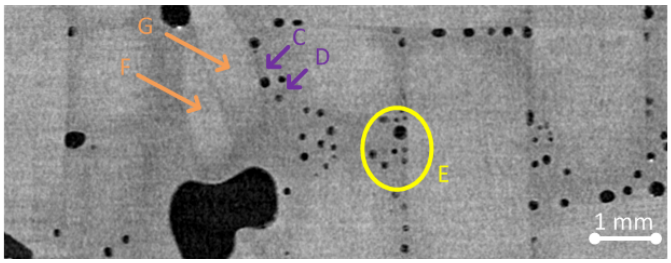

(a)

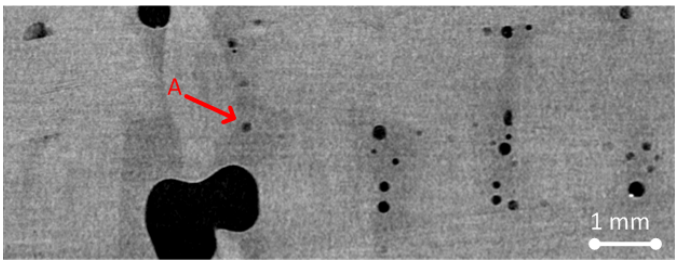

(b)

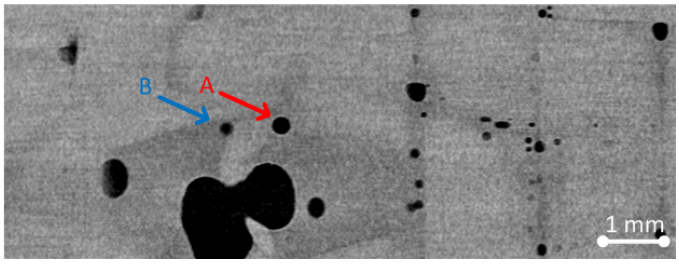

(c)

Figure 6.16: The x-ray tomography results (a) surface, (b) depth: 90 μm, (c) depth: 0.18 mm.

Figure 6.16 shows slices from the micro-CT results. Some specific micro-porosities are marked in the images. Some micro-porosities are inspected on the surface.

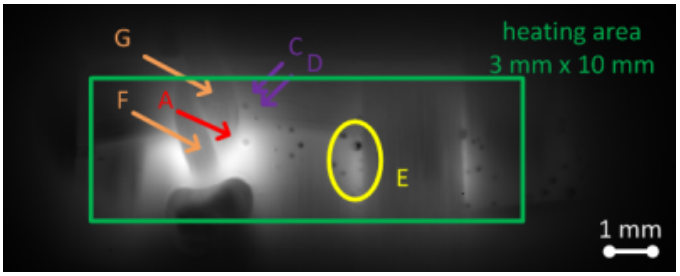

(a)

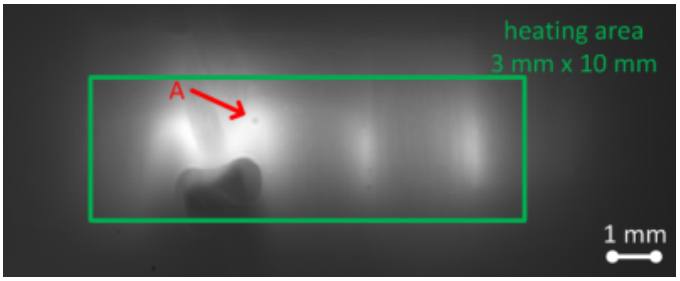

(b)

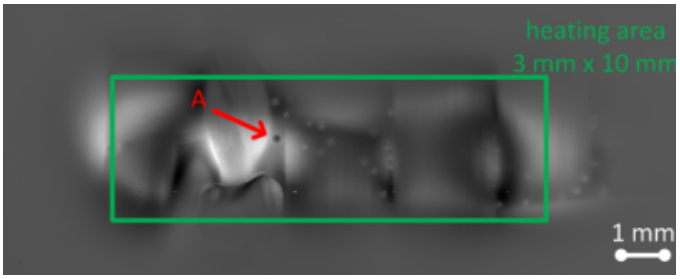

(c)

Figure 6.17: The micro-laser line thermography results (a) cold image, (b) raw image with contrast adjustment, (c) PCT.

Figure 6.17 shows the micro-LLT results in the same zone. The heating area is marked in green.

The result of an infrared inspection is a sequence of infrared images which contains: the sample before heating, the moment when the laser line heats the sample, the rise of the temperature profile and the temperature profile decrease [63].

Figure 6.17a was acquired from CIS at 0.8 s (the heating time is 0.5 s and the thermal diffusion time during temperature profile decrease is 0.3 s). In Fig. 6.17a, some micro-porosities on the surface such as C and D (marked in purple) are detected. However, some other micro-porosities on the surface such as some in the zone E (marked in yellow) are not detected. The potential cause is the IR camera resolution limitation. Statistically the micro-porosities with

a diameter of less than 54 μm are not detected in Fig. 6.17a.

In Fig. 6.17a, the micro-porosity A (marked in red) is detected. However, it is not detected on the surface shown in Fig. 6.16a. It appears from the depth of 90 μm shown in Fig. 6.16b. Figure 6.16b shows the x-ray tomography image from the depth of 90 μm. The micro-porosity A has a diameter of 0.162 mm. The micro-porosity A can be detected more clearly in the raw image with contrast adjustment shown in Fig. 6.17b.

Figure 6.17c shows the infrared image from PCT. This image is from the 6th EOF. In Fig. 6.17c, the performance of the micro-porosity A is exceptional (darker in contrast) compared to the other micro-porosities. Micro-LLT can detect the micro-sized internal defects in the sample. However, the depth and the size of defects can affect the detection results.

Figure 6.16c shows the x-ray tomography image from the depth of 0.18 mm. The micro-porosity B (marked in blue) is inspected and has a diameter of 0.216 mm from the depth of 0.18 mm. However, the micro-porosity B cannot be inspected in the infrared images. One potential cause is that the depth of 0.18 mm exceeds the IR camera detection limitation with the laser beam power of 2.9 W. Another potential cause is that the micro-porosity B is below the fiber F (marked in orange) shown in Fig. 6.16a and Fig. 6.17a. It might reduce the heat transmission. This hypothesis was investigated using finite element analysis. [60]

6.4.2 Finite Element Modeling and Simulation

A finite element simulation was performed to analyze the micro-porosities A and B. A model was implemented into COMSOL Multiphysics as a user-defined material model for predicting the non-linear behavior of heat transmission in the sample. The model was validated for the experimental results. Finally a comparison of the experiments and simulation was conducted.

The geometrical model needed for finite element discretization was developed from the micro-CT measurements (Fig. 6.18). The laser-line power is 2.9 W. The power was tested in the lab. The power density is 2.9 W / (3 mm $\times$ 10 mm). The laser line covered an area of 2.5 mm $\times$ 0.5 mm. Therefore, the power in the model is 2.9 W $\times$ (2.5 mm $\times$ 0.5 mm) / (3 mm $\times$ 10 mm). The heating time is 0.5 s.

The material properties used for the model are shown in Table 6.2.

Table 6.2: The material properties

	Epoxy	Fiber	Porosity
Thermal conductivity (k)	0.2 W/(m·K)	$\{60, 4, 4\}$ W/(m·K)	0.004 W/(m·K)
Density (ρ)	1200 kg/m^3	1500 kg/m^3	0
Heat capacity (C$_\rho$)	1000 J/(kg·K)	1000 J/(kg·K)	1004.5 J/(kg·K)

Figure 6.19a shows the x-ray tomography measurements. Figure 6.19b shows the correspond-

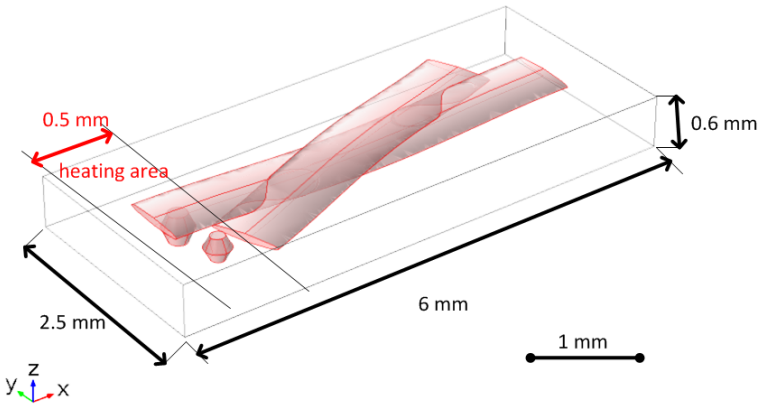

Figure 6.18: The geometrical model.

ing model geometrical parameters. The length of the fiber F is 5 mm, and its width is 0.8 mm. The length of the fiber G is 4 mm, and its width is 0.8 mm. The thickness of fiber F and G is 90 μm. The fill yarn cross section is an ellipse with major axis 0.8 mm and minor axis 0.09 mm. The warp yarn curves are described by Eq. (1), where h_y = 0.1 mm and a = 5 mm. Fiber G is rotated by 20°. Two concave surfaces face each other. The centers of mass lay on z-axis. Two fibers are embedded in cubic epoxy with the volumetric dimension of 6 mm × 2.5 mm × 0.6 mm laid along x-axis. In Fig. 6.19a, the micro-porosities A and B cannot be detected because they are below the surface. However, their positions are indicated.

The parameters of the micro-porosities A and B are shown in Fig. 6.19c. The parameters were obtained from the micro-CT. The micro-porosity A appears from the depth of 90 μm to the depth of 0.36 mm, and has a diameter of 0.162 mm to 0.306 mm. The micro-porosity B appears from the depth of 0.18 mm to the depth of 0.504 mm, and has a diameter of 0.216 mm to 0.36 mm.

Figure 6.20a shows the simulation surface temperature distribution from the heating time 0.5 s. Figure 6.20b shows the corresponding slice temperature distribution. Figure 6.20c shows the surface temperature distribution from top view.

Result analysis

Figure 6.21a shows the surface slice temperature distribution from top view. Figures 6.21b, 6.21c, 6.21d and 6.21d show the slice temperature distribution from the depth of 50 μm, 0.1 mm, 0.2 mm and 0.5 mm respectively. The temperature on the position of the micro-porosity A is much higher than that of the micro-porosity B, as shown in the figure. In Figs. 12 6.21a, 6.21b and 6.21c, the temperature on the position of the micro-porosity A is higher than that

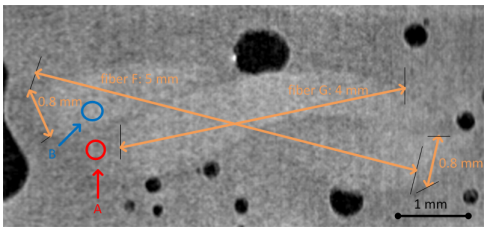

(a)

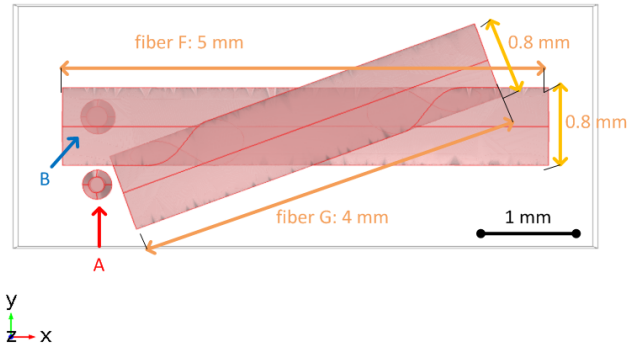

(b)

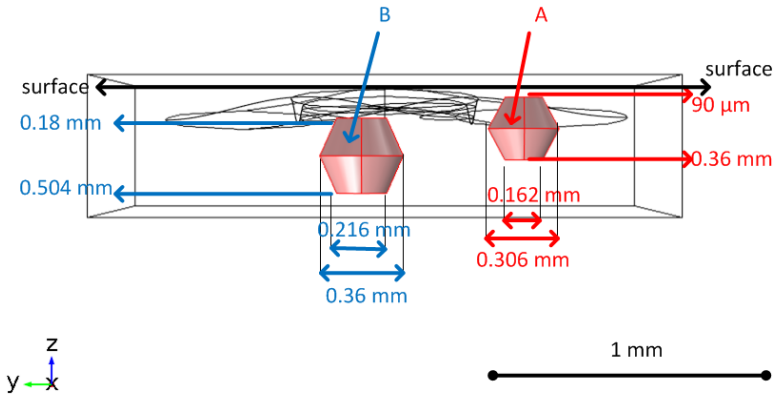

(c)

Figure 6.19: (a) The micro-CT measurements (surface), (b) the corresponding model geometrical parameters, (c) the geometrical parameters of the porosities A and B.

of the other heated zones. The potential cause is the influence of the micro-porosity A. In Fig. 6.21e, the temperature on the position H is higher than that of the other heated zones. The

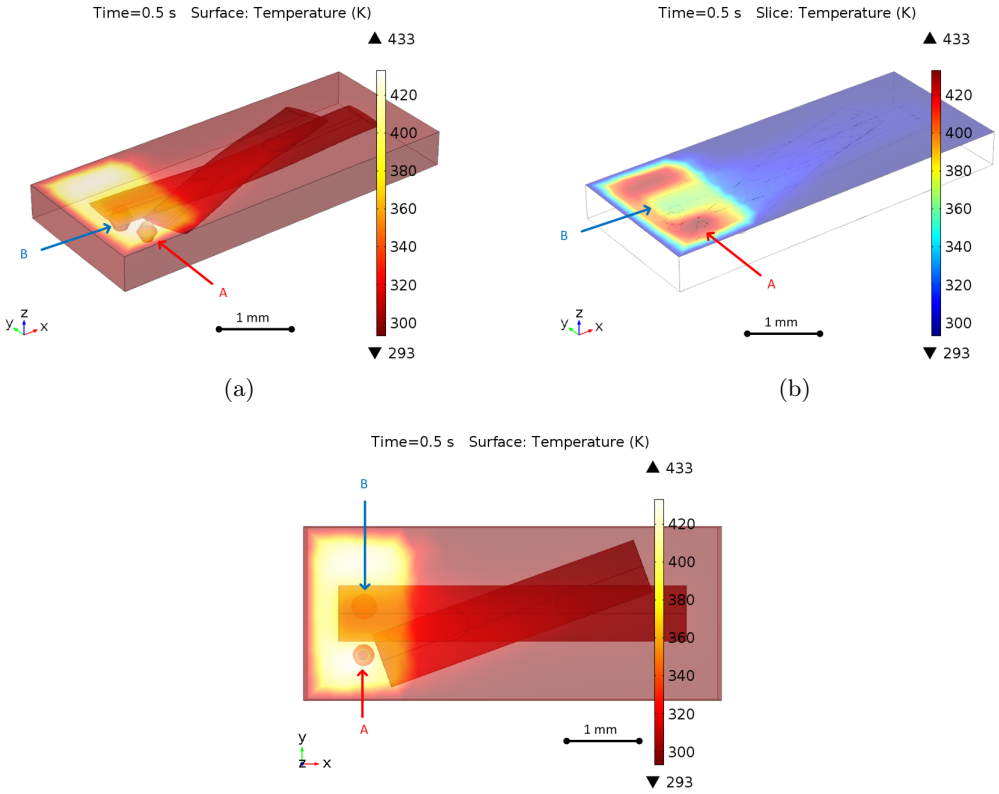

Figure 6.20: (a) surface temperature distribution (heating time: 0.5 s), (b) slice temperature distribution (heating time: 0.5 s), (c) surface temperature distribution from top view.

potential cause is that neither fiber nor micro-porosity is existed on the position H. Therefore, the heating transmission is not reduced.

Figure 6.22a indicates the cause of the phenomenon inspected from the micro-LLT experiments. The fiber F reduced the heat transmission towards the micro-porosity B. It is the major reason that the micro-porosity B was not detected in the infrared results, but was detected in the x-ray results.

Figure 6.22b shows the slice temperature distribution from side view when the heating time is 1 s. According to the temperature distribution compared to Fig. 6.22a, the micro-porosity B cannot be detected using micro-LLT even if the heating time is increased to 1 s.

The temperature distribution images can directly reveal the trend of the heating transmission. However, it cannot provide more reliable information for the detection capability. For comparative purposes, CIS and PCT were also used for simulation, which was previously poorly documented in the open literature.

The simulation data was exported to Matlab for further image processing, and the correspond-

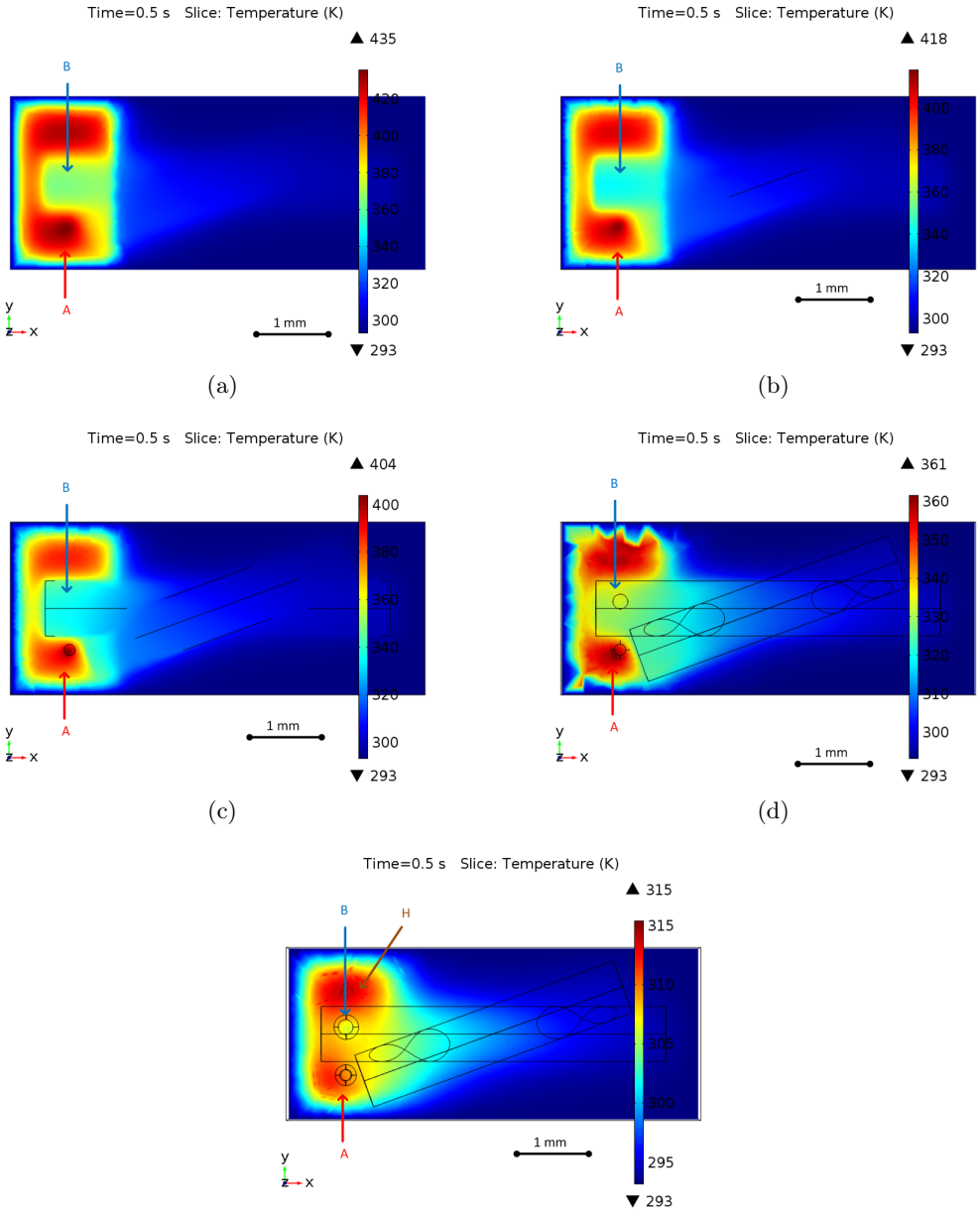

Figure 6.21: Slice temperature distribution from top view when the heating time is 0.5 s: (a) surface, (b) depth: 50 μm, (c) depth: 0.1 mm, (d) depth: 0.2 mm, (e) depth: 0.5 mm.

ing data structural transformation was performed.

Figure 6.23 shows the simulation images after image processing. The corresponding experimental results after image processing reveal the clearer porosity A than the simulation images. The porosity B cannot be inspected in the experimental results. However, it can be identified in Fig. 6.23b, which is the corresponding simulation image after PCT.

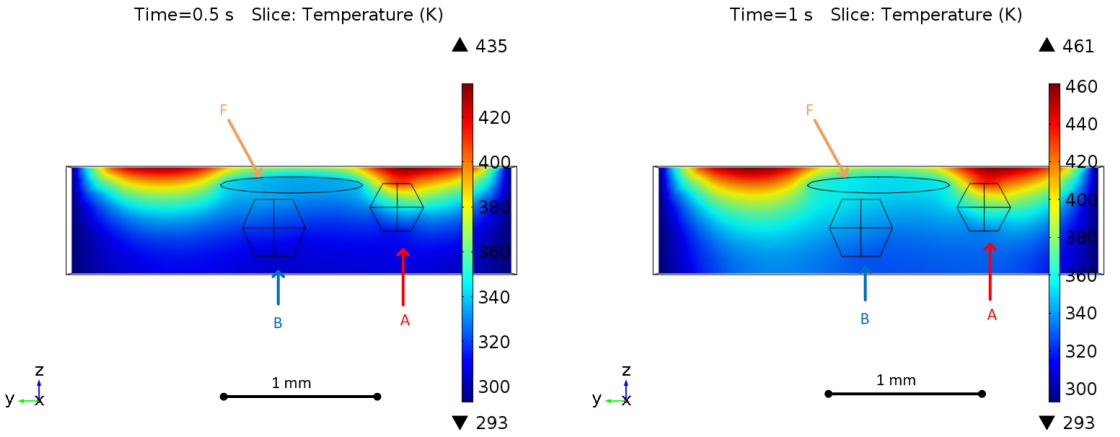

(a) (b)

Figure 6.22: Slice temperature distribution from side view: (a) heating time: 0.5 s, (b) heating time: 1 s.

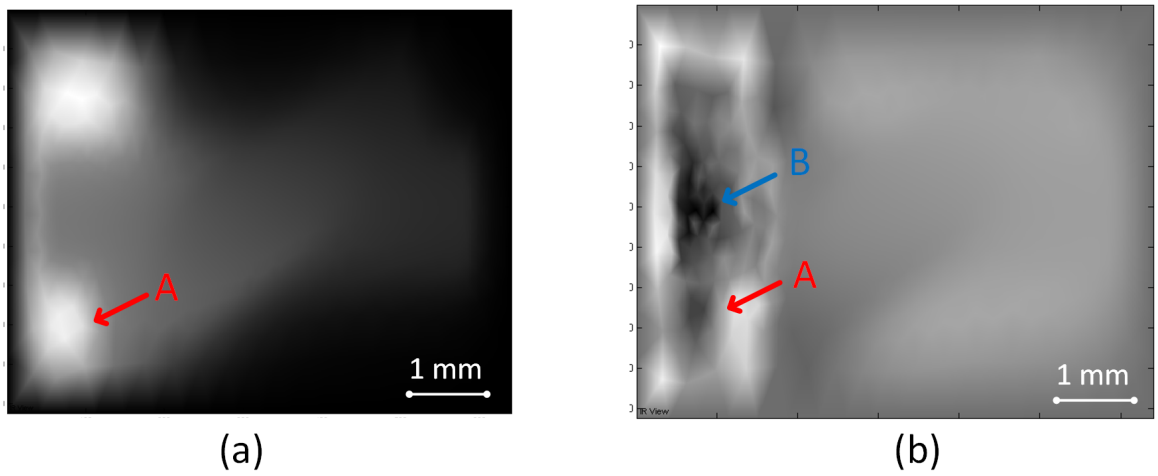

Figure 6.23: The simulation results after the corresponding image processing: (a) CIS, (b) PCT.

In Table 6.3, 1 means that the porosity is detected by the corresponding image processing technique, and 0 means the corresponding porosity is not detected. Table 6.3 reveals the detection capability. The minimum size is 54 μm, and the maximum depth is 0.18 mm.

The mesh of the corresponding models affects the image processing results severely, which is shown in Fig. 6.23. The simulation results in Fig. 6.23 reveal that clearer results can be obtained by PCT than CIS, but the defect size also affects the detection capability.

Table 6.3: Detection capacity of pulsed micro-LLT.

Submillimeter porosity		Experiment		Simulation	
Depth	Size	CIS	PCT	CIS	PCT
36 μm	72 μm	1	1	1	1
54 μm	54 μm	1	1	1	1
72 μm	126 μm	1	1	1	1
90 μm	108 μm	1	1	1	1
108 μm	90 μm	1	1	1	1
162 μm	72 μm	0	1	0	1
180 μm	216 μm	0	0	0	1

6.5 Lock-in Micro-LLT and Micro-LST

6.5.1 Experimental Configurations

The configuration for lock-in lock-in micro-LLT in this work is shown in Fig. 6.24. In the set-up, a galvanometer scanning mirror with a frequency of 600 Hz is used to generate the laser line. The position of the laser line can change by modulating the galvanometer scanning mirror, which is shown in Fig 6.24b. Therefore, the set-up can avoid blocking the camera's capture, which is more practical for submillimeter flaws detection. The laser line is approximately 13 mm in length, 3 mm in width, and its power is 0.6 W. A micro-lens with the magnification of 1× is mounted on an infrared camera for identifying and characterizing the submillimeter porosities. The mid-wave infrared camera 'FLIR Phoenix' at a frame rate of 55 fps (640 × 512 pixels) is used to record the temperature profile. A diode-laser with the wavelength of 805 nm is used as the heating source. A convex lens is used to focus the laser beam. A waveform generator is used to generate the laser line, and another waveform generator is used to generate the lock-in waves (sinusoidal waves). For pulsed micro-LLT, a 0.5 s pulse heating is performed. For lock-in micro-LLT, 1 Hz and 5 Hz lock-in signals heating (20 periods) is conducted on the same zone.

The set-up with the galvanometer scanning mirror is also used for micro-LST in this work, which is shown in Fig. 6.25. The position of the laser spot can change by modulating the mirror angle. A waveform generator is used to generate lock-in waves. The laser spot diameter is 3 mm, and its power is 0.22 W. For pulsed micro-LST, a 0.5 s pulse heating is performed. For lock-in micro-LST, 1 Hz lock-in signal heating (20 periods) is conducted on the same zone.

6.5.2 Result Analysis

Fig. 6.26 shows micro-CT slices from the position of 141 mm. Fig. 6.26a shows the surface of the detected region. Fig. 6.26b shows the micro-porosity A, which appears from the depth of 90 μm. The micro-porosity A has a diameter of 0.162 mm. Fig. 6.26c shows the micro-porosity B, which appears from the depth of 0.18 mm. The micro-porosity B has a diameter

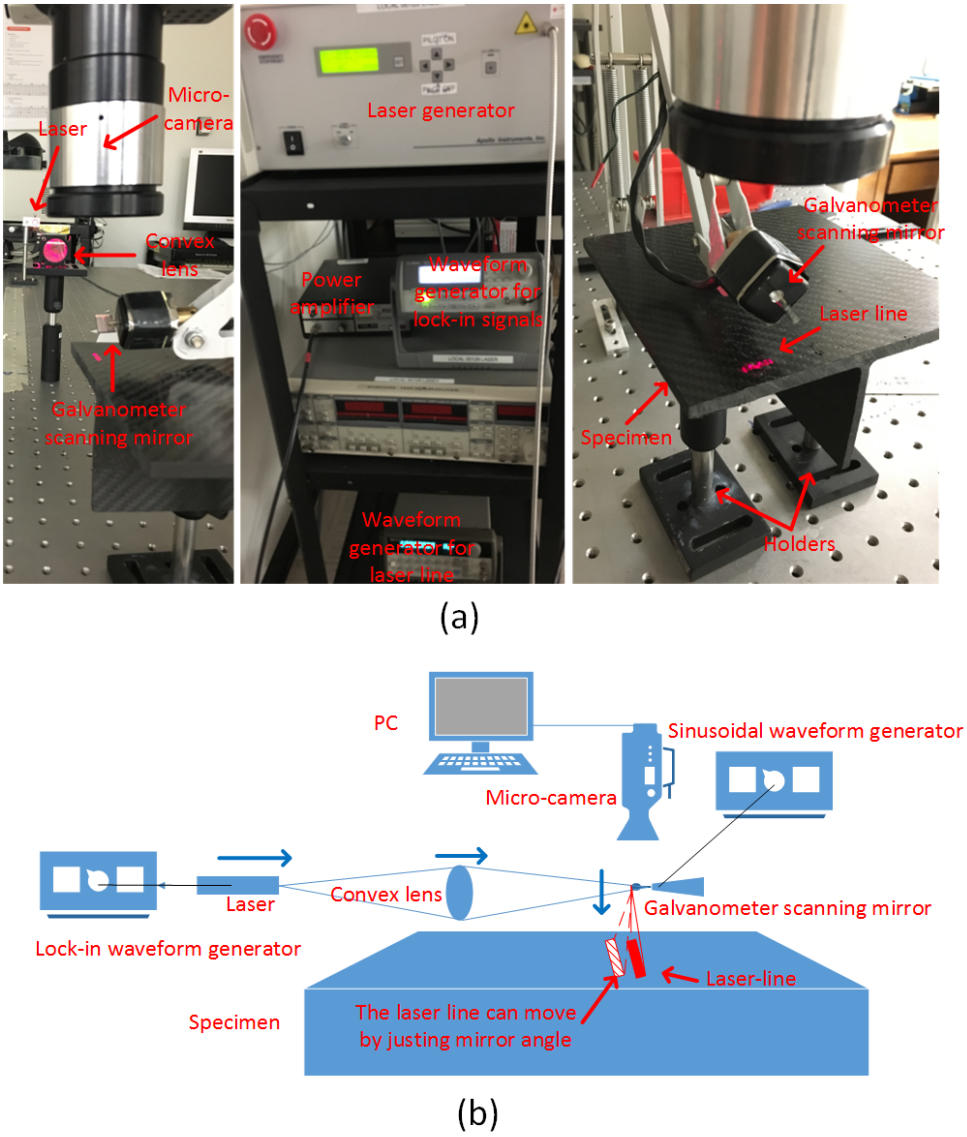

Figure 6.24: Lock-in micro-LLT set-up: (a) experimental set-up, (b) schematic set-up.

of 0.216 mm. Fig. 6.26d shows the micro-porosity C, which appears from the depth of 0.414 mm. The micro-porosity C also has a diameter of 90 μm

Fig. 6.27 shows the micro-LLT results. Fig. 6.27a shows the pulsed micro-LLT result after CIS when the heating source is a 0.5 s pulse. The micro-porosity A can be detected. In lock-in method, the micro-porosity B cannot be detected in the raw images as in the pulse method. However, the images after image processing can provide more defects information. Fig. 6.27b shows the lock-in result after PCT. The micro-porosity A can be detected in the image. The micro-porosity B is also detected, but not as clearly as the micro-porosity A. Figs. 6.27c and 6.27e show the lock-in results after Fourier transform (FT) on amplitude. The

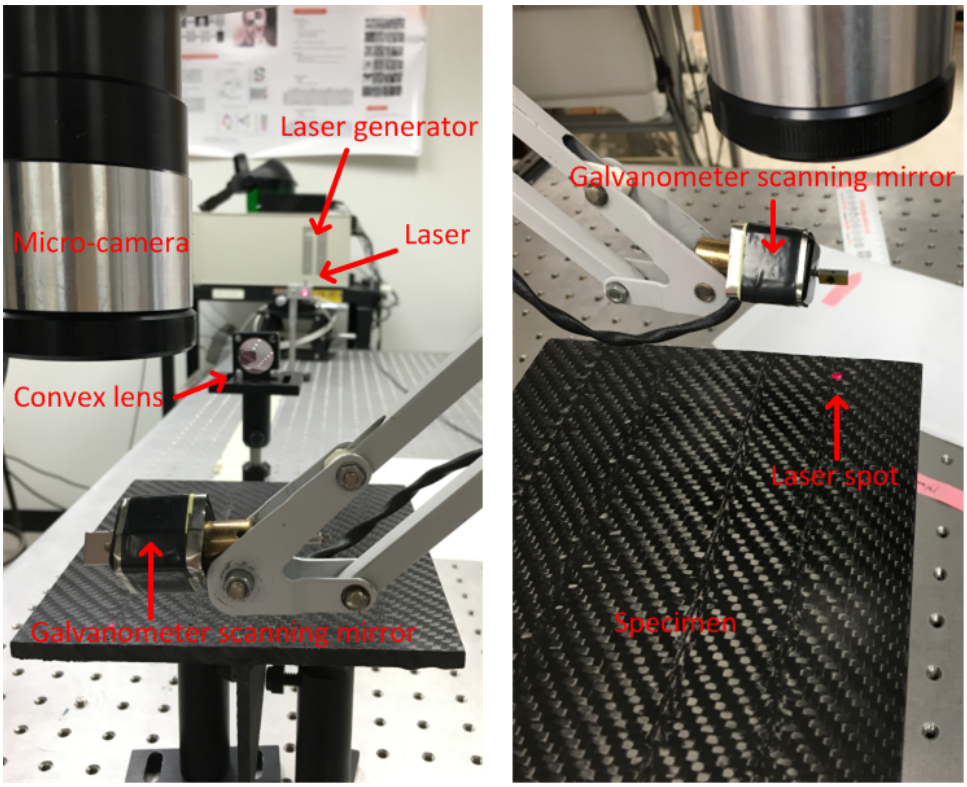

Figure 6.25: Micro-LST experimental set-up.

micro-porosities A and B can be detected, but not clearly. The micro-porosity A is clearer when the lock-in frequency is 1 Hz. On the contrary, the micro-porosity B is clearer when the lock-in frequency is 5 Hz. The positions of the micro-porosities A and B are correspondingly marked in Figs. 6.27d and 6.27f. Figs. 6.27g and 6.27h show the lock-in results after FT on phase. The micro-porosity A can be detected, but not clearly. The micro-porosity B cannot be detected as in the amplitude case.

Fig. 6.28 shows the micro-LST results. Fig. 6.28a shows the 0.5 s pulse laser heating result after CIS. The micro-porosity A is detected. The micro-porosity B cannot be inspected by any image processing methods, similar to the corresponding pulsed micro-LLT results. As in the lock-in micro-LLT results, the micro-porosity B cannot be detected in the raw images, but can be detected in post-processing images. Fig. 6.28b shows the lock-in result after PCT. The positions of the micro-porosity A and B are anomalous. One can conclude that the micro-porosities A and B are detected in this image. However, this result is not absolutely reliable. Fig. 6.28c shows the lock-in result after FT on amplitude. The micro-porosities A and B are detected clearly. The micro-porosity A is clearer than the micro-porosity B. Compared to the corresponding laser line method, the micro porosity B is clearer. Fig. 6.28d shows the lock-in result after FT on phase. Similar to the corresponding laser line results, the micro-porosity A

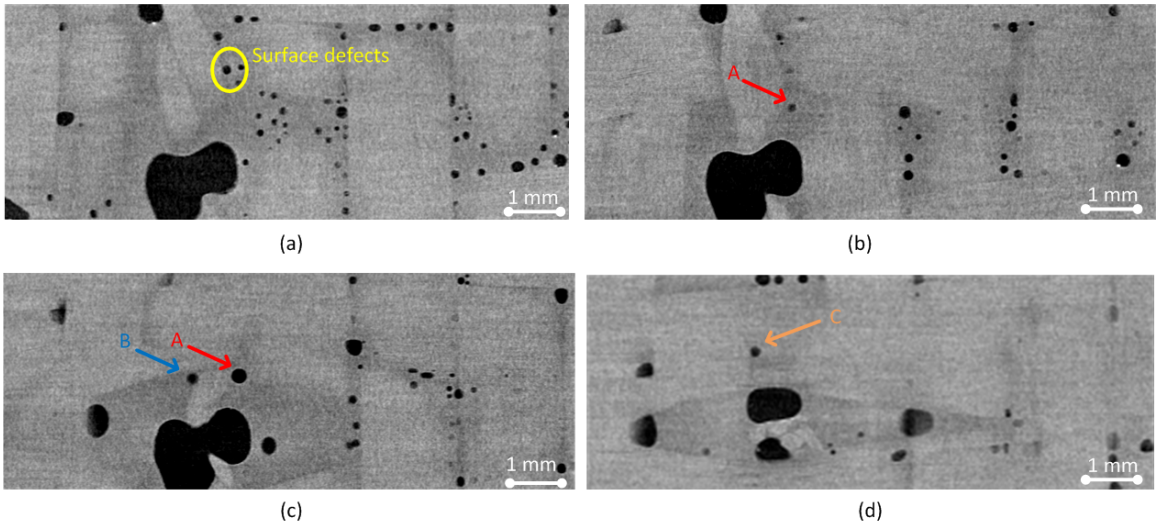

Figure 6.26: Micro-CT slices (a) surface, (b) depth: 90 μm, (c) depth: 0.18 mm, (d) depth: 0.414 mm.

can be detected, but not clearly. The micro-porosity B cannot be detected.

6.6 Micro-vibrothermoraphy (Micro-VT)

6.6.1 Experimental Configuration

In this work, micro-VT is proposed by using a 1× micro-lens, which is shown in Fig. 6.29. The IR camera 'Flir Phoenix' with the same configurations as laser thermography is used to record the temperature profile. In the set-up, an ultrasound excitation transducers with a pressure of 200 Pa is pressed against the specimen and a burst of ultrasound waves is delivered to the specimen. Table 6.4 shows the micro-VT generator technical specifications. A 10 s pulsed ultrasound excitation is used. The ultrasound excitation position is located on the back side of the specimen.

Table 6.4: Micro-VT generator technical specifications.

Technical specification	Explanation/value
Ultrasound frequency	20 kHz
Waveform	modulation or pulsed
Minimum modulation frequency	0.1 Hz
Maximum excitation time	10 s
Amplitude	0 to 100%

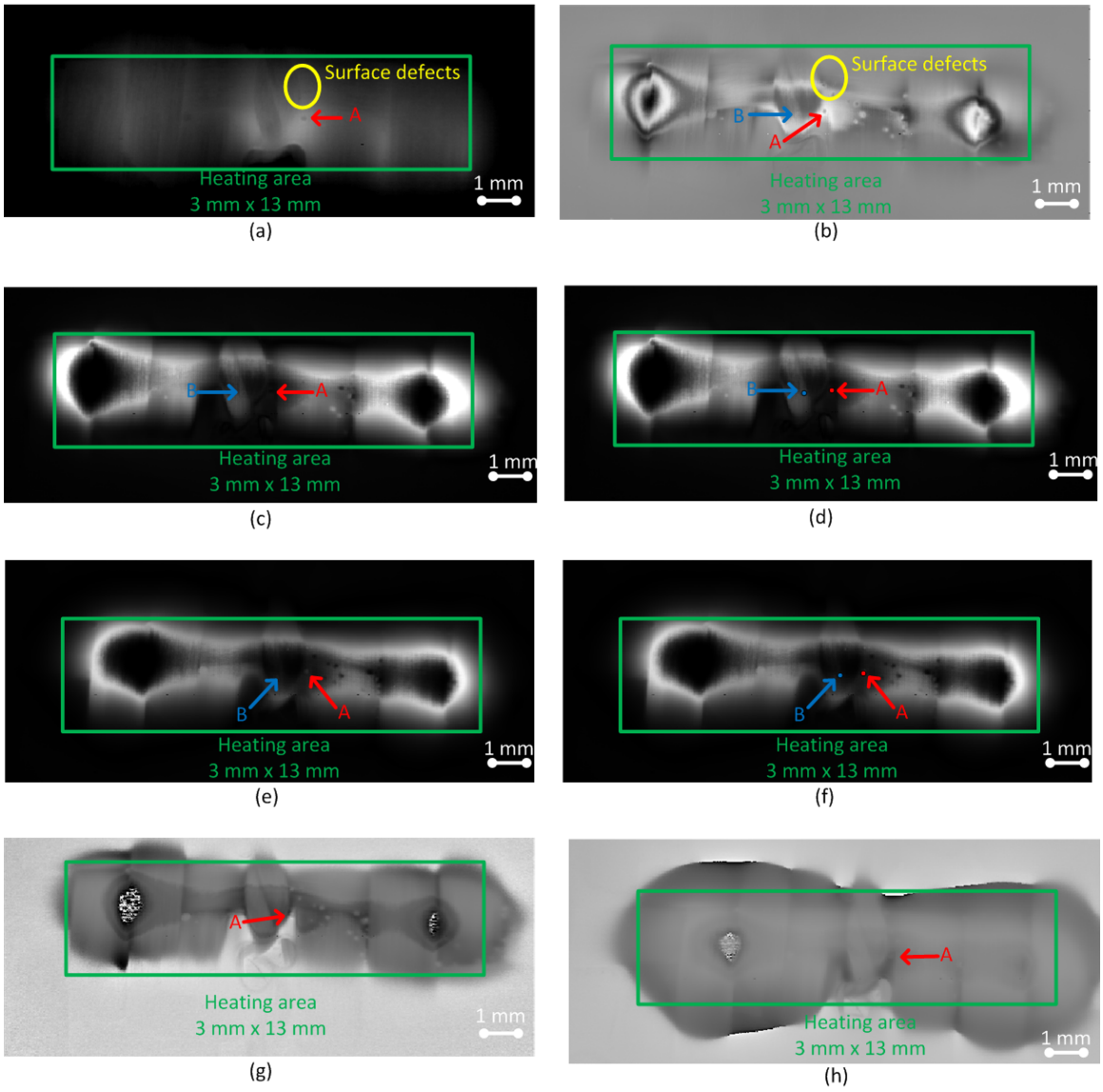

Figure 6.27: Micro-LLT results (a) pulse: 0.5 s, cold image, (b) lock-in: 5 Hz, PCT (EOF 8), (c) lock-in: 5 Hz, FT amplitude, (d) lock-in: 5 Hz, FT amplitude (defects marked) (e) lock-in: 1 Hz, FT amplitude, (f) lock-in: 1 Hz, FT amplitude (defects marked) (g) lock-in: 5 Hz, FT phase, (h) lock-in: 1 Hz, FT phase.

6.6.2 Result Analysis

Fig. 6.30 shows the corresponding micro-VT results. Fig. 6.30a shows the micro-VT result, which is from the raw images. The post-processing images do not provide better results. Compared to the micro-CT slices, micro-porosities on surface can be detected. The micro-porosities A, B and C can also be detected, but not clearly. The three micro-porosities are marked in Fig. 6.30b. The micro-porosities A, B and C show a similar size and shape, which is absolutely wrong.

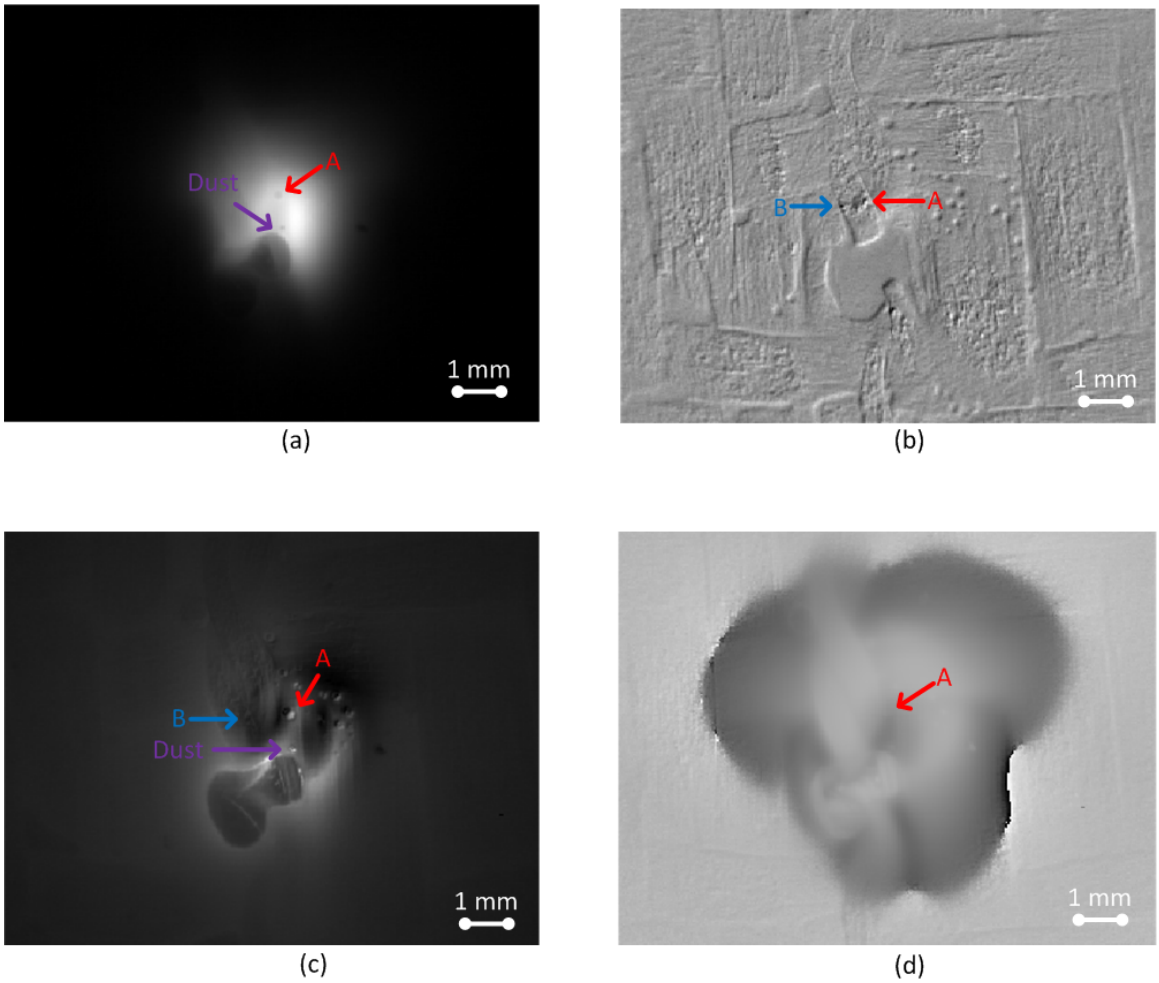

Figure 6.28: Micro-LST results (a) pulse: 0.5 s, cold image, (b) lock-in: 1 Hz, PCT (EOF 5), (c) lock-in: 1 Hz, FT amplitude, (d) lock-in: 1 Hz, FT phase.

Table 6.5: Experimental thermographic results.

Submillimeter porosity	Pulsed micro-LLT & LST			Lock-in micro-LLT & LST				Micro-VT
Depth	Raw image	CIS	PCT	Raw image	PCT	FT on phase	FT on amplitude	Raw image
Surface	1	1	1	1	1	1	1	1
90 μm	1	1	1	1	1	1	1	1
180 μm	0	0	0	0	1	0	1	1
414 μm	0	0	0	0	0	0	0	1

Table 6.5 shows the experimental thermographic results, where 1 indicates that the corresponding porosity is found, and 0 indicates that the corresponding porosity is not found. As a conclusion, lock-in technique can detect the deeper depth than pulsed technique. However, the clarity of the results decreases rapidly as the detection depth increases in PCT results. The amplitude FT results can provide more information than phase calculation. The FT results are not as clear as the CIS results, but CIS is not suitable for lock-in technique. The laser spot method is more powerful than the corresponding laser line method even if the laser spot power is lower compared to the laser line power. Micro-VT can detect the larger zone and deeper

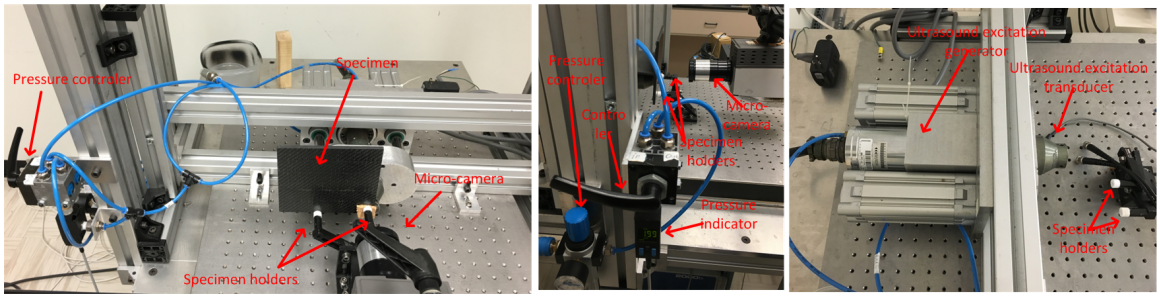

Figure 6.29: Micro-VT experimental set-up.

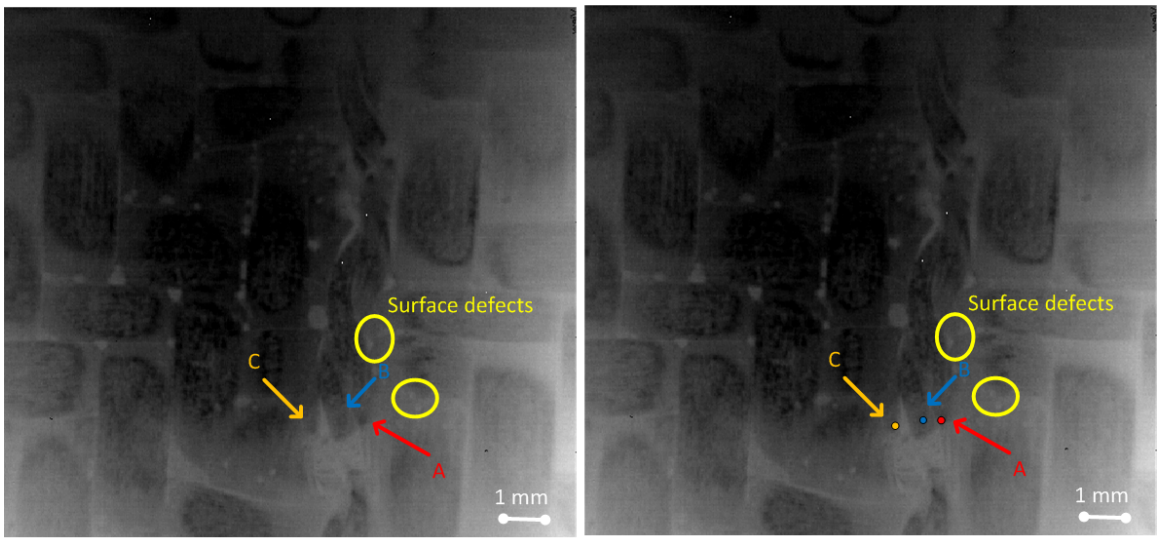

Figure 6.30: Micro-VT results (a) pulse: 10 s, (b) pulse: 10 s (defects marked).

depth than laser excitation thermography, but the detection size and shape informations are not accurate.

6.7 Summary

In this work, established techniques were used to detect a stitched 3D T-joint CFRP. Microscopic inspection can obtain the internal structure and submillimeter flaws in a clear manner. However, it is a time-consuming and destructive technique. UT cannot indentify and characterize the internal flaws accurately. PT can detect the large-sized flaws, but cannot detect the submillimeter flaws. VT cannot detect the internal flaws due to the complex structure. LST using lock-in method can detect the internal structure and flaws. However, it is a time-consuming technique.

A new micro-LLT was presented. Micro-CT was used to validate the micro-laser line thermography results. A comparison of micro-LLT and high-resolution x-ray tomography was conducted. Then a FEA was performed on the micro-LLT results. The geometrical model needed for finite element discretization was developed from micro-CT measurements. The comparison of the experiments and simulation was conducted. As a conclusion, micro-LLT can detect the micro-sized internal defects in the sample. However, the depth and the size of defects affect the detection results. Statistically the micro-porosities with a diameter of less than 54 μm cannot be detected in the micro-LLT results. Micro-LLT can detect the micro-porosity (a diameter of 0.162 mm) from the depth of 90 μm. However, it cannot detect the internal micro-porosity (a diameter of 0.216 mm) from the depth of 0.18 mm. The major cause is that the porosity with the diameter of 0.216 mm is below a fiber which reduced the heat transmission.

Other new IRT approaches including micro-VT, lock-in micro-LLT and micro-LST based on lock-in and pulsed techniques are proposed. These approaches are also used to detect the submillimeter porosities in the stitched T-joint CFRP specimen. Micro-CT is used to validate the thermographic results. Finally an experimental comparison of micro-laser excitation thermography and micro-ultrasonic excitation thermography is conducted. As a conclusion, micro-VT can provide the deepest detection depth, but the size and shape informations are not accurate. Lock-in technique can identify the deeper depth than pulsed technique. The laser spot method can provide clearer results than the laser line method, but is not practical due to the limitation of detection zone.

For laser excitation thermography, a potential way to enhance the maximum detection depth is to increase the laser power, but there is a risk that the CFRP specimen would be damaged. Another potential way is to use lower lock-in frequencies. A finite element method (FEM) is beneficial to the analysis of the lock-in technique [83], especially by using infrared image processing techniques [74].

Chapter 7

Non-destructive Investigation of Paintings on Canvas

7.1 Introduction

The use of THz technology has been magnificently described in a book recently published [107]. Among the various applications that are possible with THz, its use in the cultural heritage (CH) field is attracting increasing attention. Recently, different applications have been introduced in the scientific panorama by eminent research groups. In particular, the attention was focused on panel paintings, taking into account both the nature of the defects and the type of the materials which, usually, constitute them. In the authors' opinion, it is important to first briefly summarize the salient works already carried out in this research field for the sake of clarity for the reader and, secondly, to introduce the advantages that an integrated approach, *e.g.*, with IRT can produce in terms of additional information for comparison purposes.

In 2015, Kock Dandolo *et al.* applied THz - time domain imaging (TDI) for non-destructive visualization of a hidden painting and other subsurface composition layers of a seventeenth century panel painting belonging to the National Gallery of Denmark. Plan-type and cross-sectional scans achieved by THz have been compared with X-ray images, thus helping in the understanding of the advantages and disadvantages of the technique for art diagnostic purposes [108]. Simultaneously, Koch Dandolo *et al.* also explored and imaged subsurface features of panel paintings through gilded finishes with THz-TDI. Subsurface layers of three gilded panel paintings (two contemporary tempera panel replicas and one fourteenth-century icon) have been successfully imaged behind gold finishes with THz-TDI [109]. Instead, Abraham *et al.* revealed buried layer information such as a graphite handmade sketch covered by several layers of paint. In addition, taking advantage of the pulsed THz emission, the authors demonstrated that it was also possible to evaluate the variations of the painting thickness [110]. Labaune *et*

al. applied THz-TDI on papyrus texts, including images of hidden papyri. Inks for modern papyrus specimens were prepared using the historical binder, Arabic gum, and two common pigments used to write ancient texts, carbon black and red ochre. Temporal analysis of the signals provides the depths of the layers, and their frequency spectra give information about the inks [111]. Abraham and Fukunaga employed onsite THz radiation for the analysis of museum artifacts related to art conservation science. The authors used two complementary portable THz imaging devices which have been employed at the Tokyo National Museum (Japan) and at the Museum of Aquitaine (France). A Japanese panel screen, African fetish figures, and a nearly 3500-year-old sealed Egyptian jar were imaged with THz waves, revealing their internal structures [112]. In 2016, Fukunaga *et al.* applied THz pulsed TDI technique and near-infrared observation to investigate an oil painting on canvas by Pablo Picasso. The multilayer structure was clearly observed in a cross-sectional image by THz pulsed TDI, and particular Cubism style lines were revealed under newly painted areas by near-infrared imaging [113]. One year before, Picollo *et al.* probed two masterpieces by Giotto di Bondone and by Masaccio. Data acquired at a noninvasive level on panel paintings provided useful information on their internal structures. In addition, a first attempt in the understanding of the chemical composition of the artworks was scientifically validated [114]. The combination THz - chemical characterization was also implemented three years before by Trafela *et al.* In their paper, THz spectroscopy in the time domain was explored in combination with multivariate data analysis for quantitative determination of chemical and mechanical properties of historic paper, such as lignin content, tensile strength, and ash content. Using partial least squares (PLS) regression, it was shown that quantitative prediction of the material properties is possible, which indicates the potential of THz spectroscopy for chemical characterization of complex organic materials of natural origin [115]. A comparative study between ultraviolet, visible, infrared (by using the well-known PPT technique) and THz spectra was conducted in the same year by Bendada *et al.* [116]. The work was based on non-simultaneous multi-spectral inspections of a panel painting sample, using a set of detectors covering from the ultraviolet to the THz spectra. The THz technique provided more information regarding the wood support (rings), as well as an indication of a sub-superficial inclusion of foreign material. Another comparative study between shearography and THz imaging for evaluating a wooden panel painting was reported by Groves *et al.* in 2009 [117]. Gallerano *et al.* have investigated hidden paintings since 2008. The colleagues also calculated the refractive indexes of artwork materials, as well as the ability of distinguishing pigments via the THz technique [118].

The exponential growth in the use of THz applications in the NDT&E research field is due to the fact that the THz region (from 0.1 to 10 THz in terms of frequencies) is an area of convergence between the electronics and the photonics fields in the electromagnetic spectrum. Among the advantages that can be underlined regarding the THz radiation, it is possible to remember that it can penetrate through a wide variety of dielectric materials (*e.g.*, fabric, paper, plastic, leather, and wood), it is non-ionizing and has minimal effects on the human body

(as opposed to X-ray radiation), it demonstrates a very large absorption when meeting water aggregates or humid materials while it is highly reflected when it hits metal surfaces. Concerning the disadvantages with respect to, *e.g.*, near-infrared reflectography/transmittography technique [119], the detecting of THz signals is difficult because blackbody radiation at room temperatures is strong at THz frequencies. Another concern for THz imaging is the atmospheric transmission. The atmospheric attenuation of the THz domain is higher than in the other spectral regions, such as infrared and visible-light regions [120]. This requires that THz imaging should be short-range when compared to imaging in the other modalities. Another problem is the selection of appropriate optics in imaging systems. Generally, lenses are not used so widely in the THz regime because of lack of convenient materials and anti-reflection coatings functioning over a wide range of frequencies [121]. Difficulties in the construction of advanced lenses are associated with one of the most important limitations of THz systems, which is the measurement resolution. Despite the increasing number of pixels in cameras, THz solutions are as limited by the diffraction phenomenon as are any other imaging systems. An absolute upper performance limit linked to the laws of physics is controlled by the sensor size working f-number of the lens and the wavelength of light that passes through the lens [122]. In the diffraction-limited case, frequency determines resolution [123]. To improve the signal-to-noise ratio (SNR), THz images can be obtained by mechanically scanning the object – pixel by pixel – with the use of a coherent source. However, this solution may be applied only for static objects, and it is difficult to export the apparatus *in situ*.

In this work, the authors studied the ability of a CW THz source for the detection of the nature of different canvas supports beneath oil paintings. Since the canvas layers can sometimes be doubled and of different nature in the same painting, what is visible from the rear side does not correspond to the reality. It follows the definition of art forgery, *e.g.*, a process of creating a piece of art by copying an existing piece or by mimicking the style of another artist with the use of certain materials to falsely attribute and (or) date works of art [124]. Forgery recognition and attribution processes require a detailed knowledge of the history and the work of a particular artist, materials available at the time when the artwork was allegedly created, as well as the manner of creation used by the artists. At the same time, forgers continue to enhance their skills in mimicking styles, using old canvas as skins of a core made by a different product (which have the intent to reach the right thickness). To counteract this, art experts rely heavily on various scientific methods now available [125]. Explained above regarding the main disadvantages of the X-ray technique, the neutron activation is used less frequently than infrared in order to reveal details of composition hidden by the top layers of the painting under investigation. The primary reason for this is the necessity to use a nuclear reactor as the source of neutrons, which significantly limits the availability of the method because of cost and physical location of the reactor; another reason is the residual radioactivity of paintings [126]. Additional options may be the use of acoustic analysis [127] or ground penetrating radar technique [128]. However, acoustic analysis remains today somewhat exotic for the field

of analysis of art. The main limiting factors are the speed of raster scanning and difficulties with the fine tuning of the setup. Often the successful operation of the device requires that a qualified specialist be involved. The number of publications on this subject is relatively limited, and the scope of research mostly includes mural and panel paintings (not paintings on canvas) [129; 130; 131]. When using the ground penetrating radar technique, interpretation of radargrams is generally non-intuitive to the novice and, in the CH field, it is usually used for thick objects, such as mural paintings [132] or historical floors [133] and not for thin objects, such as paintings on canvas, due to the operation frequency. The use of IRT can be a valid choice in order to support the THz imaging in the artwork inspection and in the distinction between genuine or fake weaving in paintings on canvas. Indeed, it is a non-contact, non-intrusive and non-invasive method which permits a series of advanced post-processing operations to seeing the unseen [64; 134; 76], *e.g.*, canvas cuspings [135], underdrawings [136], covered signatures [137], sub-superficial defects [138] and repairs [139], wood analysis [140], the raising damp effect [141], inclusions of heterogeneous materials [66; 61], porosity [74; 83; 65] and fiber orientation [63]. In the present research work the authors demonstrate how the use of principal component thermography (PCT) [57] and partial least square thermography [55] techniques applied under flash thermography conditions can help to retrieve some important differences between a sample constructed following the art master rules and a fraudulent work of art, when the results are compared with the THz imaging observations.

7.2 Description of The Samples

The canvas prototypes used in this work were composed of hybrid textile supports, with different textile fibers. Once mounted on a wooden frame, the prototypes were painted using the original execution technique inherent to the painting selected as representative samples to be duplicated. The original artwork is an oil painting on canvas produced in 1871 by James Abbott McNeill Whistler, titled *Portrait of the Painter's Mother* (Fig. 7.1) [142; 143; 144; 145].

The scale drawings were, therefore, reproduced on two different hybrid fabric supports (Fig. 7.2). Regarding the preparation of the specimens, textile fibers which exhibit adequate mechanical characteristics for conservation purposes were selected. The weft-insertion usually recommended is 12 yarns (weft) : 12 yarns (warp) cm^2. The final dimensions of the specimens are 24 cm $\times$ 30 cm. The textile support of canvas A was made from hemp and nettle, while the textile support of canvas B was made from flax and juniper. The material of canvas A is close to that of the original artwork, while in painting B, the force used on the paint brush was almost double with respect to the painting B. The method to paint by pressing on the canvas through the paint brush is the opposite used by the art masters, in general.

Figure 7.1: “James Abbott McNeill Whistler, Arrangement in Grey and Black, No. 1: *Portrait of the Painter's Mother*, 1871, oil on canvas, 144.3 cm × 162.4 cm, Musée d'Orsay, Paris".

7.3 Experimental Configurations

7.3.1 CW THz

The system employed in this work utilizes IMPAct ionization Transit Time (IMPATT) diodes [146; 147; 148] to exploit 0.1 THz (sub-THz) CW imaging. The system consists of a detector (TeraSense Linear-1024), a robot (Fanuc LR Mate 200iD 7L), and a CW THz emitter (TeraSense TS 1603). The detector has a spectral range of 40 GHz - 0.7 THz and a frame rate of 8.2 fps. The pixel size of the detector is 1.5 mm × 1.5 mm, and the number of pixels is 1024 (256 × 4). The CW THz emitter has an optimized frequency of 0.1 THz and 1 μs rise/fall time (TTL Modulation). The emitted radiation beam is expanded to exploit the detector ability of detecting radiation along a line composed of 256 pixels, which reduces scanning time. The imaging capability of the system is 6 mm (4 pixels) in width and 384 mm (256 pixels) in height. The central region of the detected images (5 mm in width) was selected as the step scanning resolution, and the sample moving speed was set to 5 mm/s. The distance between the sample and the THz emitter was ∼10 cm, which was the same as the distance between the sample and the THz sensor. Fig 7.3a and 7.3c show the reflection mode configuration, in which the CW source and the detector were placed in front of the painting layer. Fig 7.3b and 7.3d show the transmission mode configuration, in which the specimen was placed between

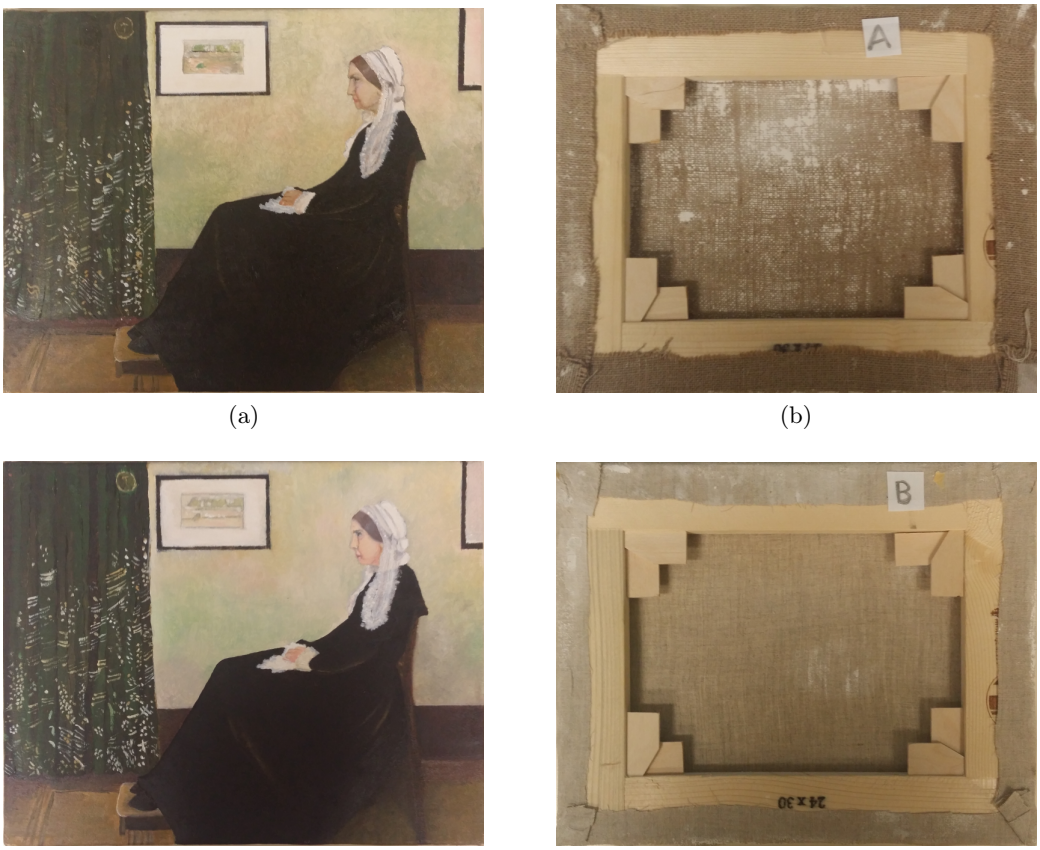

(a) (b)

(c) (d)

Figure 7.2: The photographs of the paintings on canvas: (a) the canvas A, (b) the canvas B, (c) the textile support made from hemp and nettle, (d) the textile support made from flax and juniper.

the CW source and the detector.

7.3.2 Flash Thermography

In this chapter, flash thermography was used to integrate the CW THz results.

Fig. 7.4 shows the schematic and experimental set-up for PT in which both a Balcar FX 60 (6.4 KJ, 2 ms duration) photographic flash and a mid-wave IR camera (FLIR Phoenix, InSb, 3 -5 μm, 640 $\times$ 512 pixels) was used. The cooling time was equal to $\sim$3 s (300 frames) and a frame rate of $\sim$88 fps was selected by considering the thickness of the material to be inspected. In particular, only one flash was used in order to minimize the effect of an overheating on the paint surface which is a concern for any restorer. Although this procedure can create a non-uniform heating on the surface, this effect can be minimized by applying advanced algorithms to the raw data as explained in the following.

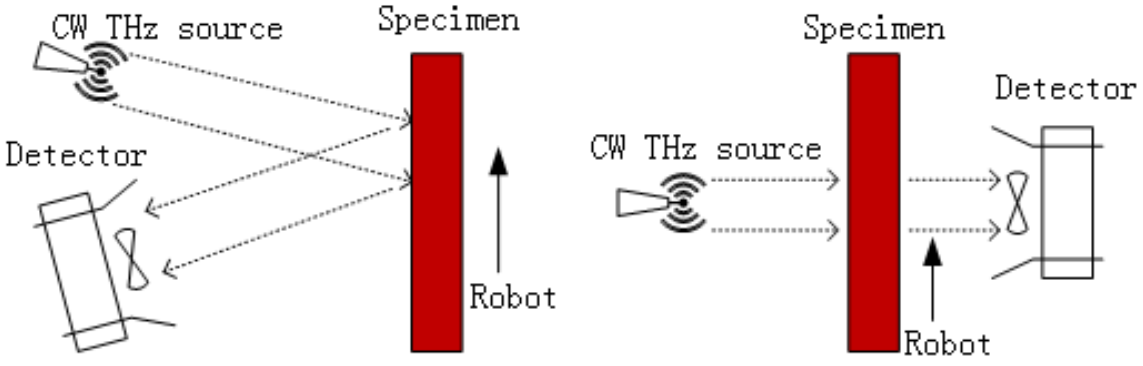

(a) (b)

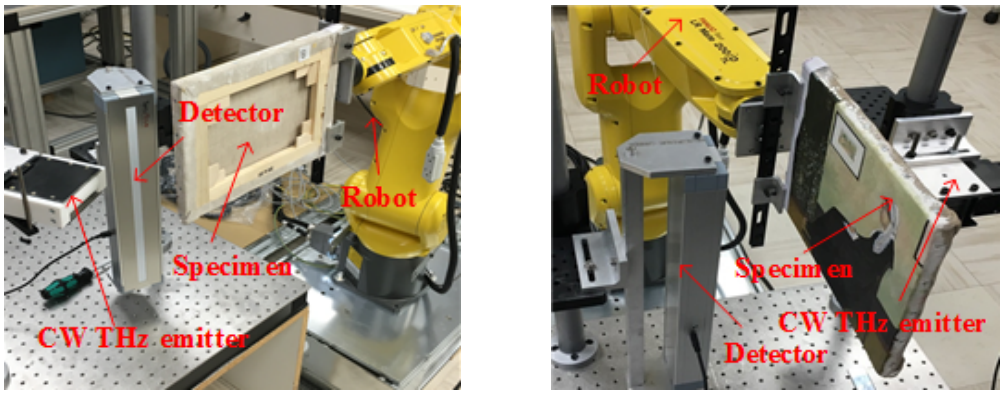

(c) (d)

Figure 7.3: CW sub-THz imaging system: (a) schematic set-up in reflection mode, (b) schematic set-up in transmission mode, (c) experimental set-up in reflection mode, (d) experimental set-up in transmission mode.

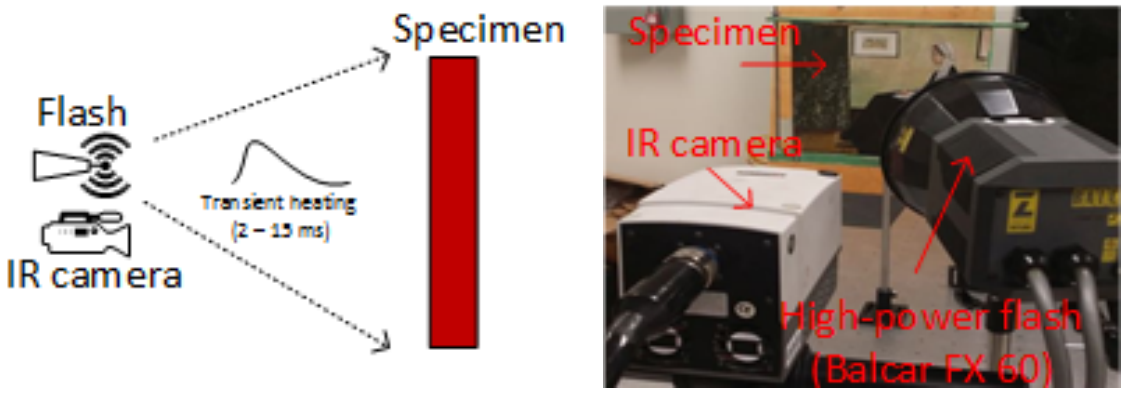

(a) (b)

Figure 7.4: PT set-up using flash: (a) schematic set-up, (b) experimental set-up.

7.4 Result Analysis

In this chapter, contrast optimization and median filter were performed in CW THz imaging, while RMF and CIS were performed prior to the application of PCT and PLST techniques to the raw thermograms.

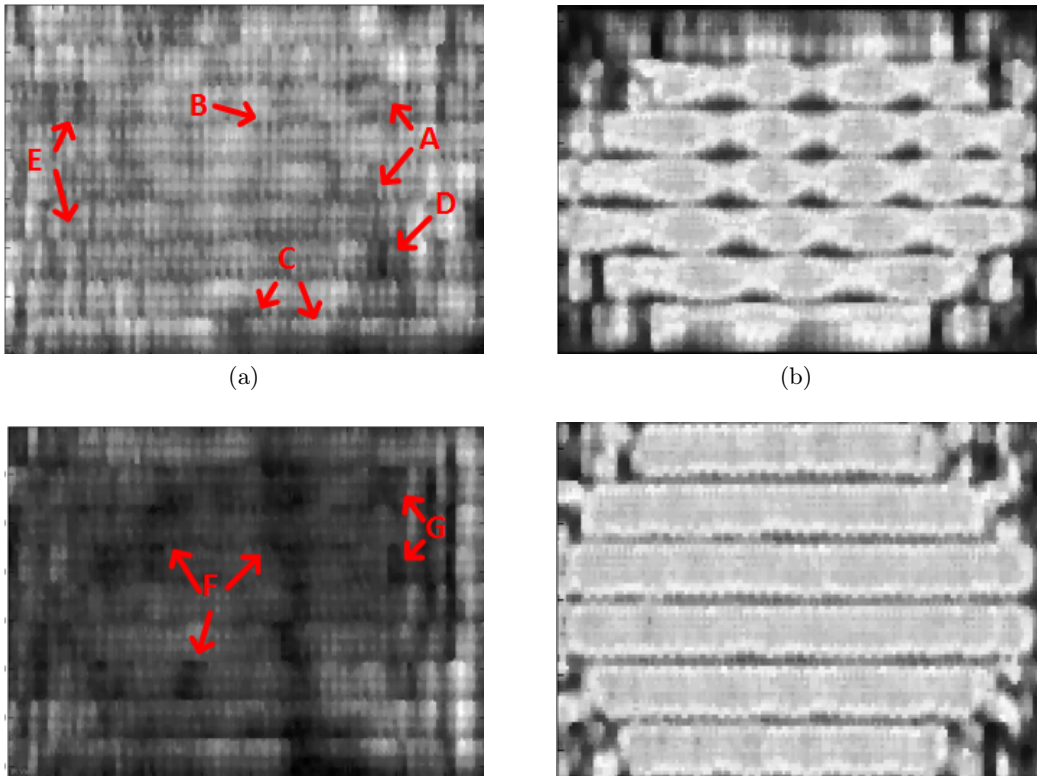

(a) (b)

(c) (d)

Figure 7.5: CW THz results: (a) painting on canvas A in reflection mode, (b) canvas A in transmission mode, (c) painting on canvas B in reflection mode, (d) canvas B in transmission mode.

Fig. 7.5 shows the CW THz results. In order to record the data, the robot was used to move the specimen, continuously and horizontally, with the aim of acquiring a series of narrow images. The images recorded by the sensor, with a size of 5 mm in width, were used to compose a wide image. Because the samples have a large size in height with respect to potentiality of the system, several scans were carried out along horizontal lines to build the final THz image. The image processing was performed using Python and Matlab scripts.

In reflection mode (Figs. 7.5a and 7.5c), some anomalous signals can be distinguished. They are indicated by arrows and explained in-depth in the following, while in transmission mode (Figs. 7.5b and 7.5d), the results show a periodic trend which is correlated to the wavelength of the radiation. The crossed fibers of the canvas can act as a reflective mesh, thus causing interference patterns depending on the different path length from source to detector. The

canvas A (Fig. 7.5a) indicates a more significant reflectance for THz radiation than the canvas B (Fig. 7.5c). On the contrary, the canvas B (Fig. 7.5d) manifests a more significant absorbency for THz radiation than the canvas A (Fig. 7.5b). These opposite phenomena were caused by the intrinsic characteristics of the supports, which have different absorptivities and reflectivities. In particular, the textile support made from hemp and nettle shows a configuration of spots alternating with high-absorption areas at specific frequency. Instead, the textile support made from flax and juniper displayed a more homogeneous behavior along the inspected lines. It should be noted that the thickness of the canvas supports (Figs. 7.2b and 7.2d) is the same, although in forgery the rear side may not match with the real support. In practice, a visual inspection or a simple microscope may not be enough in order to discriminate between a real object or a copy. The results shown herein are greatly significant for distinguishing various materials of similar (but not identical) nature. On one hand, it is obvious that the painted surface does not contribute solely to the discrimination between similar (but not identical) objects. On the other hand, this method could be potentially combined with the classical chemical analyses performed on cross-sections after a micro-sampling procedure [149; 137; 141] in order to discriminate between real or fraudulent artworks. The integration of methods proposed herein, at least when used in reflection mode, is also suited for *in situ* inspections if a movement off site, *e.g.*, the museum, is not admissible for microclimatic problems.

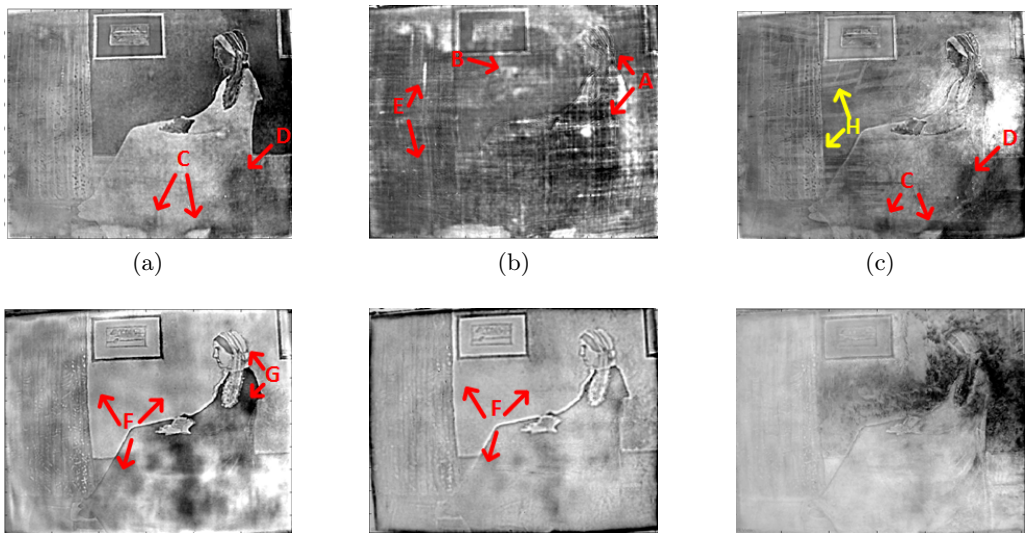

(a) (b) (c)

(d) (e) (f)

Figure 7.6: PCT results: (a) painting A: EOF 02, (b) painting A: EOF 03, (c) painting A: EOF 04, (d) painting B: EOF 02, (e) painting B: EOF 03, (f) paint B: EOF 04.

As mentioned above, some signals not correlated between the paintings can be retrieved. In particular, it seems that a vertical (dark) stripe can be visualized in the canvas B (defect F - on the right). It can be linked to the force used on the paint brush which closed more of

the pores between two consecutive fibers. Flash thermography was used to integrate the THz results. Specifically, a part of the features of the woman on painting A was detected. The features A indicate her head and arm in both THz and PCT results. An anomalous signal is marked by the letter B. It is detected more clearly in Fig. 7.6b. Additional irregularities in the signal variation are present near the feet of the woman as indicated by the letter C in Fig. 7.5a. They were also detected in Figs. 7.6a and 7.6c. The defect D was also clearly detected both in the THz (Fig. 7.5a) and PCT results (Fig. 7.6c), while the defect E indicates a poor fiber impregnation problem (Figs. 7.5a and 7.6b). These anomalies are not detectable to the naked eye and can be verified by the PCT technique. Interestingly, the warp and weft of the fibers are partially visible after the PCT image processing in Fig. 7.6c (see the anomaly H indicated by arrows). The latter is not detectable in the same EOF (EOF 04) shown in Fig. 7.6f, and inherent to the canvas B.

In the THz result (Fig. 7.5c) linked to the painting on canvas B, the hidden defect F was clearly detected. The same defect was also detected in PCT results shown in Figs. 7.6d and 7.6e. The letter G indicates another signal variation partially located on the head of the woman. This may suggest the presence of a hidden defect corresponding to the position of the woman's head, which may be located at a deeper depth. A longer cooling time during the IRT inspection may contribute to detecting this defect, which presumably is inherent to a thicker point of plaster applied beneath the paint layer (Figs. 7.2b and 7.2d).

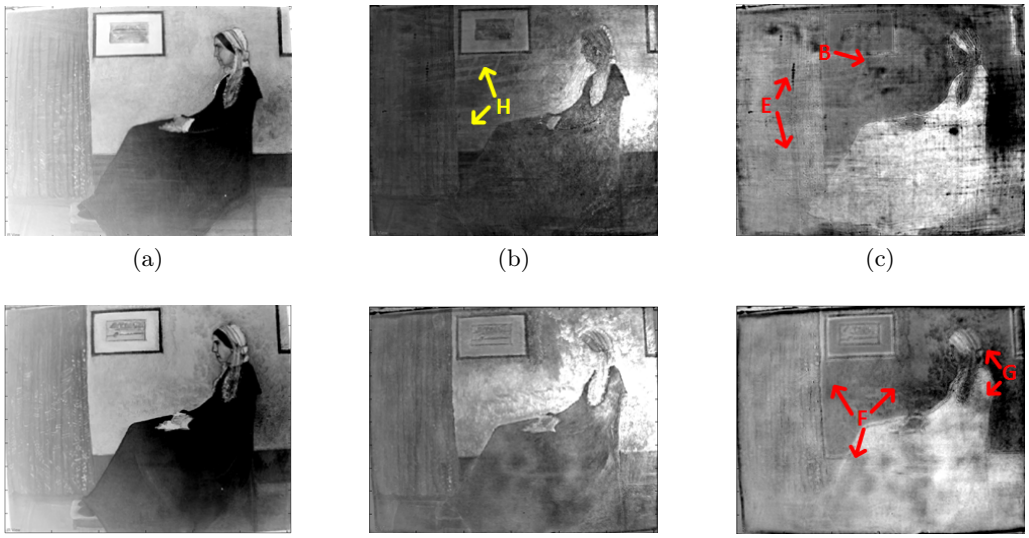

(a) (b) (c)

(d) (e) (f)

Figure 7.7: PLST results: (a) painting A: Loading 01, (b) painting A: Loading 02, (c) painting A: Loading 03, (d) painting B: Loading 01, (e) painting B: Loading 02, (f) paint B: Loading 03.

Flash thermography is able to provide information concerning the defect depth as studied in [150]. However, the series of the PLST results in Fig. 7.7, i.e., from Loading 01 to Loading 03

show the images through the increase of depth sounded, in both cases. PLST detected fewer anomalies with respect to the THz and PCT techniques. The signal variation H shows the alignment of the fibers. (Fig. 7.7b). This may explain the reason why it cannot be detected by THz. In fact, the limit imposed by the wavelength (0.1 THz) plays an important role. On the contrary, the defects B and E were detected at deeper depths as shown in Fig. 7.7c. The defect F which appears as a vertical stripe on the right side, was confirmed also in this case. It is indeed present in the THz result (Fig. 7.3c) and in the PCT result (Fig. 7.6d).

THz and IRT results indicate different sub-superficial anomalies which can be used to discriminate regarding the technical execution, and the modality of application of the materials. Interestingly, in PLST image processing, the Loading 02 in both cases (Figs. 7.7b and 7.7e) isolates the non-homogeneous heating provided by the right lamp (Fig. 7.4b) into itself. The reader can notice the bright area on the body of the woman. Both the PCT and PLST techniques were not able to retrieve the direction of the fibers for the canvas B. This is an important clue in order to provide a first conclusion concerning the technical execution of two similar (but not identical) samples.

7.5 Summary

In this work, CW THz (0.1 THz) imaging applied both in reflection and in transmission mode was applied to two similar (but not identical) paintings on canvas. In particular, the first one (named sample A) reproduces exactly the famous artwork (an oil on canvas) of James Abbott McNeill Whistler, titled *Arrangement in Grey and Black, No. 1: Portrait of the Painter's Mother*, completed in 1871, while the second one is a good reproduction in which the nature and the texture of the canvas is very dissimilar with respect to the real one and the technical execution is slightly different. Although the nature and the texture of the canvas can be observed from the rear side, one usually finds good reproductions in which the support is achieved with a bottom layer acting as a cover for the upper layers. Therefore, the inspection in reflection mode is important. In this case, the samples were prepared considering an identical final thickness, if compared to each other. The application of a cover layer on the rear side of sample B, identical to the canvas of sample A, improves the validity of the present method since also the transmission mode has been taken into account during the THz inspections. The polarization of the THz source used herein was also used in [151]. It was *a priori* considered, since anisotropic materials such as composites have a variable reflectance strictly connected to the fiber directions.

In real objects, the micro-sampling procedure and, therefore, the study of cross-sections can be considered as a second step to distinguish between artworks and forgeries. However, the micro-sampling procedure is, unfortunately, both micro-destructive and irreversible. Maybe the parameterization and analysis of various materials or the determination of the thickness

influence on the THz and IRT results, can be considered a valid alternative. The micro-sampling procedure is obviously not applied on reproductions/copies of real artworks, and/or when the materials used in real artworks are well known/documented. It can be combined with imaging in order to discriminate between materials and/or attend to "determine a period of time" of execution for an object, by considering the palette of pigments used by the art master (or by the forger). In addition, the use of the THz method combined with the use of the IRT method can help to provide information regarding the execution of the paint layers or the texture of the fabric used.

The THz results obtained in the transmission mode show different absorptivities for the textile supports, while thermographic results revealed both shallow and relatively deep anomalies in relation to the EOF (for PCT technique) or loading (for PLST technique) used. The PCT technique and THz method detect different signal variations. These signals variations can be attributed to sub-superficial anomalies than what it was possible to detect by the PLST technique. However, the PLST technique summarizes the most important noise linked to the use of a single lamp in the Loading 02. In addition, the consecutive images are strictly linked to the scanning of the depth. THz results are not immediately understandable to a non-expert in this matter, although when integrated with IRT results they can corroborate the main assumptions.

Although the THz is not new and the system used herein is a commercial product, the innovation is the use of the robot to scan the oil paintings, or more in general, the use of the robot in the cultural heritage field. It allows an *in situ* inspection when, e.g., it is not possible to move the artwork outside the museum due to microclimatic reasons. Our CW THz system has the advantage of operating via a simple experimental set up and is inexpensive, however, it cannot retrieve the defect depth. On the contrary, pulse THz system can assure quantitative analyses. Regarding the image processing, the intensity data are stored in a matrix in the CW THz system, which can be directly converted to a raster image. A perspective of the present work will be the use of the robot in combination with thermographic measurements, as well as the application of a pseudo-static reconstruction algorithm before the advanced image processing procedure. A short-wave IR camera (SWIR) can also be used both in reflection and in transmission modes considering both the semi-transparent nature of the object itself, and the possibility to perform a digital subtraction procedure between the reflectogram and the transmittogram with the aim of detecting the weaker areas of the canvas [78].

Conclusion

The thesis shows the performance of different NDT&E techniques for different composite materials including dry carbon fiber preforms, natural fiber composites, basalt-carbon hybrid composites, micro-sized flaws in a stitched T-joint CFRP and paintings on canvas which can be considered as composite materials.

In the cases of dry preforms, natural fiber composites and basalt-carbon hybrid fiber composites, IRT shows the clearest results among all the techniques. B-TSR and PCT show the clearest results among all the infrared image processing techniques. However, the lack of depth information is a disadvantage of PCT. Instead, PPT can provide the depth information. PLST can also show additional results as the depth increases, but not as clearly as PPT. PLST can only provide qualitative depth information, but it requires less processing time than PPT. The flashes modality can detect shallow-defects because it can reach a higher frequency. On the contrary, the halogen lamps modality is better for deep-defects detection.

A new IRT technique micro-LLT was proposed for the detection of micro-sized flaws in a stitched T-joint CFRP. This technique was validated by micro-CT for the detection of sub-millimeter porosities. A FEA was used to investigate the experimental phenomena. The same image processing techniques were performed both on the experimental and simulation date. In this way, micro-LST and micro-VT were also presented to detect these millimeter porosities. Finally, a comprehensive comparison of these new techniques was conducted to show their performance.

In the last chapter, a comparative study on paintings on canvas was conducted using CW THz and flash thermography. The canvas material can also be considered as composite materials. CW THz can detect subsurface features and its results were validated by the thermographic images.

More detailed conclusions are summarized in the 'summary' section of Chapter 3 to Chapter 5. Overall, IRT is a technique which is increasingly used, since it has the advantages of clearer images, faster detection speed and lower expenses. The thesis could contribute to the corresponding academic and industrial applications for the field of composite materials.

Future work

The following further work will be conducted to enhance the scientific contributions to this thesis in the future. 1), FEA will be preformed for the basalt-carbon hybrid composites in Chapter 5. This will be helpful to understand the IRT results and the structural advancements of different hybridization [73]. 2), Chirp modality can usually provide better imaging performance than LT [152]. This method will be used for the composite specimens in Chapters 4 and 5. 3), A robotic micro-LLT will be developed for the purpose of fast detection. For this purpose, a further study on dynamic thermography will be needed.

Appendix A

List of contributions

Published peer-review journal papers

[1] H. Zhang*, S. Sfarra, K. Saluja, J. Peeters, J. Fleuret, Y. Duan, H. Fernandes, C. Ibarra-Castanedo, X. Maldague, 'Non-destructive investigation of paintings on canvas by continuous wave terahertz imaging and flash thermography', Journal of Nondestructive Evaluation (2017) 36(2): 34. [DOI: 10.1007/s10921-017-0414-8]

[2] H. Zhang*, H. Fernandes, U. Hassler, C. Ibarra-Castanedo, M. Genest, F. Robitaille, S. Joncas, X. Maldague, 'Comparative study of microlaser excitation thermography and microultrasonic excitation thermography on submillimeter porosity in carbon fiber reinforced polymer composites', Optical Engineering (2017) 56(4): 041304. [DOI: 10.1117/1.OE.56.4.041304]

[3] H. Zhang*, H. Fernandes, F. Dizeu, U. Hassler, J. Fleuret, M. Genest, C. Ibarra-Castanedo, F. Robitaille, S. Joncas, X. Maldague, 'Pulsed micro-laser line thermography on submillimeter porosity in carbon fiber reinforced polymer composites: experimental and numerical analyses for the capability of detection', Applied Optics (2016) 55(34): D1-D10. [DOI: 10.1364/AO.55.0000D1]

[4] H. Zhang*, L. Yu, U. Hassler, H. Fernandes, M. Genest, F. Robitaille, S. Joncas, W. Holub, Y. Sheng, X. Maldague, 'An experimental and analytical study of micro-laser line thermography on micro-sized flaws in stitched carbon fiber reinforced polymer composites', Composites Science and Technology (2016) 126: 17-26. [DOI: 10.1016/j.compscitech.2016.02.007]

[5] H. Zhang*, U. Hassler, M. Genest, H. Fernandes, F. Robitaille, C. Ibarra-Castanedo, S. Joncas, X. Maldague, 'Comparative study on submillimeter flaws in stitched T-joint carbon fiber reinforced polymer by infrared thermography, microcomputed tomography, ultrasonic c-scan and microscopic inspection', Optical Engineering (2015) 54(10): 104109. [DOI: 10.1117/1.OE.54.10.104109]

[6] B. Liu, H. Zhang*(co-first author), H. Fernandes, X. Maldague, Experimental evaluation of

pulsed thermography, lock-in thermography and vibrothermography on foreign object defect (FOD) in CFRP', Sensors (2016) 16(5): 743. [DOI: 10.3390/s16050743]. Correction: Sensors (2017) 17(1): 195. [DOI:10.3390/s17010195]

Submitted peer-review journal papers

[1] H. Zhang*, S. Sfarra, F. Sarasini, S. Perilli, H. Fernandes, Y. Duan, J. Peeters, N.P. Avdelidis, C. Ibarra-Castanedo, X. Maldague, 'Optical and Mechanical Excitation Thermography for Impact Response in Basalt-Carbon Hybrid Fiber-Reinforced Composite Laminates', submitted to IEEE Transactions on Industrial Informatics.

[2] H. Zhang*, F. Robitaille*, C. Ibarra-Castanedo, J.O. Martins, S. Sfarra, X. Maldague, 'Optical excitation thermography for twill/plain weaves and stitched fabric dry carbon fiber preform characterization', submitted to Composites Part B: Engineering.

[3] H. Zhang*, S. Sfarra, F. Sarasini, S. Perilli, H. Fernandes, Y. Duan, J. Peeters, N.P. Avdelidis, C. Ibarra-Castanedo, X. Maldague, 'Non-destructive diagnosis and characterization of natural fiber-reinforced polymer composites subjected to impact loading using infrared thermography, ultrasonic C-scan and terahertz imaging', submitted to Composites Part A: Applied Science and Manufacturing.

[4] H. Zhang, S. Sfarra*, F. Sarasini, J. Fiorelli, J. Peeters, N. Avdelidis, D. Sartori, C. Ibarra-Castanedo, S. Perilli, Y. Mokhtari, J. Tirillo', X. Maldague, 'Impact modelling and a posteriori non-destructive evaluation of homogeneous particleboards of sugarcane bagasse – Part I', submitted to Journal of Nondestructive Evaluation. (with editor)

Published conference papers

[1] H. Zhang*, F. Robitaille*, U. Hassler, S. Joncas, X. Maldague, 'Experimental analyses for the flaws caused by fiber insertion and stitching in 3D preformed T-joint carbon fiber reinforced polymer composites using X-ray micro-computed tomography', in The 10th Canadian-International Conference on Composites, Ottawa, Canada, July 17-20, 2017.

[2] H. Zhang*, S. Sfarra, F. Sarasini, C. Ibarra-Castanedo, X. Maldague, 'Comparative Study of Impact Damage in Basalt-Carbon Hybrid Composites Using Infrared Thermography and Ultrasonic C-Scan', in The 2nd Asian Conference on Quantitative InfraRed Thermography, Daejeon, Korea, July 2-6, 2017. [DOI: 10.21611/qirt.2017.041]

[3] H. Zhang*, S. Sfarra, M. Genest, F. Sarasini, S. Perilli, H. Fernandes, J. Fleuret and X. Maldague, 'Numerical and experimental analyses for natural and non-natural impacted composites via thermographic inspection, ultrasonic C-scan and terahertz imaging', Proc. SPIE 10214 Thermosense: Thermal Infrared Applications XXXIX: 102140I, Anaheim, USA, April 9-13, 2017. [DOI: 10.1117/12.2262734]

[4] H. Zhang, S. Sfarra, C. Ibarra-Castanedo, F. Sarasini, J. Tirillò, N.P. Avdelidis*, J. Fiorelli, D. Sartori, S. Perilli and X. Maldague, 'Post-impact non-destructive evaluation of homogeneous particleboards of sugarcane bagasse', ASNT Annual Conference 2016, Long Beach, USA, October 24-27, 2016.

[5] H. Zhang*, H. Fernandes, M. Genest, U. Hassler, F. Robitaille, S. Joncas, X. Maldague, 'A comparative study of ultrasonic c-scan, micro-CT, infrared thermography and Terahertz NDT based on experiments and simulations of composites', in The 13th Quantitative InfraRed Thermography, Gdansk, Poland, July 4-8, 2016. [DOI: 10.21611/qirt.2016.155]

[6] H. Zhang*, H. Fernandes, L. Yu, U. Hassler, M. Genest, F. Robitaille, S. Joncas, Y. Sheng, X. Maldague, 'A comparative study of experimental and finite element analysis on submillimeter flaws by laser and ultrasonic excited thermography', in Proc. SPIE 9861 Thermosense: Thermal Infrared Applications XXXVIII: 98611A, Baltimore, USA, April 17-21, 2016. [DOI: 10.1117/12.2223209] *(Student Author Travel Grant)*

[7] H. Zhang*, U. Hassler, L. Yu, H. Fernandes, M. Genest, C. Ibarra-Castanedo, W. Holub, F. Robitaille, S. Joncas, X. Maldague, 'Micro-laser line thermography and high resolution x-ray tomography on micro-porosities: A comparative study of experiments and simulation', in The 13th International Workshop on Advanced Infrared Technology and Applications, Pisa, Italy, September 30-October 2, 2015. *(Under 35 Best Paper Award)*

[8] H. Zhang*, W. Holub, H. Fernandes, U. Hassler, S. Joncas, F. Robitaille, X. Maldague, 'Infrared thermography and x-ray tomography for non-destructive evaluation of micro-defects in CFRP', in The 1st QIRT-ASIA Conference on Quantitative InfraRed Thermography, Mahabalipuram, India, July 6-10, 2015. [DOI: 10.21611/qirt.2015.0093]

[9] H. Zhang*, M. Genest, F. Robitaille, X. Maldague, L. West, S. Joncas and C. Leduc, 'Infrared thermography, ultrasound c-scan and microscope for non-destructive and destructive evaluation of 3D carbon fiber materials: A comparative study', in Proc. SPIE 9485 Thermosense: Thermal Infrared Applications XXXVII: 94850X, Baltimore, USA, April 20-24, 2015. [DOI: 10.1117/12.2176853] (Best Student Paper Award)

Bibliography

[1] http://www.flir.com/.

[2] Clemente Ibarra-Castanedo, Daniel A González, François Galmiche, Abdelhakim Bendada, and Xavier P Maldague. On signal transforms applied to pulsed thermography. *Recent research developments in applied physics*, 9:101–27, 2006.

[3] Steven M Shepard, James R Lhota, Bruce A Rubadeux, David Wang, and Tasdiq Ahmed. Reconstruction and enhancement of active thermographic image sequences. *Optical Engineering*, 42(5):1337–1342, 2003.

[4] Clemente Ibarra-Castanedo and Xavier PV Maldague. Infrared thermography. In Horst Czichos, editor, *Handbook of technical diagnostics*, pages 175–220. Springer Berlin Heidelberg, 2013.

[5] Henrique C Fernandes and Xavier PV Maldague. Fiber orientation assessment on surface and beneath surface of carbon fiber reinforced composites using active infrared thermography. In *SPIE Sensing Technology+ Applications*, pages 91050D–91050D. International Society for Optics and Photonics, 2014.

[6] Henrique Fernandes and Xavier Maldague. Use of infrared thermography to measure fiber orientation on carbon-fiber reinforced composites. In *16th International Symposium on Applied Electromagnetics Mechanics (ISEM)*, page 275, 2013.

[7] Shen Yin, Xianwei Li, Huijun Gao, and Okyay Kaynak. Data-based techniques focused on modern industry: an overview. *IEEE Transactions on Industrial Electronics*, 62(1):657–667, 2015.

[8] Bin Gao, Wai Lok Woo, Gui Yun Tian, and Hong Zhang. Unsupervised diagnostic and monitoring of defects using waveguide imaging with adaptive sparse representation. *IEEE Transactions on Industrial Informatics*, 12(1):405–416, 2016.

[9] Bin Gao, Wai Lok Woo, Yunze He, and Gui Yun Tian. Unsupervised sparse pattern diagnostic of defects with inductive thermography imaging system. *IEEE Transactions on Industrial Informatics*, 12(1):371–383, 2016.

[10] Yihua Hu, Jiangfeng Zhang, Wenping Cao, Jiande Wu, Gui Yun Tian, Stephen J Finney, and James L Kirtley. Online two-section pv array fault diagnosis with optimized voltage sensor locations. *IEEE Transactions on Industrial Electronics*, 62(11):7237–7246, 2015.

[11] Abdenour Soualhi, Guy Clerc, and Hubert Razik. Detection and diagnosis of faults in induction motor using an improved artificial ant clustering technique. *IEEE Transactions on Industrial Electronics*, 60(9):4053–4062, 2013.

[12] Bin Gao, Yunze He, Wai Lok Woo, Gui Yun Tian, Jia Liu, and Yihua Hu. Multidimensional tensor-based inductive thermography with multiple physical fields for offshore wind turbine gear inspection. *IEEE Transactions on Industrial Electronics*, 63(10):6305–6315, 2016.

[13] Bin Liu, Yao He, Hai Zhang, Henrique Fernandes, Ying Fu, and Xavier Maldague. Study on characteristics of magnetic memory testing signal on the stress concentration field. *IET Science, Measurement & Technology*, 11(1):2–8, 2017.

[14] B Liu, Y Cao, H Zhang, YR Lin, WR Sun, and B Xu. Weak magnetic flux leakage: A possible method for studying pipeline defects located either inside or outside the structures. *NDT & E International*, 74:81–86, 2015.

[15] Bin Zhang, Chris Sconyers, Carl Byington, Romano Patrick, Marcos E Orchard, and George Vachtsevanos. A probabilistic fault detection approach: application to bearing fault detection. *IEEE Transactions on Industrial Electronics*, 58(5), 2011.

[16] Stjepan Stipetic, Marinko Kovacic, Zlatko Hanic, and Mario Vrazic. Measurement of excitation winding temperature on synchronous generator in rotation using infrared thermography. *IEEE Transactions on Industrial Electronics*, 59(5):2288–2298, 2012.

[17] Oscar Lucia, Pascal Maussion, Enrique J Dede, and Jose M Burdio. Induction heating technology and its applications: Past developments, current technology, and future challenges. *IEEE Transactions on Industrial Electronics*, 61(5):2509–2520, 2014.

[18] Óscar Lucía, Pascal Maussion, Enrique J Dede, and Jose M Burdio. Introduction to the special section on induction heating systems. *IEEE Transactions on Industrial Electronics*, 61(5):2504–2508, 2014.

[19] G Busse. Optoacoustic phase angle measurement for probing a metal. *Applied Physics Letters*, 35(10):759–760, 1979.

[20] BK Bein, J Gibkes, JH Gu, R Hüttner, J Pelzl, DL Balageas, and AA Déom. Thermal wave characterization of plasma-facing materials by ir radiometry. *Journal of nuclear materials*, 191:315–319, 1992.

[21] Datong Wu and Gerd Busse. Lock-in thermography for nondestructive evaluation of materials. *Revue générale de thermique*, 37(8):693–703, 1998.

[22] DA Derusova, VP Vavilov, and NV Druzhinin. Evaluating impact damage in graphite epoxy composite by using low-power vibrothermography. In *Proc. SPIE 9861, Thermosense: Thermal Infrared Applications XXXVIII*, page 98610F. International Society for Optics and Photonics, 2016.

[23] Charles Hellier. *Handbook of nondestructive evaluation*. McGraw-Hill, 2001.

[24] AB Pippard. Theory of ultrasonic attenuation in metals and magneto-acoustic oscillations. In *Proceedings of the Royal Society of London A: Mathematical, Physical and Engineering Sciences*, volume 257, pages 165–193. The Royal Society, 1960.

[25] H Jeong and DK Hsu. Experimental analysis of porosity-induced ultrasonic attenuation and velocity change in carbon composites. *Ultrasonics*, 33(3):195–203, 1995.

[26] CC Tsao and H Hocheng. Computerized tomography and c-scan for measuring delamination in the drilling of composite materials using various drills. *International Journal of Machine Tools and Manufacture*, 45(11):1282–1287, 2005.

[27] SR Stock. X-ray microtomography of materials. *International Materials Reviews*, 44(4):141–164, 1999.

[28] Paul J Schilling, BhanuPrakash R Karedla, Arun K Tatiparthi, Melody A Verges, and Paul D Herrington. X-ray computed microtomography of internal damage in fiber reinforced polymer matrix composites. *Composites Science and Technology*, 65(14):2071–2078, 2005.

[29] George Y Baaklini, Ramakrishna T Bhatt, Andrew J Eckel, Philip Engler, Richard W Rauser, and Michael G Castelli. X-ray microtomography of ceramic and metal matrix composites. *Materials evaluation*, 53(9), 1995.

[30] E Maire, L Babout, J-Y Buffiere, and R Fougeres. Recent results on 3d characterisation of microstructure and damage of metal matrix composites and a metallic foam using x-ray tomography. *Materials Science and Engineering: A*, 319:216–219, 2001.

[31] PM Mummery, B Derby, P Anderson, GR Davis, and JC Elliott. X-ray microtomographic studies of metal matrix composites using laboratory x-ray sources. *Journal of Microscopy*, 177(3):399–406, 1995.

[32] I Justice, P Anderson, G Davis, B Derby, and James Elliott. Damage nucleation and growth in particle reinforced aluminium matrix composites. *Key Engineering Materials*, 127:945–952, 1996.

[33] SA McDonald, M Preuss, E Maire, J-Y Buffiere, PM Mummery, and PJ Withers. X-ray tomographic imaging of ti/sic composites. *Journal of microscopy*, 209(2):102–112, 2003.

[34] Digby D Symons. Characterisation of indentation damage in 0/90 lay-up t300/914 cfrp. *Composites science and technology*, 60(3):391–401, 2000.

[35] Joy P Dunkers, Daniel P Sanders, Donald L Hunston, Matthew J Everett, and William H Green. Comparison of optical coherence tomography, x-ray computed tomography, and confocal microscopy results from an impact damaged epoxy/e-glass composite. *The Journal of Adhesion*, 78(2):129–154, 2002.

[36] Hongbin Shen, Steven Nutt, and David Hull. Direct observation and measurement of fiber architecture in short fiber-polymer composite foam through micro-ct imaging. *Composites Science and Technology*, 64(13):2113–2120, 2004.

[37] JSU Schell, M Renggli, GH Van Lenthe, R Müller, and P Ermanni. Micro-computed tomography determination of glass fibre reinforced polymer meso-structure. *Composites Science and Technology*, 66(13):2016–2022, 2006.

[38] Irl Duling and David Zimdars. Terahertz imaging: Revealing hidden defects. *Nature Photonics*, 3(11):630–632, 2009.

[39] TS Hartwick, DT Hodges, DH Barker, and FB Foote. Far infrared imagery. *Applied Optics*, 15(8):1919–1922, 1976.

[40] N Malykh, A Nagornyi, and E Yampolskii. Submillimeter-wave imagery. *Instrum. Exp. Tech*, 18(1):182–184, 1975.

[41] Thomas S Hartwick. Far infrared imaging techniques for law enforcement applications. In *Proc. SPIE 0108, Optics in Security and Law Enforcement I*, pages 139–140. International Society for Optics and Photonics, 1977.

[42] Karsten J Siebert, Torsten Löffler, Holger Quast, Mark Thomson, Tobias Bauer, Rainer Leonhardt, Stephanie Czasch, and Hartmut G Roskos. All-optoelectronic continuous wave thz imaging for biomedical applications. *Physics in medicine and biology*, 47(21):3743–3748, 2002.

[43] Nicholas Karpowicz, Hua Zhong, Jingzhou Xu, Kuang-I Lin, Jenn-Shyong Hwang, and XC Zhang. Comparison between pulsed terahertz time-domain imaging and continuous wave terahertz imaging. *Semiconductor Science and Technology*, 20(7):S293, 2005.

[44] Safa O Kasap. *Principles of electronic materials and devices*. McGraw-Hill, 2006.

[45] Ernst Schlömann. Dielectric losses in ionic crystals with disordered charge distributions. *Physical Review*, 135(2A):A413–A419, 1964.

[46] U Strom and PC Taylor. Temperature and frequency dependences of the far-infrared and microwave optical absorption in amorphous materials. *Physical Review B*, 16(12):5512–5522, 1977.

[47] M Naftaly and RE Miles. Terahertz time-domain spectroscopy of silicate glasses and the relationship to material properties. *Journal of Applied Physics*, 102(4):043517, 2007.

[48] M Koch, S Hunsche, P Schumacher, MC Nuss, J Feldmann, and J Fromm. Thz-imaging: a new method for density mapping of wood. *Wood Science and Technology*, 32(6):421–427, 1998.

[49] Yutaka Oyama, Li Zhen, Tadao Tanabe, and Munehito Kagaya. Sub-terahertz imaging of defects in building blocks. *NDT & E International*, 42(1):28–33, 2009.

[50] Xavier Maldague and Sergio Marinetti. Pulse phase infrared thermography. *Journal of applied physics*, 79(5):2694–2698, 1996.

[51] RL Thomas, JJ Pouch, YH Wong, LD Favro, PK Kuo, and Allan Rosencwaig. Subsurface flaw detection in metals by photoacoustic microscopya. *Journal of Applied Physics*, 51(2):1152–1156, 1980.

[52] Hernán Benítez, Xavier Maldague, Clemente Ibarra-Castanedo, Humberto Loaiza, Abdelhakim Bendada, and Eduardo Caicedo. Modified differential absolute contrast using thermal quadrupoles for the nondestructive testing of finite thickness specimens by infrared thermography. In *2006 Canadian Conference on Electrical and Computer Engineering*, pages 1039–1042. IEEE, 2006.

[53] Alexander Dillenz, Thomas Zweschper, and Gerhard Busse. Progress in ultrasound phase thermography. In *Aerospace/Defense Sensing, Simulation, and Controls*, pages 574–579. International Society for Optics and Photonics, 2001.

[54] G Busse. Nondestructive evaluation of polymer materials. *NDT & E International*, 27(5):253–262, 1994.

[55] Fernando Lopez, Clemente Ibarra-Castanedo, Vicente de Paulo Nicolau, and Xavier Maldague. Optimization of pulsed thermography inspection by partial least-squares regression. *NDT & E International*, 66:128–138, 2014.

[56] Sergio Marinetti, Ermanno Grinzato, Paolo G Bison, Edoardo Bozzi, Massimo Chimenti, Gabriele Pieri, and Ovidio Salvetti. Statistical analysis of ir thermographic sequences by pca. *Infrared Physics & Technology*, 46(1):85–91, 2004.

[57] Nikolas Rajic. Principal component thermography for flaw contrast enhancement and flaw depth characterisation in composite structures. *Composite Structures*, 58(4):521–528, 2002.

[58] Clemente Ibarra-Castanedo, Abdelhakim Bendada, and Xavier Maldague. Thermographic image processing for ndt. In *IV Conferencia Panamericana de END*, volume 79. Citeseer, 2007.

[59] Yuxia Duan. *Probability of detection analysis for infrared nondestructive testing and evaluation with applications including a comparison with ultrasonic testing.* PhD thesis, Université Laval, 2014.

[60] Hai Zhang, Ulf Hassler, Marc Genest, Henrique Fernandes, Francois Robitaille, Clemente Ibarra-Castanedo, Simon Joncas, and Xavier Maldague. Comparative study on submillimeter flaws in stitched t-joint carbon fiber reinforced polymer by infrared thermography, microcomputed tomography, ultrasonic c-scan and microscopic inspection. *Optical Engineering*, 54(10):104109, 2015.

[61] Stefano Sfarra, Stefano Perilli, Domenica Paoletti, and Dario Ambrosini. Ceramics and defects. *Journal of Thermal Analysis and Calorimetry*, 123(1):43–62, 2016.

[62] Stefano Sfarra, Edoardo Marcucci, Daniel Ambrosini, and D Paoletti. Infrared exploration of the architectural heritage: from passive infrared thermography to hybrid infrared thermography (hirt) approach. *Materiales de Construcción*, 66(323):e094, 2016.

[63] Henrique Fernandes, Hai Zhang, and Xavier Maldague. An active infrared thermography method for fiber orientation assessment of fiber-reinforced composite materials. *Infrared Physics & Technology*, 72:286–292, 2015.

[64] Henrique Fernandes, Clemente Ibarra-Castanedo, Hai Zhang, and Xavier Maldague. Thermographic non-destructive evaluation of carbon fiber-reinforced polymer plates after tensile testing. *Journal of Nondestructive Evaluation*, 34(4):1–10, 2015.

[65] Hai Zhang, Lingyao Yu, Ulf Hassler, Henrique Fernandes, Marc Genest, François Robitaille, Simon Joncas, Wolfgang Holub, Yunlong Sheng, and Xavier Maldague. An experimental and analytical study of micro-laser line thermography on micro-sized flaws in stitched carbon fiber reinforced polymer composites. *Composites Science and Technology*, 126:17–26, 2016.

[66] Henrique Fernandes, Hai Zhang, Alisson Figueiredo, Clemente Ibarra-Castanedo, Gilmar Guimarares, and Xavier Maldague. Carbon fiber composites inspection and defect characterization using active infrared thermography: numerical simulations and experimental results. *Applied Optics*, 55(34):D46–D53, 2016.

[67] Horatio Scott Carslaw and John Conrad Jaeger. *Conduction of heat in solids.* Oxford: Clarendon Press, 2nd ed., 1959.

[68] G Wróbel, S Pawlak, and G Muzia. Thermal diffusivity measurements of selected fiber reinforced polymer composites using heat pulse method. *Archives of Materials Science and Engineering*, 48(1):25–32, 2011.

[69] Abou-bakr Cherki, Abdelhamid Khabbazi, Benjamin Remy, and Dominique Baillis. Granular cork content dependence of thermal diffusivity, thermal conductivity and heat capacity of the composite material/granular cork bound with plaster. *Energy Procedia*, 42:83–92, 2013.

[70] WJ Parker, RJ Jenkins, CP Butler, and GL Abbott. Flash method of determining thermal diffusivity, heat capacity, and thermal conductivity. *Journal of applied physics*, 32(9):1679–1684, 1961.

[71] DL Balageas. Nouvelle méthode d'interprétation des thermogrammes pour la détermination de la diffusivité thermique par la méthode impulsionnelle (méthode flash). *Revue de Physique Appliquée*, 17(4):227–237, 1982.

[72] Christophe Ageorges, Lin Ye, Yiu-Wing Mai, and Meng Hou. Characteristics of resistance welding of lap shear coupons. part i: Heat transfer. *Composites Part A: Applied Science and Manufacturing*, 29(8):899–909, 1998.

[73] Stefano Sfarra, F Lopez, F Sarasini, J Tirillò, L Ferrante, S Perilli, C Ibarra-Castanedo, D Paoletti, L Lampani, P Gaudenzi, E Barbero, S Sánchez-Sáez, and X Maldague. Analysis of damage in hybrid composites subjected to ballistic impacts: an integrated non-destructive approach. In Vijay Kumar Thakur, Manju Kumari Thakur, and Michael R Kessler, editors, *Handbook of Composites from Renewable Materials*, volume 3, pages 175–210. WILEY-Scrivener Publisher, 2017.

[74] Hai Zhang, Henrique Fernandes, Frank Billy Djupkep Dizeu, Ulf Hassler, Julien Fleuret, Marc Genest, Clemente Ibarra-Castanedo, François Robitaille, Simon Joncas, and Xavier Maldague. Pulsed micro-laser line thermography on submillimeter porosity in carbon fiber reinforced polymer composites: experimental and numerical analyses for the capability of detection. *Applied Optics*, 55(34):D1–D10, 2016.

[75] Bardia Yousefi, Seyed Mostafa Mirhassani, Alireza AhmadiFard, and MohammadMehdi Hosseini. Hierarchical segmentation of urban satellite imagery. *International Journal of Applied Earth Observation and Geoinformation*, 30:158–166, 2014.

[76] Bardia Yousefi, Julien Fleuret, Hai Zhang, Xavier PV Maldague, Raymond Watt, and Matthieu Klein. Automated assessment and tracking of human body thermal variations using unsupervised clustering. *Applied Optics*, 55(34):D162–D172, 2016.

[77] S Sfarra, C Ibarra-Castanedo, F Sarasini, C Santulli, and XPV Maldague. Basalt fibre laminates non-destructively inspected after low-velocity impacts. *FME Transactions*, 44(4):381, 2016.

[78] Stefano Sfarra, Clemente Ibarra-Castanedo, Carlo Santulli, Domenica Paoletti, and Xavier Maldague. Monitoring of jute/hemp fiber hybrid laminates by nondestructive testing techniques. *Science and Engineering of Composite Materials*, 23(3):283–300, 2016.

[79] Juliano Fiorelli, Diego Donizetti Curtolo, Núbia G Barrero, Holmer Savastano, Eliria Maria de Jesus Agnolon Pallone, and Ryan Johnson. Particulate composite based on coconut fiber and castor oil polyurethane adhesive: An eco-efficient product. *Industrial Crops and Products*, 40:69–75, 2012.

[80] H Zhang, S Sfarra, C Ibarra-Castanedo, F Sarasini, J Tirillo, N Avdelidis, J Fiorelli, D Sartori, S Perilli, and XPV Maldague. Post-impact non-destructive evaluation of homogeneous sugarcane bagasse particleboards. In *ASNT Annual Conference 2016*, pages 2–10, 2016.

[81] Sreekumar Kaiplavil and Andreas Mandelis. Truncated-correlation photothermal coherence tomography for deep subsurface analysis. *Nature Photonics*, 8(8):635–642, 2014.

[82] Sreekumar Kaiplavil, Andreas Mandelis, and Bennett T Amaechi. Truncated-correlation photothermal coherence tomography of artificially demineralized animal bones: two-and three-dimensional markers for mineral loss monitoring. *Journal of biomedical optics*, 19(2):026015, 2014.

[83] Hai Zhang, Henrique Fernandes, Ulf Hassler, Clemente Ibarra-Castanedo, Marc Genest, François Robitaille, Simon Joncas, and Xavier Maldague. Comparative study of micro-laser excitation thermography and microultrasonic excitation thermography on submillimeter porosity in carbon fiber reinforced polymer composites. *Optical Engineering*, 56(4):041304, 2017.

[84] Mehmet Aktaş, Cesim Atas, Bülent Murat İçten, and Ramazan Karakuzu. An experimental investigation of the impact response of composite laminates. *Composite Structures*, 87(4):307–313, 2009.

[85] PNB Reis, JAM Ferreira, P Santos, MOW Richardson, and JB Santos. Impact response of kevlar composites with filled epoxy matrix. *Composite Structures*, 94(12):3520–3528, 2012.

[86] Jeremy Gustin, Aaran Joneson, Mohammad Mahinfalah, and James Stone. Low velocity impact of combination kevlar/carbon fiber sandwich composites. *Composite structures*, 69(4):396–406, 2005.

[87] NK Naik, R Ramasimha, HEMENDRA Arya, SV Prabhu, and N ShamaRao. Impact response and damage tolerance characteristics of glass–carbon/epoxy hybrid composite plates. *Composites Part B: Engineering*, 32(7):565–574, 2001.

[88] Tamás Deák and Tibor Czigány. Chemical composition and mechanical properties of basalt and glass fibers: a comparison. *Textile Research Journal*, 79(7):645–651, 2009.

[89] V Fiore, T Scalici, G Di Bella, and A Valenza. A review on basalt fibre and its composites. *Composites Part B: Engineering*, 74:74–94, 2015.

[90] Anne Ross. Basalt fibers: Alternative to glass? *Composites Technology*, 12(4):44–48, 2006.

[91] S Sfarra, C Ibarra-Castanedo, F Sarasini, C Santulli, and XPV Maldague. Basalt fibre laminates non-destructively inspected after low-velocity impacts. *FME Transactions*, 44(4):380–385, 2016.

[92] Stefano Sfarra, Clemente Ibarra-Castanedo, Carlo Santulli, Alfonso Paoletti, Domenica Paoletti, Fabrizio Sarasini, Abdelhakim Bendada, and Xavier Maldague. Falling weight impacted glass and basalt fibre woven composites inspected using non-destructive techniques. *Composites Part B: Engineering*, 45(1):601–608, 2013.

[93] F Sarasini, J Tirillò, L Ferrante, M Valente, T Valente, L Lampani, P Gaudenzi, S Cioffi, S Iannace, and L Sorrentino. Drop-weight impact behaviour of woven hybrid basalt–carbon/epoxy composites. *Composites Part B: Engineering*, 59:204–220, 2014.

[94] Pierre Servais, Nathalie Gerlach, Jason Habermehl, Clemente Ibarra-Castanedo, and Xavier Maldague. Characterization of manufacturing and maintenance of aerospace composite discontinuities using infrared thermography. *Materials Evaluation*, 66(9):955–962, 2008.

[95] Fredrik Stig. *3D-woven Reinforcement in Composites*. PhD thesis, KTH Royal Institute of Technology, 2012.

[96] Fredrik Stig and Stefan Hallström. Assessment of the mechanical properties of a new 3d woven fibre composite material. *Composites Science and Technology*, 69(11):1686–1692, 2009.

[97] Johan Ekh. *Multi-fastener single-lap joints in composite structures*. PhD thesis, KTH Royal Institute of Technology, 2006.

[98] PB Stickler and M Ramulu. Investigation of mechanical behavior of transverse stitched t-joints with pr520 resin in flexure and tension. *Composite structures*, 52(3):307–314, 2001.

[99] P Potluri, E Kusak, and TY Reddy. Novel stitch-bonded sandwich composite structures. *Composite Structures*, 59(2):251–259, 2003.

[100] Tae Jin Kang and Sung Ho Lee. Effect of stitching on the mechanical and impact properties of woven laminate composite. *Journal of Composite Materials*, 28(16):1574–1587, 1994.

[101] Yoseph Bar-Cohen. Emerging ndt technologies and challenges at the beginning of the third millennium, part 2. *Materials evaluation*, 58(2):141–150, 2000.

[102] Makoto Ito and Tsu-Wei Chou. An analytical and experimental study of strength and failure behavior of plain weave composites. *Journal of Composite Materials*, 32(1):2–30, 1998.

[103] EJ Barbero, P Lonetti, and KK Sikkil. Finite element continuum damage modeling of plain weave reinforced composites. *Composites Part B: Engineering*, 37(2):137–147, 2006.

[104] J Schlichting, GN Kervalishvili, Ch Maierhofer, and M Kreutzbruck. Imaging cracks by laser excited thermography. In *REVIEW OF PROGRESS IN QUANTITATIVE NONDESTRUCTIVE EVALUATION VOLUME 29*, volume 1211, pages 727–734. AIP Publishing, 2010.

[105] T Li, Darryl P Almond, and D Andrew S Rees. Crack imaging by scanning laser-line thermography and laser-spot thermography. *Measurement Science and Technology*, 22(3):035701, 2011.

[106] Hai Zhang, Marc Genest, Francois Robitaille, Xavier Maldague, Lucas West, Simon Joncas, and Catherine Leduc. Infrared thermography, ultrasound c-scan and microscope for non-destructive and destructive evaluation of 3d carbon fiber materials: a comparative study. In *Proc. SPIE 9485, Thermosense: Thermal Infrared Applications XXXVII*, page 94850X. International Society for Optics and Photonics, 2015.

[107] Ali Rostami, Hassan Rasooli, and Hamed Baghban. *Terahertz technology: fundamentals and applications*. Springer Science & Business Media, 2011.

[108] Corinna L Koch Dandolo, Troels Filtenborg, Jacob Skou-Hansen, and Peter Uhd Jepsen. Analysis of a seventeenth-century panel painting by reflection terahertz time-domain imaging (thz-tdi): contribution of ultrafast optics to museum collections inspection. *Applied Physics A*, 121(3):981–986, 2015.

[109] Corinna L Koch Dandolo, Antonino Cosentino, and Peter Uhd Jepsen. Inspection of panel paintings beneath gilded finishes using terahertz time-domain imaging. *Studies in Conservation*, 60(S1):S159–S166, 2015.

[110] Emmanuel Abraham, Ayesha Younus, Jean-Christophe Delagnes, and Patrick Mounaix. Non-invasive investigation of art paintings by terahertz imaging. *Applied Physics A*, 100(3):585–590, 2010.

[111] J Labaune, JB Jackson, S Pages-Camagna, IN Duling, M Menu, and GA Mourou. Papyrus imaging with terahertz time domain spectroscopy. *Applied Physics A*, 100(3):607–612, 2010.

[112] Emmanuel Abraham and Kaori Fukunaga. Terahertz imaging applied to the examination of artistic objects. *Studies in Conservation*, 60(6):343–352, 2015.

[113] Kaori Fukunaga, Tomofumi Ikari, and Kikuko Iwai. Thz pulsed time-domain imaging of an oil canvas painting: a case study of a painting by pablo picasso. *Applied Physics A*, 122(2):1–5, 2016.

[114] Marcello Picollo, Kaori Fukunaga, and Julien Labaune. Obtaining noninvasive stratigraphic details of panel paintings using terahertz time domain spectroscopy imaging system. *Journal of Cultural Heritage*, 16(1):73–80, 2015.

[115] Tanja Trafela, Maya Mizuno, Kaori Fukunaga, and Matija Strlič. Quantitative characterisation of historic paper using thz spectroscopy and multivariate data analysis. *Applied Physics A*, 111(1):83–90, 2013.

[116] A Bendada, S Sfarra, M Akhloufi, J Caumes, C Pradere, J Batsale, X Maldague, et al. Subsurface imaging for panel paintings inspection: A comparative study of the ultraviolet, the visible, the infrared and the terahertz spectra. *Opto-Electronics Review*, 23(1):90–101, 2015.

[117] RM Groves, B Pradarutti, E Kouloumpi, W Osten, and G Notni. 2d and 3d nondestructive evaluation of a wooden panel painting using shearography and terahertz imaging. *Ndt & E International*, 42(6):543–549, 2009.

[118] GP Gallerano, A Doria, E Giovenale, G Messina, A Petralia, I Spassovsky, K Fukunaga, and I Hosako. Thz-arte: non-invasive terahertz diagnostics for art conservation. In *Proceedings of the 33rd International Conference on Infrared, Millimeter and Terahertz Waves*. IEEE, 2008.

[119] A Bendada, S Sfarra, M Genest, D Paoletti, S Rott, E Talmy, C Ibarra-Castanedo, and X Maldague. How to reveal subsurface defects in kevlar® composite materials after an impact loading using infrared vision and optical ndt techniques? *Engineering Fracture Mechanics*, 108:195–208, 2013.

[120] Duy Thong Nguyen. *Design, modeling, and characterization of innovative terahertz detectors*. PhD thesis, Université de Grenoble, 2012.

[121] Roger Adrian Lewis. *Terahertz physics*. Cambridge University Press, 2012.

[122] JC Lizarraga and Carlos Del-Rio. Resolution capabilities of future thz cameras. In *Proceedings of the 4th European Conference on Antennas and Propagation*. IEEE, 2010.

[123] Piotr Garbacz. Terahertz imaging–principles, techniques, benefits, and limitations. *Problemy Eksploatacji*, (1):81–92, 2016.

[124] D Gavrilov, R Gr Maev, and DP Almond. A review of imaging methods in analysis of works of art: Thermographic imaging method in art analysis. *Canadian Journal of Physics*, 92(4):341–364, 2014.

[125] Paul Craddock. *Scientific investigation of copies, fakes and forgeries*. Routledge, 2009.

[126] Hermann Kühn. Trace elements in white lead and their determination by emission spectrum and neutron activation analysis. *Studies in Conservation*, 11(4):163–169, 1966.

[127] Woon Siong Gan. *Acoustical Imaging: Techniques and Applications for Engineers*. John Wiley & Sons, 2012.

[128] DJ Daniels. Ground penetrating radar . knoval (institution of engineering and technology). 2004.

[129] Roman G Maev, RE Green Jr, and AM Siddiolo. Review of advanced acoustical imaging techniques for nondestructive evaluation of art objects. *Research in Nondestructive Evaluation*, 17(4):191–204, 2006.

[130] Alison Murray, Marion F Mecklenburg, CM Fortunko, and Robert E Green. Air-coupled ultrasonic system: a new technology for detecting flaws in paintings on wooden panels. *Journal of the American Institute for Conservation*, 35(2):145–162, 1996.

[131] AM Siddiolo, A Maeva, and R Gr Maev. Air-coupled imaging method applied to the study and conservation of paintings. In *Acoustical Imaging*, volume 28, pages 3–12. Springer, 2007.

[132] Massimiliano Pieraccini, Daniele Mecatti, Matteo Fratini, Carlo Atzeni, and Maurizio Seracini. A high frequency gpr application to the cultural heritage survey: the search of the" battle of anghiari" by leonardo da vinci. In *Proceedings of the 10th International Conference on Grounds Penetrating Radar*, volume 1, pages 391–394. IEEE, 2004.

[133] Stefano Sfarra, Abdelhakim Bendada, Clemente Ibarra-Castanedo, Dario Ambrosini, Domenica Paoletti, and Xavier Maldague. Santa maria di collemaggio church (l'aquila, italy): Historical reconstruction by non-destructive testing techniques. *International Journal of Architectural Heritage*, 9(4):367–390, 2015.

[134] Xavier Maldague. *Theory and practice of infrared technology for nondestructive testing*. Wiley, 2001.

[135] Stefano Sfarra, Clemente Ibarra-Castanedo, Domenica Paoletti, and Xavier Maldague. Infrared vision inspection of cultural heritage objects from the city of l'aquila, italy and its surroundings. *Materials Evaluation*, 71(5):561–570, 2013.

[136] Clemente Ibarra-Castanedo, Stefano Sfarra, Dario Ambrosini, Domenica Paoletti, Abdelhakim Bendada, and Xavier Maldague. Diagnostics of panel paintings using holographic interferometry and pulsed thermography. *Quantitative InfraRed Thermography Journal*, 7(1):85–114, 2010.

[137] Stefano Sfarra, Clemente Ibarra-Castanedo, Mariagrazia Tortora, Lorenzo Arrizza, Giorgio Cerichelli, Iole Nardi, and Xavier Maldague. Diagnostics of wall paintings: A smart and reliable approach. *Journal of Cultural Heritage*, 18:229–241, 2016.

[138] S Sfarra, P Theodorakeas, J Černeckỳ, E Pivarčiová, S Perilli, and M Koui. Inspecting marquetries at different wavelengths: The preliminary numerical approach as aid for a wide-range of non-destructive tests. *Journal of Nondestructive Evaluation*, 36(1):6, 2017.

[139] S Sfarra, C Ibarra-Castanedo, D Ambrosini, D Paoletti, A Bendada, and X Maldague. Discovering the defects in paintings using non-destructive testing (ndt) techniques and passing through measurements of deformation. *Journal of Nondestructive Evaluation*, 33(3):358–383, 2014.

[140] Clemente Ibarra-Castanedo, Stefano Sfarra, Dario Ambrosini, Domenica Paoletti, Abdelhakim Bendada, and Xavier Maldague. Subsurface defect characterization in artworks by quantitative pulsed phase thermography and holographic interferometry. *Quantitative InfraRed Thermography Journal*, 5(2):131–149, 2008.

[141] Mariagrazia Tortora, Stefano Sfarra, Marco Chiarini, Valeria Daniele, Giuliana Taglieri, and Giorgio Cerichelli. Non-destructive and micro-invasive testing techniques for characterizing materials, structures and restoration problems in mural paintings. *Applied Surface Science*, 387:971–985, 2016.

[142] Ronald Anderson and Anne Koval. *James McNeill Whistler: Beyond the Myth*. John Murray London, 1994.

[143] Richard Dorment and Margaret MacDonald. James mcneill whistler. *The Art Book*, 2(1):15–16, 1995.

[144] Gordon H Fleming. *James Abbott McNeill Whistler: A Life*. Windrush Press, 1991.

[145] Burns Archer Stubbs. *James McNeill Whistler: A Biographical Outline*, volume 1. Freer Gallery of Art, 1950.

[146] Xiaochuan Bi, Tracey Krakowski, and Doug Weiser. Integration of the silicon impatt diode in an analog technology, July 9 2014. US Patent App. 14/327,157.

[147] Igor Kukushkin, Viacheslav Muravev, Gombo Tsydynzhapov, and Anton Fortunatov. High-speed giga-terahertz imaging device and method, December 23 2011. US Patent App. 13/336,912.

[148] Richard H Wittstruck. Method for high frequency device operation with high temperature and radiation hard characteristics, July 29 1997. US Patent 5,652,551.

[149] Stefano Sfarra, Clemente Ibarra-Castanedo, Stefano Ridolfi, Giorgio Cerichelli, Dario Ambrosini, Domenica Paoletti, and Xavier Maldague. Holographic interferometry (hi), infrared vision and x-ray fluorescence (xrf) spectroscopy for the assessment of painted wooden statues: a new integrated approach. *Applied Physics A*, 115(3):1041–1056, 2014.

[150] Clemente Ibarra-Castanedo. *Quantitative subsurface defect evaluation by pulsed phase thermography: depth retrieval with the phase*. PhD thesis, Université Laval, 2005.

[151] Xiao Xiao, Ho Ming Leung, Che Ting Chan, and Weijia Wen. Manipulation of the polarization of terahertz wave in subwavelength regime. *Scientific reports*, 5, 2015.

[152] Nima Tabatabaei, Andreas Mandelis, and Bennett T Amaechi. Thermophotonic radar imaging: An emissivity-normalized modality with advantages over phase lock-in thermography. *Applied Physics Letters*, 98(16):163706, 2011.